UNIVERSITÀ DEGLI STUDI DI PARMA

Dottorato di Ricerca in Ingegneria Civile e Architettura

Ciclo XXXVIII

Experimental analysis of air exchange mechanisms between indoor environments under human and climatic forcings

Coordinatore:
Prof. Andrea Spagnoli

Tutor:
Prof. Luca Chiapponi

Co-tutor:
Prof. Sandro Longo

Dottorando:
Nicolò Merli

Anni Accademici 2022/2023 – 2024/2025

UNIVERSITÀ DI PARMA

UNIVERSITÀ DEGLI STUDI DI PARMA

Doctorate in Civil Engineering and Architecture

XXXVIII cycle

Experimental analysis of air exchange mechanisms between indoor environments under human and climatic forcings

Coordinator:
Prof. Andrea Spagnoli

Supervisor:
Prof. Luca Chiapponi

Co-supervisor:
Prof. Sandro Longo

Ph.D. student:
Nicolò Merli

Academic years 2022/2023 – 2024/2025

Ringraziamenti

Quello che i (pochi) lettori di questa tesi troveranno nelle pagine che seguono è una relazione scientifica del lavoro da me svolto durante un triennio di avviamento all'attività di ricerca, il dottorato. Cominciavo nel novembre 2022 *quand'era in parte altr'uom da quel ch'i' sono*, dopo un anno abbondante trascorso a stretto contatto con le, a mio avviso, deprimenti e provinciali realtà lavorative parmigiano-reggiane legate al mondo dell'ingegneria civile e ambientale.

All'Università ho trovato una grande libertà, la soddisfazione di essere tenuto in considerazione e di essere trattato con dignità e rispetto, la bella fatica di lavorare con gli studenti di quello che era stato il mio corso di laurea, la possibilità di viaggiare per presentare il mio lavoro ... Mi sono unito a un gruppo di ricerca che approccia l'idraulica (e tutte le sue derivazioni) con grande rigore, precisione ferrea e immensa curiosità. Spero che la possibilità di fare un dottorato di ricerca rimanga aperta per il maggior numero di studenti possibile, specialmente nella nostra ignorante società in cui l'importanza dello studio e del lavoro intellettuale è sempre più messa in discussione.

Desidero ringraziare prima di tutti il Prof. Luca Chiapponi che è una guida insostituibile, la cui presenza costante e la cui creatività scientifica sono ciò che ha reso possibile questo lavoro. Ringrazio inoltre il Prof. Sandro Longo che è per me un modello inarrivabile di dedizione alla materia, uno dei sempre più scarsi pilastri su cui l'Università Italiana si fonda. Non manca un ringraziamento anche per Fabio Addona, che ha già percorso il sentiero del dottorato e che da due anni condivide con me l'ufficio: è stata una importante fonte di consigli e aiuti.

I limiti del linguaggio come tutti sappiamo sono enormi e dopo secoli di esperienze volte a forzarli mi ritrovo anch'io nella triste condizione di spiegare a parole tutto quello che ho vissuto insieme a questo lavoro. Ci rinuncio, è impossibile.

Abstract

Airflow dynamics in indoor environments play a crucial role in pollutant dispersion and the overall indoor microclimate. This study experimentally investigates air exchange processes between two interconnected rooms under two distinct driving mechanisms: human motion, specifically the "pump effect" generated by a person walking through a doorway, and wind-induced interactions between indoor and outdoor spaces.

To capture these phenomena, two reduced-scale experimental models were developed based on Reynolds number similarity. The first, operating with air inside a wind tunnel, explored the effects of external wind, window configurations, and pressure differentials on inter-room airflows. Hot-wire anemometry measurements provided a detailed characterization of turbulence and flow rates, revealing a power-law relationship between the volumetric flow rate and the Euler number, with an observed exponent of 0.39.

The second model, a water-filled tank, enabled detailed visualization of turbulent flow structures generated by human motion through the use of ultrasonic velocimetry and in particular Particle Image Velocimetry (PIV). The results highlighted how walking speed and imposed recirculation flows influence air exchange, with specific flow rates identified that minimize cross-contamination between rooms.

The findings offer valuable insights for the design of localized ventilation strategies aimed at reducing backflow and improving indoor air quality. Future work will extend the experimental database to support the calibration and validation of computational fluid dynamics (CFD) models, enabling accurate prediction of recirculation and stagnation zones and optimizing HVAC system design.

Contents

List of Figures

List of Tables

Chapter 1

Introduction

1.1 Archaeology of the topic

In the history of Western thought, the concepts of air quality and pollution caused by human activities have been present since ancient times. It was the Greek physician Hippocrates, considered the father of scientific medicine, who formulated the miasmatic theory, identifying miasmas, poisonous emanations from decomposing organic matter, as the cause of diseases such as cholera, plague, and malaria. Hippocrates advocated for air purification as a fundamental action to ensure healing and maintain health. The issue of air quality already emerged in ancient times as multifaceted and multidisciplinary. For example, we can recall the architectural contributions concerning the construction of buildings by Vitruvius (approx. 80 BC - 15 BC) first with *De Architectura*, and later by the Florentine Leon Battista Alberti (1404-1472) with *De Re Aedificatoria*. Alberti, with his promotion of a rational and scientific approach to learning, laid the foundations of modern territorial planning, starting, among other things, from the assumption that foul air represents a natural hazard that should be avoided.

A first systematization of the state of the art in air quality studies was published in 1751 by John Arbuthnot (Arbuthnot, 1751). In this review, the author outlines a series of general and broadly applicable guidelines regarding the ventilation of homes to ensure proper air exchange prescribing, for example, a daily air exchange for indoor environments.

The link between the aforementioned contributions, which, despite their coherence and rationality, now seem archaic to us, and a more contemporary study of the subject, is provided by the pioneering work of Max Joseph von Pettenkofer on the topic. Of particular importance is his understanding of the concentration of carbon dioxide in indoor environments as an indicator of air quality. In Pettenkofer (1858), he states that one volume of carbon dioxide in 1000 volumes of room air marks the threshold that separates good air from bad air and that, on average, in spaces where the air is maintained at a good quality, there was a ventilation rate of more than 2100 cubic feet per person per hour (16.5 l/s per person, not far from today standard values, formalized for example in the UNI EN 16798-1 Italian standard).

1.2 Review of contemporary contributions

As will be seen in the following discussion, our goal is to study, describe, and quantify air mixing phenomena in two interconnected indoor environments with a view to laying the groundwork for studying their implications on indoor air quality and, ultimately, on human health. Air flows and their mixing dynamics in indoor environments have a huge impact on the dispersion of pollutants and, in turn, on the microclimate that develops inside buildings. The particles dispersed in the air move along with it; therefore, knowing the motion field that occurs in an environment, particularly indoors, under specific conditions, translates into mapping recirculation zones and stagnation points, identifying areas with high or low concentrations of dispersed micromaterials.

The study of air quality in both indoor and outdoor environments has been a prolific field of research in the recent years, especially after the Covid-19 pandemic. In fact, air is the main vehicle of viruses, pollutants and other threats for human health. In the 1970s, indoor air quality was thought to be influenced solely by outdoor atmospheric pollution. However, the energy crisis spurred a shift in building design toward creating more airtight spaces. This approach, aimed at minimizing thermal energy loss through better insulation and sealed windows, achieved energy and cost savings but reduced air exchange with the outdoor environment. Consequently, indoor levels of chemical compounds rose significantly, posing health risks to the cardiovascular, immune, and respiratory systems. This issue led to a reassessment of indoor air quality and underscored the need for dedicated research into indoor environments. It became evident that indoor air quality is shaped by multiple factors, including ventilation efficiency, materials used in construction and decoration, and occupant activities. Growing awareness of the health risks associated with poor indoor air quality, coupled with the fact that people spend 70–90% of their time indoors, heightened interest in studying indoor pollutants. Factors such as age, geographical location, type of work, and lifestyle habits further influence exposure levels to indoor environments (Śmiełowska et al., 2017).

In particular, the most critical period of the year from an outdoor air pollution point of view is winter, since we have to consider the combination of higher concentrations of particulate matter, the need to heat indoor environments and the reduced habit of ventilating closed rooms due to lower outside temperatures. In order to deal with the combination of these instances, it's important to evaluate the effects of air purification or air ventilation systems. Underfloor heating and radiators are devices used to achieve thermal comfort in winter and play a key role in indoor air quality. Underfloor heating systems have gained popularity because of the advantages of providing a high thermal comfort saving energy at the same time. They uses either fluid flowing through pipes or electrical resistance elements to heat the floor and control the indoor climate by generating indoor air currents through conduction, radiation, and convection. These air movements favour the spread of airborne pollutants. However, in most buildings with underfloor heating, there is a lack of fresh air systems in winter, resulting in poor indoor air quality. In addition, pathogens or pollutants are often brought into the indoor environment through entrance doors by air currents from outside or neighbouring indoor areas. Ventilation and air cleaning systems play an important role in removing pollutants and indoor particles (Ciuzas et al., 2016; Feng et al., 2016), with the result of an improved air quality (Cao and Meyers, 2013; Cao and Yang, 2016). When air quality is involved, the comprehension and the analysis of gravity-driven phenomena is necessary: in fact, movements of air fluxes, and consequently the spatial variation of particles concentration, act as gravity currents. These currents are generated by the interaction between fluids having different densities and the scientific results of air quality studies, both for observations and predictions, are based on dynamics governed by gravity (Linden and Simpson, 1985). In order to simulate what happens in various spatial domains in terms of dispersion of air fluxes and particles of various nature, researchers use physical and numerical models. The first model type refers to the laboratory reconstruction of various real environments based on similarity criteria and to the execution of experiments usually aimed at validating analytical models that describe the observed phenomena or at describing natural behaviours through the introduction of dimensionless parameters. On the other hand, the second model type is based on numerical simulations of real problems using the computational fluid dynamics (CFD).

1.2.1 Indoor air quality and indoor/outdoor air exchange

The rapid growth of urban areas and industrial activities in recent years has led to an increase in air pollutants around the world. The deterioration of air quality can have a huge impact on the health, well-being, and quality of life of urban dwellers (Chan and Yao, 2008; Hachem and Bensefa-Colas, 2019). When studying air quality conditions, an important aspect to consider is the ventilation of enclosed (indoor) environments (Cui et al., 2021), as increasing urbanisation has increased the amount of time spent indoors. Typically, indoor/outdoor (or indoor/indoor) airflow is driven by two forces (Linden, 1999; Walker et al., 2011):

1. Buoyant flows induced by temperature and/or density gradients. They can develop through vents, openings and, in general, whenever the ambient fluid from two different environments mixes (Mingotti et al., 2011).

2. Pressure gradients (e.g., due to wind action).

The exchange of air and heat between indoor and outdoor environments has been studied extensively. This attention stems from the importance of ventilation systems in improving the efficiency of air conditioning (Hunt and Linden, 1999), managing the transport of pollutants (Mingotti et al., 2013, 2020a) and controlling the spread of harmful substances such as viruses (Cui et al., 2021). Even if many studies have investigated the impact of airflow management and building ventilation on the transmission of airborne diseases, most of these studies have made simplifying assumptions by assuming steady-state conditions (Godish and Spengler, 1996; Liddament, 2000; Fan and Li, 2022; Mata et al., 2022). As a result, they have overlooked the dynamic events that occur within indoor spaces (for example the movement of persons and equipment and the opening and closing of doors and windows). These events can have a great influence on airflow patterns and aerosol distribution, particularly in low-ventilated spaces such as office and residential buildings (Lv et al., 2021; Wu et al., 2022). Many studies have analysed the transport and distribution of airborne particles, focusing on different ventilation modes and heat sources. These studies have highlighted the significant influence of different ventilation modes on particle diffusion. For example, Zhang and Chen (2006) studied the distribution of particles depending on three different ventilation systems, and their results showed that the underfloor air distribution (UFAD) system performed better than ceiling and sidewall systems. However, it is possible the particles which have settled on the floor could become airborne again for various reasons, including people walking around the room. Jurelionis and Martuzevicius (2015) used experimental methods to investigate the effect of ventilation strategy on aerosol dispersion and removal. They found that one-way mixing ventilation was effective in directing particles towards the exhaust diffuser, especially at low air exchange rates. Zhuang et al. (2017) investigated particle removal and deposition in two different air conditioning systems in a room. They found that (1) the central air conditioning system made particle removal more efficient, and (2) increasing the air supply velocity accelerated particle removal without reducing the final contamination level. Habchi and Alotaibi (2016) demonstrated that the combination of ceiling personalised ventilation and a desk fan could achieve superior performance in terms of particle reduction, compared to using a conventional mixing ventilation system. Overall, these studies provide valuable insights into the effects of different ventilation approaches on particle transport and distribution in indoor environments. They shed light on the potential advantages and disadvantages of different ventilation strategies in terms of particle removal and concentration in specific zones. These findings are crucial for the development of effective ventilation systems to maintain better indoor air quality and minimise the risk of cross-contamination and exposure to pollutants or pathogens.

In addition to forced or natural ventilation, the effects of airing have also been investigated, although to a lesser extent. Airing is the temporary opening of windows or doors. This enhances natural ventilation and can mitigate indoor contaminant peaks while saving energy compared to constant high-flow mechanical ventilation. It is particularly valuable in environments like museums and churches, where it prevents the soiling of artifacts by diluting indoor particulates. While mechanical ventilation is common in modern buildings, historical structures and older houses rely heavily on natural ventilation and airing. As airtight construction becomes more prevalent, temporary airing methods are increasingly crucial for maintaining indoor air quality. Wind tunnel studies offer controlled environments for understanding these mechanisms and refining predictive models for ventilation system design and energy assessments. Buoyancy-driven flow is more widely studied compared to wind-driven flow (Hayati et al., 2019). However, wind-driven flow, which will constitute a significant focus of this thesis, is notably affected by both the average wind speed and turbulent fluctuations. Studies on pulsation flows and mixing layer theory have demonstrated the critical role of fluctuations and eddy penetration in shaping wind-driven ventilation (Malinowski, 1971). Research further emphasizes how eddies and turbulence within openings facilitate air exchange, especially when the wind direction is parallel to the opening. Airing mechanisms include cross-ventilation and single-sided ventilation. For single-sided ventilation, Warren (1977) examines the mechanisms of natural ventilation in spaces with openings located exclusively on a single external wall focusing on environments like sealed offices or classrooms, where through-ventilation is unavailable. The work achieves some results on the performance of different types of windows, highlighting the fact that the results will need to be improved to also consider situations where turbulence plays a role. Experimental studies conducted in the field of single-sided ventilation have made it possible to determine the ventilation flow rate using predictive models based on pressure measurements, and examining its dependence on aperture separation (Daish et al. (2016)) or the ventilation dynamics even in the case of corner rooms, including numerical LES-type simulations (da Graca et al. (2021)) or the effects of window geometry on single sided ventilation (Albuquerque et al. (2021)). Sandberg et al. (2015) studies the interaction between wind driven flow and a church, reproduced into a wind tunnel with a reduced scale model which was adopted by Hayati et al. (2019). It shows that the region influenced by wind blockage extended roughly twice the building's roof height and the fact that understanding stagnation points and their relationship to openings is crucial for predicting wind flow. Cross ventilation is investigated, among others, in Da Graça and Linden (2003) where it is developed a simplified model that provides formulas to predict airflow rates and velocities in cross-ventilated rooms, showing how room geometry influences ventilation and in Micallef et al. (2016), who numerically models the realistic case of a courtyard building. Previous research has also focused on investigating the effect of door movements on aerosol dispersion in isolation rooms with negative pressure, which are designated areas within hospitals to accommodate patients infected with airborne diseases (Hang et al., 2015; Saarinen et al., 2018). However, due to limited availability, most medical structures have only a small number of such rooms. For example, during the peak of the COVID-19 pandemic, emergency staff had to accommodate patients in rooms that lacked the negative difference of pressure. Even if management procedures may recommend that the doors of these rooms should not be opened, it is inevitable that routine assistance operations result in the infringement of this rule. Virus-laden aerosols can escape into common areas precisely because of these events. Also, hotel quarantine has been introduced by many governments in order to prevent virus transmission. Nonetheless, the lack of proper facilities in such hotels has led to reports of COVID-19 transmission linked to door openings. (Cheng et al., 2022; Wong et al., 2022). In addition, home quarantine is common among travellers and individuals with moderate airborne infectious diseases, making the home an important site for virus transmission. During home quarantine, infected individuals typically isolate themselves in enclosed rooms with balanced air pressure. In this cases, air mixing and aerosol dispersion is an inevitable consequence of opening and closing doors for daily household activities (Mousavi and Grosskopf, 2016). Therefore, it is crucial to thoroughly investigate the impact of these events in the indoor environment (with or without the pressure differential). In the case of entry doors that communicate with the outside environment, the pressure conditions are difficult to predict, which further complicates the problem. In addition, it is important to note that when doors are opened and closed, people or equipment often pass through the doorway, further contributing to aerosol dispersion. Previous research has shown that factors such as the angular velocity of the door, the walking speed of individuals, and even the physical characteristics of a walking person have a strong influence on the patterns of aerosol fluxes (Fontana and Quintino, 2014; Hang et al., 2015; Mousavi and Grosskopf, 2016; Kalliomäki and Koskela, 2016; Tao et al., 2018). However, the interactions and relative importance of these factors are not fully understood, especially when the effects of convective motion due to heating systems are included among the variables.

1.2.2 Airflow and mixing in indoor spaces: initial research approaches

In this section we provide a starting point for studying the flow field and mixing in indoor environments (such as hospitals, hotels, airport terminals, civilian homes, etc.), especially due to human passage through doors. Analysing the scientific papers produced on the topic, a first line of research can be observed, with some initial studies investigating air exchange between two rooms caused by thermal gradients, and a second line that, in the same indoor environment, examines the influence of movements of human beings — also considered as heat sources — on ventilation systems.

To the first line of research belong works such as Linden and Simpson (1985), where laboratory experiments are used to simulate the movement of air due to temperature-induced density differences which drive gravity currents highlighting the utility of laboratory models for visualizing and quantifying air movement dynamics, or Lane-Seriff et al. (1987) where the authors used small-scale laboratory experiments with saltwater to model buoyancy-driven airflows, leveraging density differences instead of temperature changes. Kiel and Wilson (1989) studied the combination of buoyancy-driven counterflows caused by temperature differences and the pumping effect of a swinging door, that is a modeling condition, with the addition of the pumping effect, which is more closely related to the subject matter addressed in the present thesis. They found that buoyancy dominates at larger temperature differences and pumping effects becomes significant when temperature differences are small.

With reference to the second line of research, there is a first schematic approach in Sandberg and Mattsson (1992), where a human was modelled as a heated rod inside an indoor environment represented by a small-scale physical model filled with water. Another series of studies (Jha et al., 2021b,a) operates in similarity, using water as the ambient fluid, to model human movement. In these cases, the human is also represented as a moving cylinder travelling along a straight path through an air curtain, devices installed in open doorways of a building to reduce buoyancy-driven exchange flows across the doorway discharging a controlled stream of air.

A series of other works like Mattson and Sandberg (1994) and Mattsson (1996) have refined the approach in full-scale experiments, leading to the realization of experiments using breathing mannequins (Bjørn et al., 1997) with the observation of the effect of movements and breathing on the contaminant distribution in a displacement ventilated room.

The evolution of research on the subject has led to the use of Computational Fluid Dynamics (CFD) alongside the experimental approach, as well as investigations aimed at minimizing air exchanges caused by people passing through sensitive areas such as operating rooms in hospitals or cleanrooms. In Brohus et al. (2006), CFD is used to simulate the influence of people movements in an operating room introducing distributed momentum sources to simulate a movement through a LAF (Laminar Air Flow) field and a turbulent kinetic energy source for the small-scale local movements, while in Oberoi et al. (2010) CFD is used to simulate the resuspension of particles caused by human movement, an experimental condition conducted at full scale in a ventilated room where a human moved across the space and then began stomping their feet while stationary. Also in Wu and Lin (2015) full-scale experiments were conducted based on measurements at several points in a room to assess the air velocity induced by the passage of a mannequin (mannequin height was 1.70 m). Ansaripour et al. (2016) studied the particle transport and distribution as a function of different ventilation strategies. They found a remarkable concentration of particles in the breathing zone of a heated manikin. Furthermore, their results indicated that mixed ventilation systems resulted in lower mean particle concentrations in the breathing zone compared to displacement ventilation systems.

There is, therefore, an abundance of full-scale experimental situations.

1.2.3 Methods

Chen (2009) presented a comprehensive review of various techniques that are used to study and predict ventilation performance in buildings. The review started from analytical and empirical models, giving then particular attention to small-scale and full-scale experimental models. Eventually the author treated multi-zone network models, zonal models, and computational fluid dynamics (CFD). The results showed that, in recent years, the contribution to the research literature by analytical and empirical models has been minimal. Small-scale and full-scale experiments were mainly used to collect data for the validation of numerical models. On the other hand, multi-zone models showed improvement and emerged as the main tool for predicting ventilation performance in entire buildings. Zonal models had limited applications and could potentially be replaced by coarse-grained computational fluid dynamics models. CFD models proved to be the most popular, accounting for around 70 per cent of the literature reviewed. Several measurement techniques find application in small-scale experiments, making it possible to predict realistic ventilation performance in buildings or rooms at a reduced scale. The use of such models is more cost-effective than the use of full-scale buildings or rooms. However, it should be emphasized that the flow similarity between a small-scale model and a real room (or a building) is guaranteed if key non-dimensional flow parameters (such as Froude number, Reynolds number, Grashof number, Prandtl number, etc.) have the same value in both the model and the prototype. However, maintaining the same Reynolds and Grashof numbers can be a challenge when dealing with heat transfer in a ventilated space. In such cases, researchers may use liquids of different densities (e.g., fresh water and brine) to simulate thermal buoyancy. Otherwise, the experiments on a reduced scale may not be able to simulate the actual flow field with the desired accuracy, although they can provide valuable insights. For example, Livermore and Woods (2007) used a small acrylic tank filled with water to study natural ventilation in a building with multiple heating levels. They used an analytical model to determine the level of neutral buoyancy and the direction of flow, and the results closely matched those obtained from the small-scale model. Although models on a reduced scale are economical and effective for studying ventilation performance in the artificial environment, they face challenges in scaling down complex flow geometries, such as certain types of diffusers. The literature review shows that these models are mainly used to validate theory or numerical schemes, which are then able to predict ventilation performance in real cases (Mingotti et al., 2011, 2013, 2020a; Cao and Yu, 2022).

CFD models have been widely used to study indoor air quality, thermal comfort, fire safety, and more in various building types such as commercial buildings, residential buildings, schools, healthcare facilities, institutional buildings, and industrial buildings. In addition, CFD models have been used for studies in various other environments, including underground facilities, public transport vehicles, greenhouses, animal facilities and more. Norton and Sun (2006); Norton et al. (2007) have carried out a very comprehensive review of CFD applications, focusing specifically on ventilation studies in the food and agricultural industry. After precise and accurate calibration, numerical methods allow to analyse the air flow evolution and the aerosol concentration following the opening of a door. Several researchers have tried to use CFD to reliable predictions of aerosol transport. For example, Choi and Edwards (2012) have used large-eddy simulation (LES) and immersed boundary (IB) methods to investigate contaminant transport induced by human passage and door opening in a room. Although the IB method is an easier approach in the case of moving boundaries, it has limitations in terms of grid placement in the vicinity of these moving surfaces. As a result, its accuracy in capturing the physics of phenomena near the walls can be compromised. To address these challenges, Zheng et al. (2023) used a combination of boundary-conforming mesh techniques to accurately simulate the airflow and aerosol exchange through a swinging door in the presence of a moving manikin between two spaces at the same pressure. The authors have quantified the effects of door opening events and human movement on aerosol exchanges, providing a better understanding of the mechanisms controlling the transport and dispersion of aerosols related to the airborne transmission risk.

1.3 Research gaps and objectives of the study

1.3.1 Wind tunnel activities

Despite the large body of research on wind-driven natural ventilation, several aspects of airflow exchange in multi-room buildings remain insufficiently understood. Wind tunnel experiments have been widely used to investigate cross-ventilation flows and to characterize the indoor airflow field generated by facade openings. Early experimental studies such as Ohba et al. (2001) analysed the penetration of the incoming jet and the resulting indoor recirculation structures in cross-ventilated buildings, highlighting the strong dependence of airflow patterns on wind direction and opening configuration. More recent wind-tunnel investigations like Shirzadi et al. (2019) have provided detailed measurements of velocity fields and ventilation flow rates under different wind angles and surrounding urban conditions, showing that external flow characteristics strongly affect indoor airflow distribution. Chu et al. (2010) have considered buildings with internal partitions and demonstrated that internal openings can significantly influence ventilation rates and pressure distributions within multi-room configurations and the very recent contribution by Sudirman et al. (2024), that used LDA techniques to give wind tunnel measurements on realistic partitioned buildings, further confirmed that internal walls can substantially modify indoor airflow patterns and ventilation performance.

However, despite these advances, experimental investigations have mainly focused on global ventilation metrics, such as airflow rates through facade openings, pressure coefficients, or overall indoor velocity distributions. Even in studies considering internal partitions, measurements are generally performed at a limited number of locations inside the rooms, while the local airflow dynamics occurring at the internal opening between communicating rooms are rarely investigated in detail. In particular, high resolution experimental data describing the spatial distribution of velocity directly across internal openings are still scarce. Moreover, turbulence characteristics at these interfaces, such as turbulent kinetic energy and Reynolds stresses, have received very limited experimental attention, despite their potential influence on the momentum transfer and mixing processes governing room-to-room airflow exchange. Another limitation of the existing literature concerns the validation of simplified predictive approaches: the airflow through internal openings is typically estimated using Bernoulli-type orifice formulations based on pressure differences; however, the availability of datasets providing detailed velocity measurements at the opening between two indoor spaces, in the context of cross ventilation, remains scarce, and consequently comparisons between detailed velocity measurements and pressure-gradient-based predictions are limited. To address these gaps, the present study experimentally investigates the airflow dynamics at the internal opening between two communicating rooms using a reduced-scale (1:15) building model placed in a wind tunnel. Detailed velocity measurements were performed at more than forty locations across the opening, corresponding to a full-scale doorway, using hot-wire anemometry. Multiple facade opening configurations were analysed, considering different combinations of open and closed windows on both the windward and leeward sides in order to reproduce different wind-driven ventilation scenarios. In addition to the mean velocity field, turbulence characteristics at the opening were evaluated through the analysis of turbulent kinetic energy and Reynolds stresses. Furthermore, pressure differences between the two rooms were measured to quantify the driving pressure gradient and to assess the consistency between the experimentally observed airflow behaviour and simplified Bernoulli-based formulations commonly used in ventilation modelling. Within this framework, the present study addresses the following research questions: (i) How does the spatial distribution of velocity across the opening vary under different facade opening configurations? (ii) What turbulence characteristics (turbulent kinetic energy and Reynolds stresses) characterize the airflow at the doorway and how do they influence the air exchange between the rooms? (iii) To what extent can Bernoulli-based formulations derived from measured pressure differences reproduce the airflow behaviour observed experimentally at the internal opening?

1.3.2 Indoor human walking air mixing

The body of research on occupant-induced airflow in indoor environments has grown considerably. However, the influence of human motion on air exchange between communicating rooms remains poorly understood. Previous experimental studies have investigated wake flows generated by moving manikins or small bodies in single-room settings, often using CFD or PIV to capture near-body velocity fields (Tao et al. (2017); Lv et al. (2019)). Mingotti et al. (2020b) uses cylinders of different sizes moved in a small water tank on a motorized cart to simulate wakes generated by moving bodies, visualizing the trace of a dye and recording wake dynamics. While these studies provide valuable insight into wake formation and local mixing, they generally focus on single-room scenarios and do not quantify velocity fields in the receiving space, nor do they examine volumetric flows or air exchange through openings connecting adjacent rooms. Furthermore, the interaction between motion-induced flows and pre-existing pressure gradients or recirculation conditions in the receiving space has not been systematically addressed, nor have they been experimentally investigated at a reduced scale with a certain degree of realism, leaving a gap in understanding how transient human motion contributes to room-to-room airflow transfer. To address these gaps, the present study investigates the flow generated by a human model moving along a rail system between two connected rooms in a water-filled experimental apparatus operating under dynamic similarity conditions. The passage of the model at different velocities was monitored using multiple experimental techniques, including Ultrasonic Doppler Velocity probes and Particle Image Velocimetry, providing detailed velocity fields across several planes in the receiving room. The volumetric flow induced by the moving model was quantified, and additional experiments were performed under increased hydraulic loading in the receiving space to simulate a pressure surplus, allowing assessment of how motion-induced flows interact with adverse pressure gradients and affect the resulting air exchange. This approach provides high-resolution, quantitative data on both mean flow and turbulence generated by human motion across an internal opening, directly addressing the gaps identified in previous studies. Within this framework, the research questions addressed in this part of the study are: (i) What flow structures are generated by a moving occupant passing through an internal opening connecting two rooms? (ii) How does the velocity field in the receiving room depend on the speed of the moving occupant? (iii) What volumetric flows are induced by the passage of the occupant through the opening? (iv) How do pressure differences in the receiving space modify the airflow generated by occupant motion?

1.4 Dissertation overview

The present thesis aims to address the questions outlined in paragraph 1.3. The entire study, both regarding the wind tunnel cross-ventilation experiments conducted at the University of Granada and the experiments in a water-filled tank conducted at the University of Parma designed to investigate the influence of human movement between two rooms on indoor air exchanges between adjacent environments, has a strong experimental focus and seeks to propose new experimental approaches to the physical problems under investigation.

In particular, Chapter 2 describes the starting materials and the specific characteristics of the two experimental setups used, as well as all technical features of the instrumentation, the calibration curves, and the similarity criteria employed, which justify the translation of the experimental activity with physical models to real-world scenarios. Chapter 3, on the other hand, focuses on the experimental procedures adopted to ensure full reproducibility of the experiments: specifically, the procedures applied by the author during the execution and programming of the tests are explained, and tables are provided that detail the specifications of each test for every activity performed. Chapter 4 is devoted to the discussion of the results from the wind tunnel experiments, while Chapter 5 presents the results from the water tank experiments involving human passage. Finally, Chapter 6 summarizes the overall work and presents the conclusions, also highlighting the practical implications for building ventilation and indoor airflow control.

Chapter 2

Materials and methods

2.1 Wind tunnel activities

The experimental activities presented in this section were carried out during a six-month research visit at the Laboratory of Environmental Hydraulics of the Andalusian Institute for Earth System Research (IISTA, University of Granada).

2.1.1 The wind tunnel

The wind tunnel at the IISTA of the University of Granada, constructed in 2004 and made of wood and *Plaxiglas*, is an open-circuit design. This means that it features an inlet and an outlet sections without a return circuit, significantly reducing construction costs. Open-circuit wind tunnels are typically constructed indoors. As a result, they can be considered similar to closed-circuit tunnels but with a less efficient air return system. IISTA wind tunnel, schematically represented in Figure 2.1, total length is equal to 22 m. Its closed test section is 13.6 m long, with a 2.15 m wide and 1.80 m high cross section, constant in the longitudinal direction. The tunnel is equipped with two entrances to allow the operator to access its interior for inserting physical models and instrumentation. Its test section has side walls made of *Plexiglas*, enabling visual inspection of the interior during testing. The turbine provided has a diameter of 1.70 m and operates in suction mode rotating from a minimum of 27 rpm to a maximum of 400 rpm generating inner wind velocities from 1 m/s to 15 m/s.

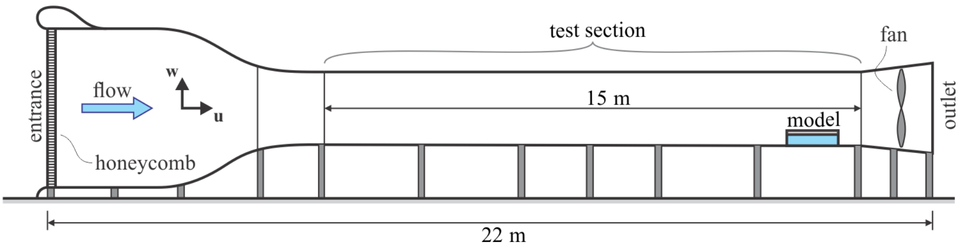

Figure 2.1: Section of the IISTA (University of Granada) open circuit wind tunnel.

2.1.2 Physical model

For this experimental activity, we conducted experiments on an apparatus with geometrical features similar to those of the setup that we used in the water experiments carried out in the Hydraulic Laboratory of the University of Parma and that will be described in section 2.2. Since the fluid used in this activity is air, the model was made of wood, with only one side wall made of *Plexiglas* to allow visual inspection of its interior. The model featured two confining chambers having inner dimensions of $500 \times 500 \times 300$ mm^3 and was positioned in the measuring section of the wind tunnel (Figure 2.1). The dividing wall between the two rooms, also made of wood, has an aperture of dimensions 65×150 mm^2, which simulates the presence of a door connecting the two environments. The geometric scale is $\lambda = 1{:}15$.

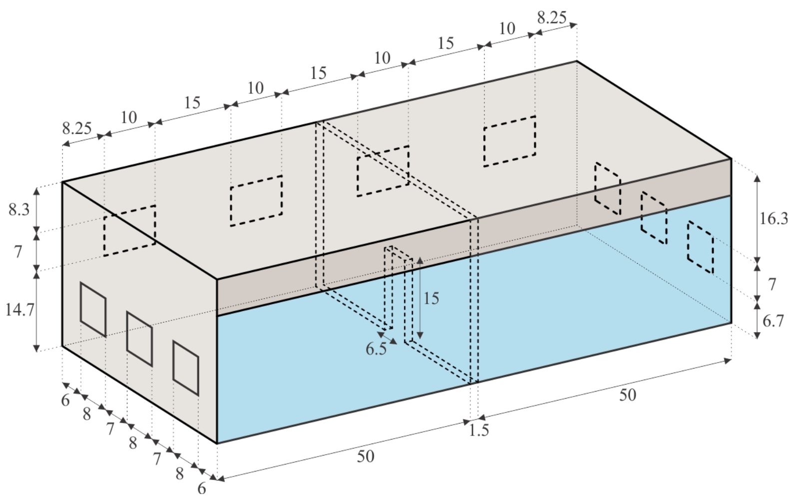

Figure 2.2: Isometric view of the tank in wood and *Plaxiglas* used for the experiments in the IISTA wind tunnel. Measures are in cm.

A set of three windows was created on both the upstream and downstream walls, which were perpendicular to the wind direction. Each opening has dimensions of 80 mm in width and 70 mm in height. Additionally, a second set of four larger windows, measuring 100×70 mm^2, is located on one of the side walls to simulate an industrial environment. Each opening can be closed independently to recreate various configurations. The model can be rotated around its vertical axis to vary the angle at which the wind blows on external surfaces. When the model was oriented parallel to the airflow inside the wind tunnel, that is, when the rotation angle was zero, the blockage ratio was 3.9 %. A hole was also made in the roof of the model, allowing the necessary instrumentation to directly enter its interior to perform velocity measurements.

2.1.3 Velocity measurements

To measure mass exchange between the two rooms of the model, we measured velocities at a section immediately downstream of the doorway using a hot-wire measurement system. From a practical standpoint, the hot-wire system allows penetration into the model through the hole in the roof due to the small size of the probe, which was specifically chosen with a right-angle design. To perform velocity measurements we used Constant Temperature Anemometer System Model IFA 300 by TSI Incorporated. It is a fully-integrated, thermal anemometer-based system that measures mean and fluctuating velocity components in air, water and other fluids. The device is capable of acquiring data on 8 channels, transmitting the acquired data to a personal computer via an A/D conversion board, where the proprietary software Thermal Pro is installed and provides up to 300 kHz frequency response.

For the present activity, we used a hot-wire probe by TSI, Model 1249A Miniature Cross Flow "X" Probe, mounted of a Dual Sensor Probe Support Model 1154-15. The arrangement of the measuring instruments can be appreciated in Figures 2.3 and 2.4. This type of probe consists of two hot-wire sensors paired in an "X" configuration, allowing the measurement of the two components u and w of air velocity contained in the plane formed by the two sensors with a frequency of 2 kHz. The probe support had two BNC connectors as output, one for each channel, which were directly connected to the IFA 300 anemometer via a 457.5 cm (15 ft) long cable. The probe support was attached to an additional structure we built, which was in turn anchored to a mechanical arm remotely controlled via software using a dedicated computer. This motorized mechanical arm, an integral part of the wind tunnel, allowed the probe to move along three relative Cartesian directions within the tunnel's internal space, ensuring the correct positioning of the probe at the designated measurement points.

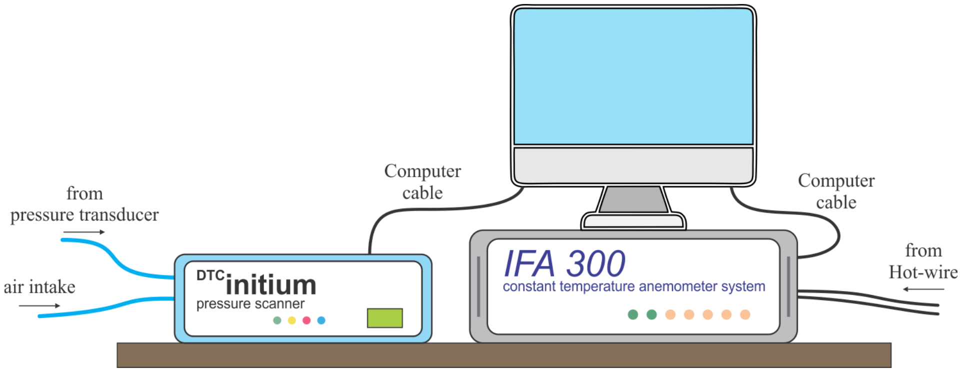

Figure 2.3: Acquisition hardware for experiments conducted in the IISTA wind tunnel.

At the start of each test, the hole on the top was opened to allow the hot wire probe to enter the model. The hole was then sealed before measurements began to prevent any air exchange through it.

2.1.4 Calibration of the hot wire anemometer

The hot-wire anemometric system is very delicate and sensitive to variations in environmental variables such as temperature and pressure. For this reason, calibrating the hot-wire anemometer was necessary at the beginning of each test day. For the calibration operations, a TSI Model 1129 Automated Calibrator was used, paired with a Pressure Transducer Type 220D by MKS Instruments. The automatic calibrator was first connected to a compressed air inlet. The air then passed through a nozzle with known dimensions, which allowed it to be delivered at controlled speeds. These speeds were indirectly regulated by a feedback system that measured the relative pressure using the pressure transducer connected to the calibrator. The hot-wire probe is attached to the calibrator and connected to the probe support, which in turn is linked to the IFA 300 anemometer. The calibration process is automatically managed by the Thermal Pro software. According to the procedure outlined in the instrument manual, the software automatically varies the air speeds during the calibration and, at the appropriate time, the operator varies the angle of incidence between the airflow and the hot wire by rotating the probe. This procedure allows to obtain a calibra-

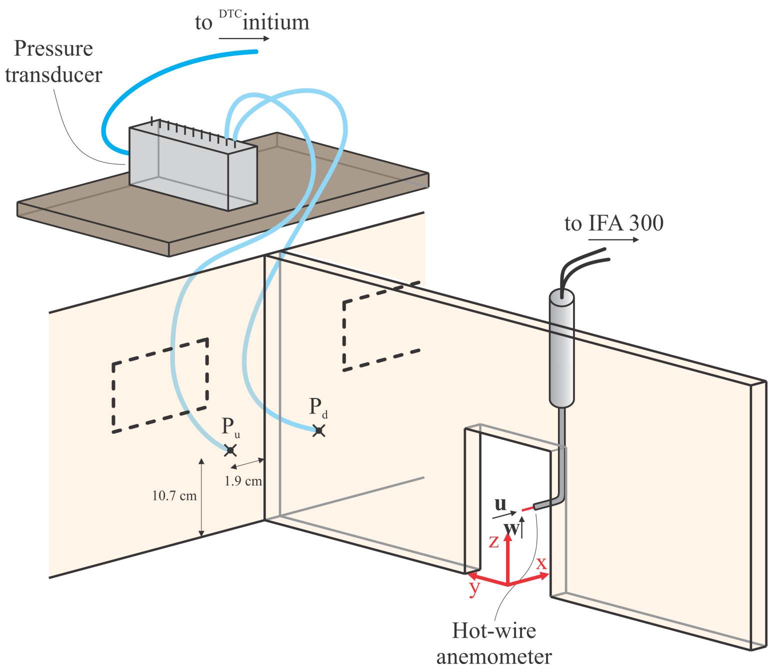

Figure 2.4: Detail of IISTA wooden tank, with the arrangement of the measuring instruments. P_u and P_d indicate the upstream and the downstream static pressure ports.

tion curve that associate specific air incident speeds with the corresponding probe's voltages output.

In Figure 2.5, we provide an example of calibration curve. Since the probe is of the "X" type, it is capable of measuring two orthogonal components of velocity and therefore uses two sensors. For this reason, as shown in the figure, there are two calibration curves, one for each wire. The points indicate the measured output voltage values as the incident velocity from the calibrator nozzle varies, while the two continuous curves represent an interpolation performed using a fourth-order polynomial. The five coefficients of the fitting polynomial are calculated by the Thermal Pro software and then used to convert the voltage values recorded by the sensors into measured velocities during the day's tests.

2.1.5 Athmospheric boundary layer

The lower part of Earth's Troposhpere is called Athmospheric Boundary Layer (ABL) or Planetary Boundary Layer (PBL). It is a layer in which

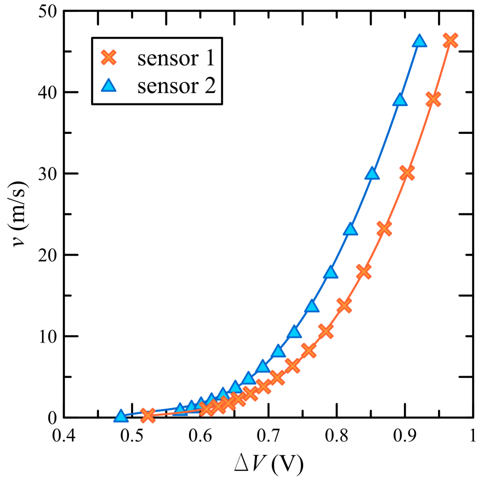

Figure 2.5: Typical calibration curve for the hot wire probe

interaction phenomena between the Earth's surface and the atmosphere occur, strongly influencing the behavior of the air in which human beings are normally immersed. At ground level, it is assumed that the air velocity is zero, which then generally tends to increase with distance from the ground until it reaches a region of the layer where the mean velocity value is ideally constant, known as the freestream velocity. The entire layer is affected by complex and intense turbulent phenomena.

In geometrically scaled flow simulations, Atmospheric Boundary Layer is stratified in two macro-layers: the inner wall layer, which is the layer closest to the floor and the region suitable for testing, and the outer wake layer, where the transition from the boundary layer to freestream conditions occurs (Catarelli et al., 2020). In turn, the inner wall layer is divided into roughness sublayer (RSL) and inertial sublayer (ISL), the region where Reynolds shear stress $\tau_{R_{xz}} = -\rho\overline{u'w'}$ is nearly constant.

To simulate a realistic ABL under modelling conditions, five panels with staggered arrays of foam blocks measuring $35 \times 40 \times 80$ mm^3 were installed at the entrance of the wind tunnel. Each panel had 15 rows of blocks, with each row containing 13 blocks. We measured a velocity profile $(u(z), w(z))$ with a freestream wind velocity $U_w = 10$ m/s in the empty tunnel at the model insertion section along the central vertical axis to characterize the ABL by evaluating the roughness length z_0. For each height z we acquired the horizontal and vertical velocity components with a frequency of 2 kHz for 120 s for each point. The z_0 parameter is derived from the classic logarithmic law 2.1 which describes the variation of the mean horizontal velocity $U(z)$ with measurement height z using the von Kármán constant $\kappa = 0.4$ and the shear velocity u_*

$$U(z) = \frac{u_*}{\kappa} \ln \frac{z-d}{z_0} \tag{2.1}$$

Equation 2.1 also includes the term d, i.e. the zero plane displacement or displacement height, defined as the height above the ground at which wind speed theoretically is equal to zero. As stated in Kunadi et al. (2024), this variable was originally introduced quite empirically but later studies have identified it, in real scale, as the elevation at which the mean drag force appear to act on the flow. The physical significance of parameter d has been investigated in recent years, for example in Catarelli et al. (2020), but it remains controversial. According to de Bruin and Moore (1985) and Dong et al. (2001), displacement height $d \to 0$ when the roughness elements are sparse and their density $\to 0$, due to the proportional relationship between these two variables, and it is a significant parameter only for tall vegetation. Given the above and since the use of large obstacles displaced with high density is not planned in the execution of this experimental activity, the value of the displacement height d has been set equal to 0. The equation 2.1 becomes:

$$U(z) = \frac{u_*}{\kappa} \ln \frac{z}{z_0}. \tag{2.2}$$

The region where it is possible to fit the measured values to equation 2.2 is the inertial sublayer. Before determining the roughness length value z_0, it is necessary to determine the shear velocity u_*. According to Weber (1999) and considering that the main direction of the flow is along the x-axis, the shear velocity is given as:

$$u_* = \sqrt{|\overline{u'w'}|}\,\Big|_{ISL} \tag{2.3}$$

Once the ISL of our profile, which, as shown in Figure 2.6, lies approximately between $z = 18$ cm and $z = 26$ cm, was determined, it was possible to calculate the shear velocity using equation 2.3, resulting $u_* = 0.54$ m/s. Then we applied the ordinary least squares method in order to adapt equation 2.2 to our data set considering only z_0 as free parameter. Referring to the real case, given that our modelling is at a 1:15 scale, we obtained a roughness length $z_0 = 6.15$ mm.

We also applied the ordinary least squares method considering both u_* and z_0 of equation 2.2 as two free parameters (2P). We obtained $u_{*,2P} = 0.45$ m/s and $z_{0,2P} = 1.95$ mm.

A qualitative correspondence of the obtained roughness length values is contained in Wieringa (1992): according to the Davenport-Wieringa roughness classification, a value $z_0 \approx 5$ mm is typical of smooth landscapes like fallow open country. Figure 2.6 shows the result of an acquisition performed

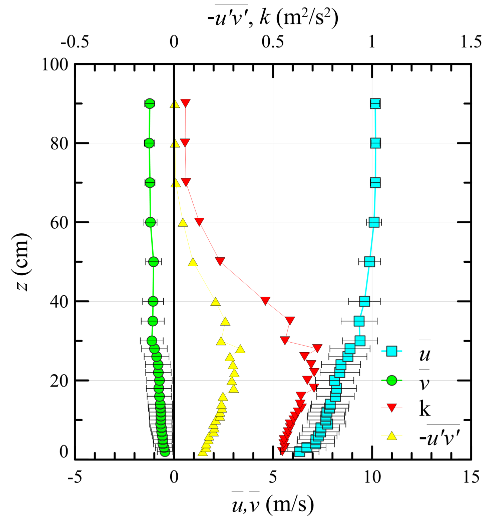

Figure 2.6: The graph shows the profiles of the horizontal and vertical velocity measured. Additionally, for each of the various heights, the Reynolds stresses and the turbulent kinetic energy, according to equation 3.1, are also shown.

in an empty tunnel with only the roughness-generating panels installed installed in the upstream part of the wind tunnel. Several points were acquired along a vertical line at the center of the tunnel's cross-section, corresponding to the area of the tunnel where the physical model is positioned. The analysis of these data, in light of what is illustrated in this paragraph, has allowed the evaluation of roughness length.

2.1.6 Pressure measurements

In parallel with the velocity measurements, pressure measurements were also conducted within the model under varying test conditions. Specifically, two holes were made, one for each chamber of the model, near the dividing wall. To create two static pressure ports, a PVC tube with an internal diameter of 1 mm was inserted into each of the two holes and connected to a pressure transducer ESP-32HD made by TE Connectivity. To ensure that there was no communication between the tube inserted in the hole and the external environment, it was sealed with silicone. The pressure transducer was, in turn, connected to the pressure scanner, DTC Initium by TE Connectivity. This pressure scanner was further connected to a computer via Ethernet for data acquisition and to a compressed air supply, the latter connection providing a reference for the device during the measurements. The pressure scanner had a range of 996 Pa and an accuracy equal to 0.15% FS and the whole pressure measuring system can be seen in figures 2.3 and 2.4. For each of the tested configurations, we measured the pressure gradient Δp between the two rooms.

2.1.7 Similarity criteria

In order to ensure that the flow in the model and prototype is in similarity, the experiments have been designed to respect the geometrical similarity, kinematic and dynamic similarity (i.e. with the same Reynolds number in both the model and the prototype). The Reynolds number is defined as $Re = ul\rho/\mu$, where u is the averaged velocity characterising the process, μ is the dynamic viscosity, ρ is the density, and l is the characteristic length scale. In order to reproduce turbulent phenomena in similarity, it is necessary that the ratio of the Reynolds numbers be equal to one, that is to say that

$$\frac{Re_p}{Re_m} = 1 \tag{2.4}$$

where Re_p is the Reynolds number referred to the prototype, while Re_m is the Reynolds number referred to the model. This means that the two Reynolds numbers must be at least of the same order of magnitude assuming to be in a fully developed turbulent flow regime.

Consequently, in order to have both kinematic and Reynolds similarities satisfied, the following conditions must be respected, with density ρ_{air} and dynamic viscosity μ_{air} of air already reported in paragraph 2.2.7:

$$\begin{cases} r_t = \dfrac{\lambda}{r_u} \\ r_{\Delta p} = r_\rho r_u^2 \\ r_\rho r_u \lambda = r_\mu \end{cases} \tag{2.5}$$

In this case, the fluid used in the model and in the prototype is air, hence the scale ratio between the densities and viscosities is constant and equal to 1. In order to obtain a perfect dynamic similarity, $Re_p/Re_m = 1$, we obtain that $r_u = 1/\lambda = 15$. In our case, the Reynolds number is on the order of 10^5 based on a transverse model length of 0.5 m and a minimum air velocity inside the tunnel considered of 3 m/s in the wind tunnel. The range of wind speed variation at full scale for our tests is between 0.2 m/s and 0.67 m/s, corresponding to light air, which are also the most frequent conditions.

2.2 Water tank activities

2.2.1 Physical model

The main apparatus for the experiments conducted at the Hydraulic Laboratory of the University of Parma was a tank filled with water. This tank was built specifically for this activity assembling panels of *Plexiglas* (PMMA). The choice of *Plaxiglas* was driven by its transparency, which allowed us to use PIV techniques and high-speed cameras, and by its resistance to the applied hydraulic loads. We wanted to physically model an environment consisting of two rooms, with the only means of communication being an aperture, large enough for people to pass through, located on the shared wall. In designing the physical model, we took into account Italian legislation, and in particular D.M. 236/89, according to which the clear opening width of a door must be at least 80 cm. To facilitate the smooth conduct of experimental activities, it was decided to work at a 1:15 geometric scale. This scale allows to clearly observe the physical phenomena reproduced in the laboratory and to profitably measure all the physical quantities involved. The apparatus (Figure 2.7) consists of six panels of *Plexiglas*, 1 cm thick, assembled and glued together to form a rectangular tank with two environments. The first environment has inner dimensions of $600 \times 500 \times 400$ mm^3 and the second, slightly smaller, has inner dimensions of $500 \times 500 \times 400$ mm^3. The two faces of the partition panel has dimensions of 500×400 mm^2. This panel was cut to create the 65×150 mm^2 opening shown in Figure 2.7, that represent an aperture of 97.5×2.25 m^2 at the real scale, dimensions compatible with those of an apartment door.

2.2.2 Preliminary velocity measurements: UVP probes

In this paragraph, the equipment set up to carry out some preliminary velocity measurements will be described. This initial experimental configuration was used as a preparatory step toward the use of PIV (Particle Image Velocimetry) techniques, which will be discussed later. These data were used to gain a general understanding of the observed phenomenon, since they provide measurements along only a single vertical line, but also to size and select the most appropriate PIV configuration for measuring a

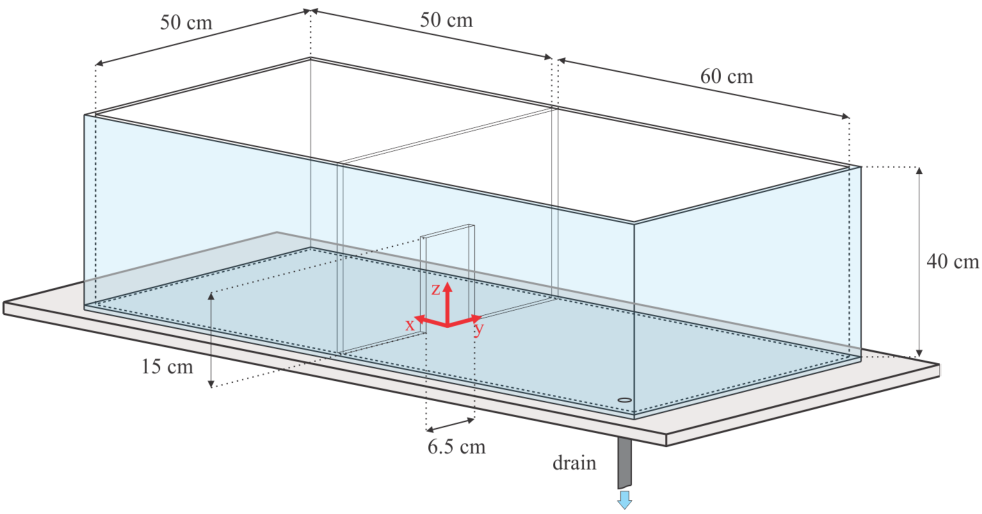

Figure 2.7: *Plaxiglas* tank used for experiments in water conducted at the Hydraulic Laboratory of the University of Parma. The reference system originates at the midpoint of the opening.

given velocity range, and to obtain a general idea of the velocities generated, allowing comparison with the data obtained using PIV. In order to perform velocity measurements in water, we used Ultrasonic Velocity Profilers (UVPs), also called Ultrasonic Doppler Profilers (UDPs). The UVP measurement technology is based on the emission and subsequent reception of ultrasonic acoustic signals by the UVP probe (transducer) within a liquid containing an appropriate tracer. A part of the acoustic energy emitted is partially scattered by the tracing particles as they pass through the probe's measurement beam and reflected back to it. By comparing the emitted and received signals, which are shifted in frequency due to the Doppler effect, it is possible to measure the fluid velocity at various points along the probe's axis, thus obtaining a one-dimensional velocity profile. During the preparation of every test, TiO_2 tracer particles were suspended into the fresh water contained in the tank. To take our measurements, we used two transducers, with a carrier frequency of 1 MHz, connected to an UVP (Signal Processing, Switzerland, model DOP 2000, year 2005). Since the ultrasonic energy is subjected to lateral spreading, the measuring volume of each transducer is a cone with a half diverging angle of 3°. The piezo diameter of each transducer is equal to 14 mm and Figure 2.8 shows the placement of the two UDP probes on their support, which was then positioned inside the tank. This particular arrangement, with probe 1 inclined at −25° and probe 2 inclined at 5° both respect to the vertical, allows us, by using a suitable transformation matrix, to convert the measured velocity components of each profile along the transducer's axis into components referring to a suitable Cartesian coordinate system. The velocity profile was measured at multiple spatial positions (gates), starting 15 mm ahead of the probe head, with each recorded velocity value of the profile assumed to correspond to the center of the measurement volumes. The details of the measurement procedure and the transformations applied to the raw data will be described in paragraph 3.2.1. Since all our experiments are conducted using fresh water, no correction is needed on the velocity values recorded by DOP 2000 due to variations of the standard velocity c of ultrasounic waves in water

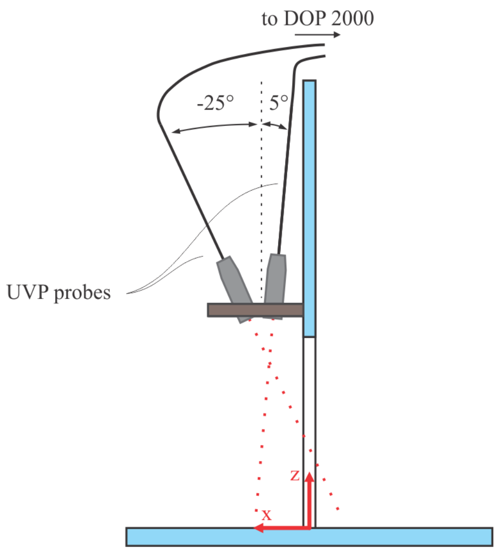

Figure 2.8: Detail of the UVP probes, with their rotation with respect to the vertical. The figure includes a schematization of their measurement cone.

2.2.3 Velocity measurements: PIV

Another experimental campaign carried out on the water testing apparatus involved the use of different and more sophisticated instrumentation. Specifically, the Particle Image Velocimetry (PIV) technique was employed, a technology based on the introduction of tracer particles into the fluid under investigation and the combined use of a laser capable of emitting light in the form of a two-dimensional plane and a camera able to capture images of the illuminated tracer particles at precise time intervals, according to user-defined settings. PIV technology, by providing instantaneous velocity fields over entire planes, offers a more comprehensive and spatially resolved dataset compared to the one-dimensional measurements obtained along a single vertical line with UVP probes. This extended coverage makes it possible to identify flow structures, detect spatial heterogeneities, and assess three-dimensional effects that cannot be captured with pointwise or line-based techniques. Moreover, the simultaneous acquisition of large-scale velocity distributions allows for a more robust statistical analysis of the flow, thereby reinforcing the reliability of the UVP-based measurements. The operation of the camera is synchronized with the emission of the laser beam by means of a timing controller. The adjustment of parameters such as the aperture and exposure time of the camera, as well as the laser beam intensity, allows the definition of optimal acquisition conditions. Image acquisition is performed in pairs; the user can define, based on the specific characteristics of the test being conducted, both the time interval between successive pairs and the time interval between the two images of each pair, Δt. Our experimental setup included an Optronis Cyclone-25-150 camera, featuring a resolution of 26 megapixels (5120×5120 pixel) and operated at 150 fps, and an Optolution LD-PS/40 laser with a minimum pulse duration of 5 μs, a peak optical power of 20 W and a double-pulse repetition frequency up to approximately 17.5 kHz.

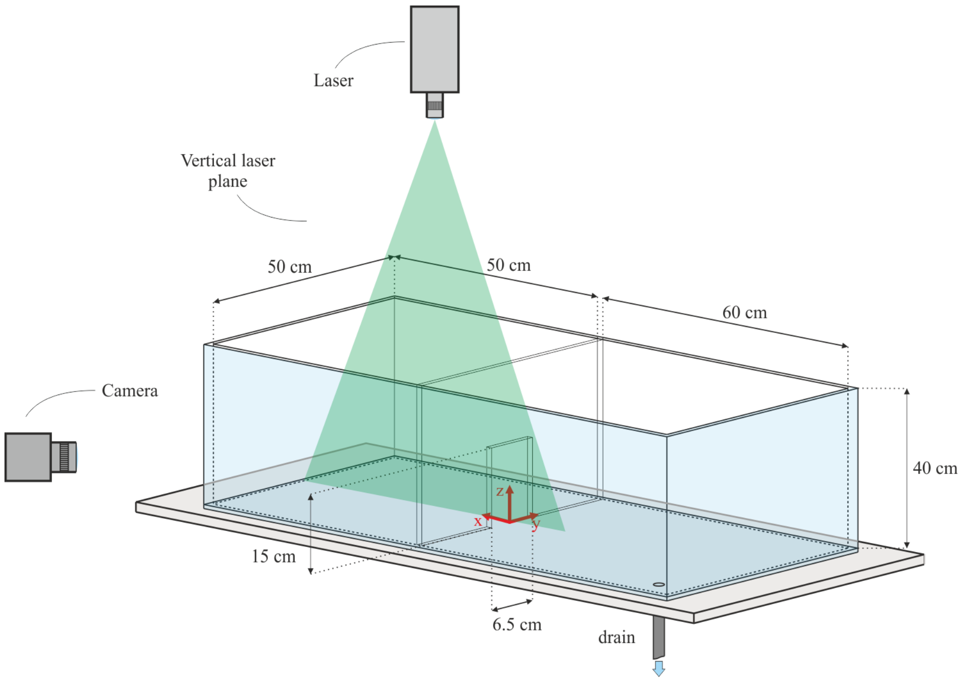

Figure 2.9: *Plaxiglas* tank used for experiments in water conducted at the Hydraulic Laboratory of the University of Parma with the camera and laser installed for experiments using the PIV technique. In this case the position of the measurement plane is vertical and expressed by equation $y = 0.6$ cm.

2.2.4 Modeling inhabitant flow

In order to model the passage of a human being between the two rooms, we installed a stainless steel rail at the bottom of the tank, on which a trolley was free to slide. The rail was positioned as in figure 2.10 and 50 cm long, with an effective stroke of 47.5 cm and the top surface of the trolley was at a height of 1.7 cm from the bottom of the tank. On the trolley we placed a foosball figure 11 cm tall, which was thus able to move from one room to another through the aperture. The movement of the dummy on the cart was made possible by a nylon thread to which it was attached. The thread was wound and unwound on a steel pulley with a diameter of 11 cm located out of the tank by a motor that allowed it to rotate. Simultaneously, the movement of the figure caused a small opaque target, positioned outside the tank, to go up and down thanks to a series of smaller plastic pulleys, with diameters of 1.5 cm. The target's position was recorded by an ultrasonic distance meter (U-GAGE S18U by Banner Engineering Corp., Minneapolis

(USA), 2005). The ultrasonic distance meter measured the position with a frequency of 100 Hz and an accuracy on the order of a millimetre. This device allowed us to determine the dummy's position along the rail in real time. The coupled operation of the motor, which could be activated or deactivated depending on the position of the dummy along the rail, and the ultrasonic distance sensor was controlled by the LabVIEW software. The voltage supplied to the motor generated a corresponding and controllable velocity of the dummy along the U_m rail.

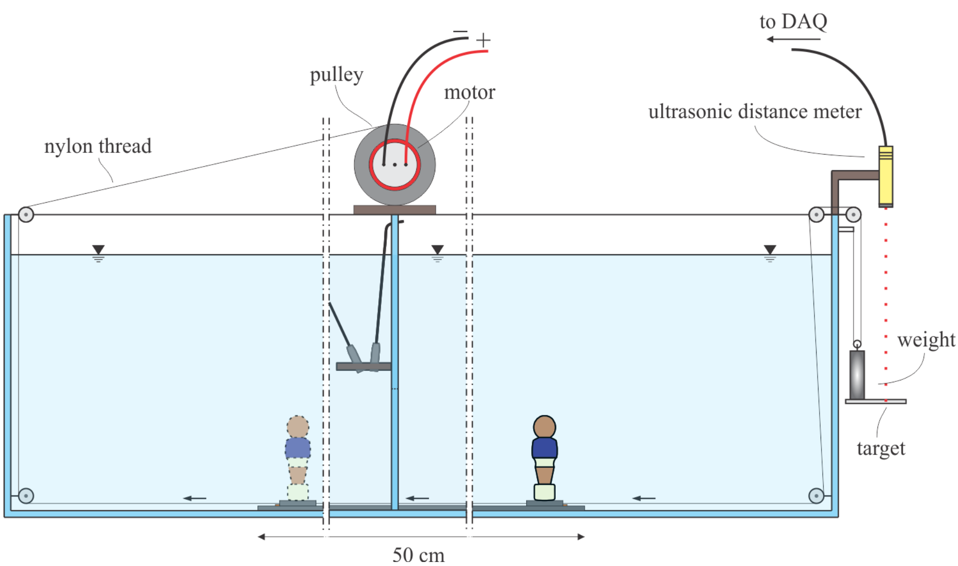

Figure 2.10: Section of the *Plaxiglas* tank shown in Figure 2.7 used for the water experiments. It is possible to appreciate the details of the motor and of the Ultrasonic distance meter. The initial position of the dummy is represented on the right, with arrows indicating the direction of the dummy from the starting room to the destination room.

2.2.5 Configurations with imposed pressure gradient

To model the possible air flow between the two rooms, or when the dummy's destination room is under overpressure, two additional configurations of the experimental setup were developed.

The first configuration (the one with water recirculation, Figure 2.11) included the installation of a pipe in the destination room capable of introducing water, shielded by a flow straightener (a 10 cm wide honeycomb, characterized by hexagonal cells with major diagonal equal to 6 mm) to prevent the turbulence generated at the inlet area from compromising the measurements of the probes. The water was then recirculated by draining it out and reintroducing it into the circuit thanks to a pump capable of regulating the flow rates.

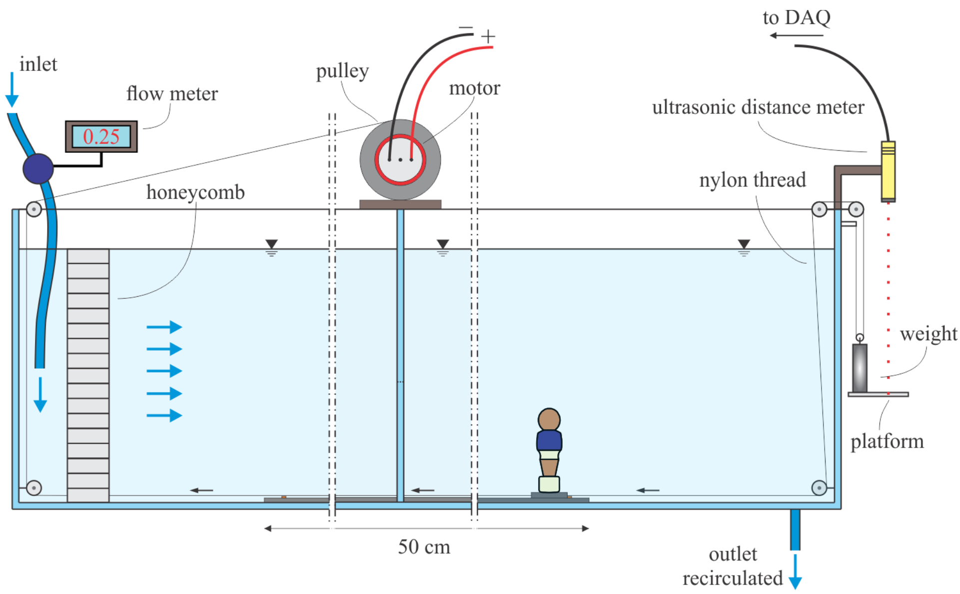

Figure 2.11: Section of the *Plaxiglas* tank shown in Figure 2.7 used for the water experiments with water recirculation. The initial position of the dummy is represented on the right.

The second configuration (the one with head-driven flow, Figure 2.12) involved the creation of a pressure gradient between the two chambers by filling the destination room of the model with a greater volume of water than that in the departure chamber. The closure of the opening between the two chambers by means of a gate ensured static conditions at the initial moment of the test. The instantaneous lifting of the gate initiated the return flow, together with the commencement of data acquisition and the beginning of the mannequin's motion.

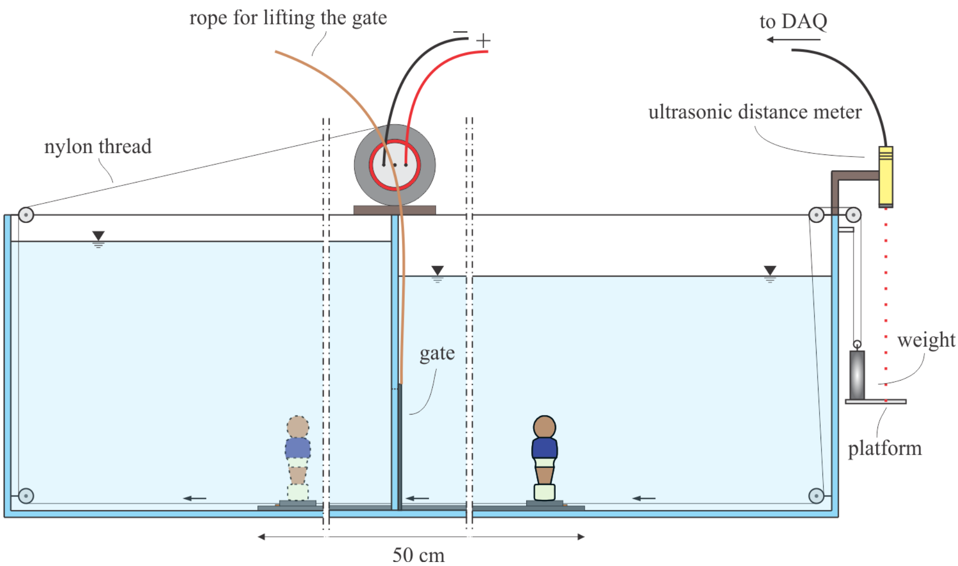

Figure 2.12: Section of the *Plaxiglas* tank shown in Figure 2.7 used for the water experiments with head-driven flow at time instants before the start of the test, with the gate lowered. The initial position of the dummy is represented on the right.

2.2.6 Calibration of the distance probe

As we mentioned in paragraph 2.2.4, for this experimental campaign we used an ultrasonic distance sensor to detect the position along the probe's vertical axis of the opaque target and, consequently, the dummy's position on the rail. Due to the specific arrangement of the counterweight and pulleys, as shown in Figure 2.10, the position changes of the opaque target along the probe's measurement axis were halved compared to the actual position changes of the dummy along the track. Before the beginning of the experimental campaign we calibrated the US distance meter obtaining the curve in Figure 2.13.

In Figure 2.13, the calibration points, acquired for a time of 10 s each, have been interpolated with a linear fitting, represented by the solid blue line, whose slope is equal to -0.03736 and intercept equal to 11.22 V.

2.2.7 Similarity criteria

In order to ensure that the flow in the model and prototype is similar, the experiments have been designed to respect the geometrical similarity, the

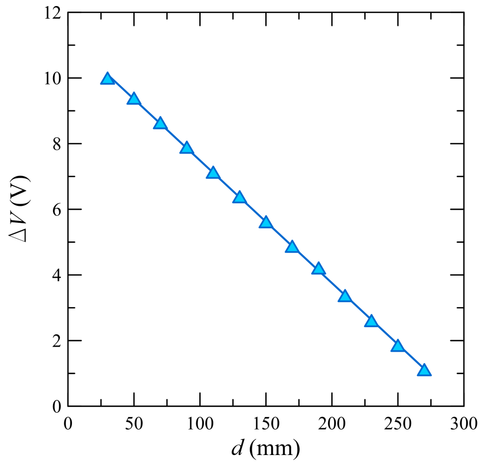

Figure 2.13: Calibration curve for the US distance meter

gravitational similarity (i.e. with the same Euler and Reynolds number in both the model and the prototype). The Reynolds number is defined as $Re = ul\rho/\mu$, where u is the averaged velocity characterising the process, μ is the dynamic viscosity, ρ is the density, and l is the characteristic length scale. In order to reproduce turbulent phenomena in similarity, it is necessary that the ratio of the Reynolds numbers be equal to one, that is to say that

$$\frac{Re_p}{Re_m} = 1 \tag{2.6}$$

where Re_p is the Reynolds number referred to the prototype, while Re_m is the Reynolds number referred to the model.

Consequently, in order to have both kinematic and Reynolds similarities satisfied, the following conditions must be respected, where densities are $\rho_{m,H_2O} = 1000$ kg/m^3 and $\rho_{p,air} = 1.20$ kg/m^3, and dynamic viscosities are $\mu_{m,H_2O} = 1$ mPa $\cdot$ s and $\mu_{p,air} = 1.8 \cdot 10^{-2}$ mPa $\cdot$ s:

$$\begin{cases} r_t = \dfrac{\lambda}{r_u} \\ r_{\Delta p} = r_\rho r_u^2 \\ r_\rho r_u \lambda = r_\mu \end{cases} \tag{2.7}$$

Given that the scale ratio between densities and viscosity is fixed (depending on the choice of fluids), it can be concluded that only one degree of freedom is preserved. For $\lambda \approx 1/15$, this results, in our specific case where air is the prototype fluid and water is the model fluid, in $r_u \approx 1$.

Chapter 3

Experimental procedures and tests performed

In this chapter, the experimental practices adopted during the experimental campaigns for data acquisition for this work will be described and explained.

3.1 Wind Tunnel activities

As reported in the previous chapters, the purpose of the activity was to characterize the flow field generated in two interconnected rooms separated by an opening, both subjected to the action of a pressure gradient induced by the external wind entering the indoor environments. In addition to the characterization of the flow field, the acquired data were also used to determine the flow rate passing from one room to the other under various experimental configurations, i.e. with different boundary conditions, which will be thoroughly presented in this chapter. This transiting flow rate, measured using a hot wire at multiple points within the same plane, formed the basis for a characterization of our experiments in which the dimensionless flow rate was expressed as a function of dimensionless groups obtained by combining some characteristic parameters of the phenomenon.

3.1.1 Experimental procedures

By experimental practices, we refer to the set of methodological choices and procedural measures implemented during test execution to acquire the data of interest. More specifically, this includes the chain of preparatory and concurrent operations essential both for the experimental setup and for its operational management throughout the testing phase.

To summarize what has been said so far, during the experimental campaign in the wind tunnel we carried out two types of measurements using two different instruments: velocity with the hot-wire system and pressure with a pressure transducer connected to two static ports inside the physical model. It is important to specify that, for a given set of experimental boundary conditions, i.e. configurations of the model with open or closed windows or its variable rotation angle relative to the mean wind velocity, the pressure measurements inside the model were taken subsequently to the wind velocity measurements near the opening between the model's internal environment. Furthermore, not all sets of boundary conditions for which pressure measurements were taken have corresponding velocity measurements and this is due to the fact that velocity measurements are more labor-intensive than pressure measurements, due to the delicate placement of the hot wire inside the physical model and the longer measurement time, which depends on the high number of points at which the velocities were measured.

The velocity measurements with the hot wire (see paragraph 2.1.3 for specific details on the instrumental setup) were taken at points on a homogeneous grid within the plane which had the same dimensions as the opening between the two rooms and was placed 0.5 cm downstream of the opening. As shown in figure 3.1, the measure points were selected so that they would be representative of the velocity values corresponding to areas dA. All the areas dA are equal, except for those at the lowest and highest elevations. Below and above those extremes, positioning the mechanical arm is quite challenging due to the delicacy of the hot wire and the risk of damaging it by bumping into the physical wooden model. We therefore measured the velocity values along three equidistant verticals located at $y = 2.167, 0, -2.167$ cm, with 14 points each, equally spaced at a height of $z = 1, 2, ..., 14$ cm (these coordinates refer to the reference systems shown in figure 2.4, 3.1 and 3.2).

3.1.2 Tests performed

Figure 3.2 shows in plan view all the combinations of windows open or closed adopted during the campaign. The configurations are marked with a letter of the alphabet and the closed windows are filled in red. In the same figure 3.2, it is possible to observe the direction of the model's rotation angle θ relative to the average wind speed in the tunnel $\vec{U_w}$.

As specified in paragraph 2.1, both speed and pressure data were collected for different configurations, and simultaneously, for all tests, the tem-

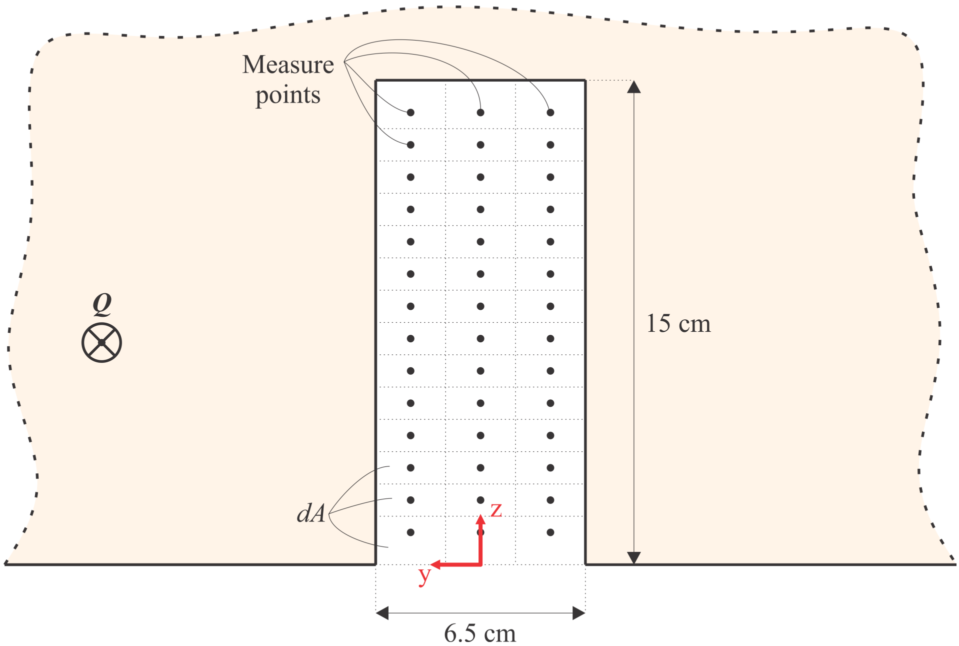

Figure 3.1: Cross-section of the physical model at the upstream partition wall. At the opening, all velocity measurement points and their corresponding influence areas dA are indicated. On the left, the flow rate vector entering the diagram is shown, as well as the reference system, depicted in red.

perature values within the tunnel were also measured, with the averaged temperature serving as a reference environmental parameter. The configuration called *ind* was tested only by measuring the pressure gradients between the two static ports located in the two rooms, visible in figure 3.2. The denomination *ind* refers to industrial-type environment, such as a large warehouse, with windows only in the upper part of the walls.

Tables 3.1 and 3.2 resume the tested configurations and the test conditions.

Configuration	U_w (m/s)	θ (°)
$\mathrm{A}_{U_w,\theta}$	10	0
$\mathrm{B}_{U_w,\theta}$	3, 5, 7.5, 10	0
$\mathrm{B}_{U_w,\theta}$	10	0, 15, 30, 45
$\mathrm{C}_{U_w,\theta}$	10	0
$\mathrm{D}_{U_w,\theta}$	10	0
$\mathrm{E}_{U_w,\theta}$	10	0
$\mathrm{F}_{U_w,\theta}$	10	0
$\mathrm{G}_{U_w,\theta}$	3, 5, 7.5, 10	0
$\mathrm{H}_{U_w,\theta}$	10	0
$\mathrm{I}_{U_w,\theta}$	10	0

Table 3.1: Tested configurations by measuring both the velocity with the hot wire at the designated points and the static pressure difference between the two rooms of the model.

Configuration	U_w (m/s)	θ (°)
$\mathrm{A}_{U_w,\theta}$	1, 2, 3, 5, 7.5, 10	0, 15, 30, 45
$\mathrm{B}_{U_w,\theta}$	1, 2, 3, 5, 7.5, 10	0, 15, 30, 45
$\mathrm{C}_{U_w,\theta}$	1, 2, 3, 5, 7.5, 10	0, 15, 30, 45
$\mathrm{D}_{U_w,\theta}$	1, 2, 3, 5, 7.5, 10	0, 15, 30, 45
$\mathrm{E}_{U_w,\theta}$	1, 2, 3, 5, 7.5, 10	0, 15, 30, 45
$\mathrm{F}_{U_w,\theta}$	1, 2, 3, 5, 7.5, 10	0, 15, 30, 45
$\mathrm{G}_{U_w,\theta}$	1, 2, 3, 5, 7.5, 10	0, 15, 30, 45
$\mathrm{H}_{U_w,\theta}$	1, 2, 3, 5, 7.5, 10	0, 15, 30, 45
$\mathrm{I}_{U_w,\theta}$	1, 2, 3, 5, 7.5, 10	0, 15, 30, 45
$\mathrm{ind}_{U_w,\theta}$	1, 2, 3, 5, 7.5, 10	0, 15, 30, 45

Table 3.2: Tested configurations by measuring the static pressure difference between the two rooms of the model.

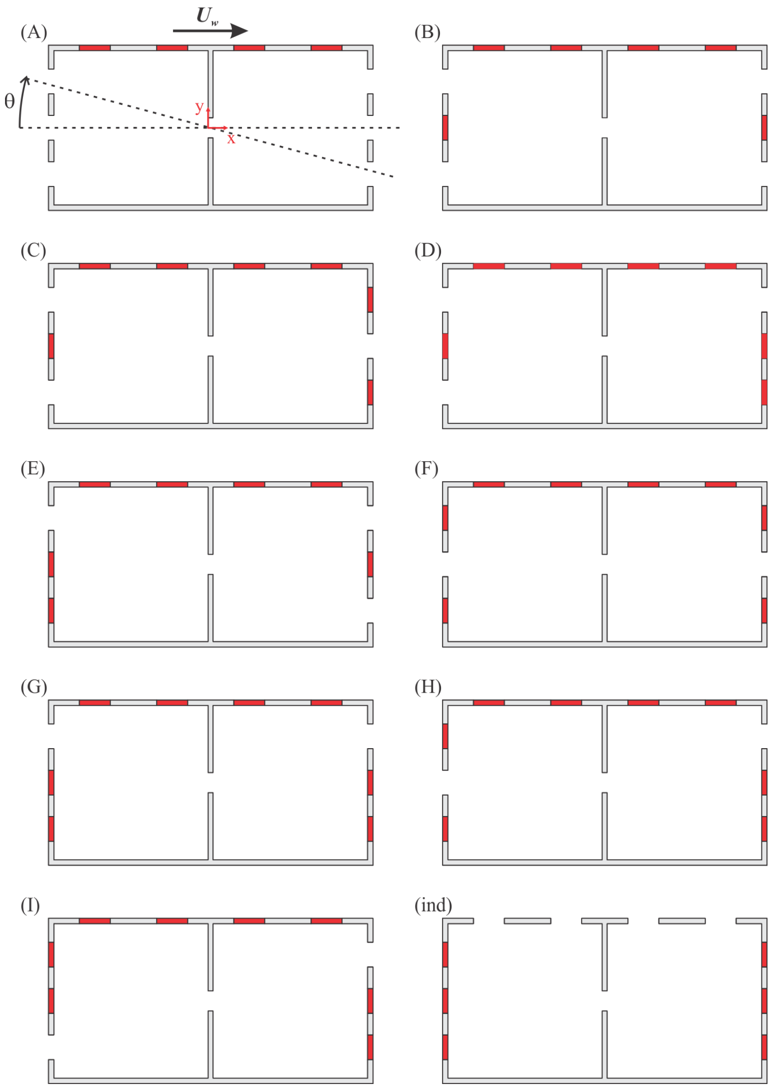

Figure 3.2: Plan view of all the configurations tested during the experimental campaign. Windows filled in red are closed. Wind velocity $\vec{U_w}$, model rotation angle θ and reference system x, y are also indicated.

3.1.3 Velocity field upstream of the model

In order to calibrate the system and to quantify the disturbance induced in the internal flow field of the tunnel by the presence of the physical model, the velocity profile was measured along a vertical line centred with respect to the tunnel cross-section, at a position located 3 cm from the outer wall and immediately upstream of the model. This preliminary investigation makes it possible to quantify how the presence of the obstacle, i.e. the physical model, modifies the turbulence pattern, and to determine the actual mean air velocity profile at the model's inlet. During these measurements, all windows of the model were kept closed. Instantaneous values of the horizontal velocity component $\boldsymbol{u}$ and the vertical component $\boldsymbol{w}$ were measured at 25 points spaced 2 cm apart, covering a height range from 2 cm to 50 cm. Given that the model height is 30 cm, the results are presented in figure 3.3. We have also included the empty tunnel velocity profiles to facilitate comparison.

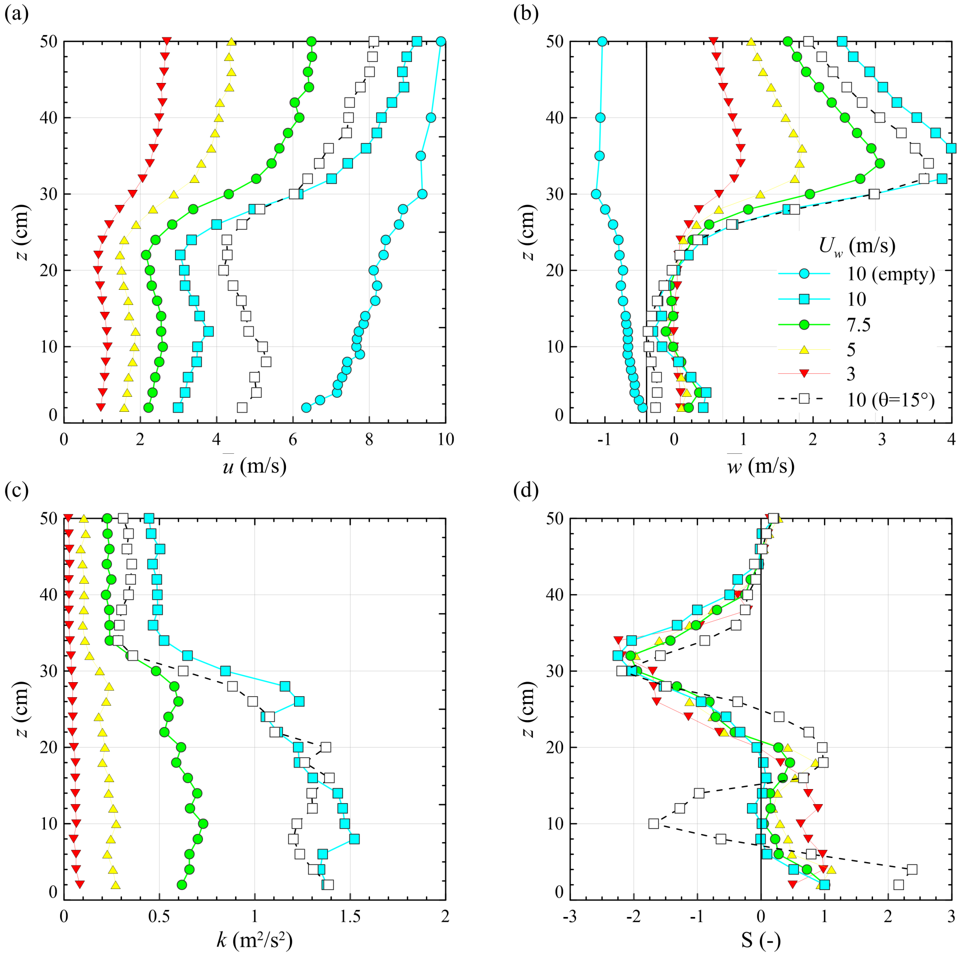

Figure 3.3: (a) Average horizontal velocity profile, (b) average vertical velocity profile, (c) Turbulent Kinetic Energy with varying height and (d) Skewness with varying height. These measurements were taken upstream of the model with all windows closed.

In figure 3.3, the legend reports the freestream velocity values, which correspond to standard rotation speeds of the wind tunnel fan. This allows a direct correlation between the operating conditions of the tunnel and the flow characteristics presented. The influence of the model wall on the velocity field is clearly visible in all the graphs. Compared to the empty tunnel case, there is a notable reduction in the mean horizontal velocity and a reversal in the sign of the mean vertical velocity, indicating a substantial modification of the flow induced by the wall.

The turbulent kinetic energy (TKE), defined as k in equation 3.1) represents the mean kinetic energy per unit mass associated with the velocity fluctuations $\overline{u'^2}$ and $\overline{w'^2}$:

$$k = \frac{1}{2}(\overline{u'^2} + \overline{w'^2}) \tag{3.1}$$

The level of turbulence, evaluated through TKE, increases with increasing freestream velocity. This trend suggests that higher incoming flow speeds enhance shear and vortex generation near the model wall.

The vertical skewness of the velocity fluctuations (Equation 3.2, where $\overline{w'}$ is the mean of the vertical fluctuations) exhibits an intermittent positive–negative pattern at heights corresponding to the top of the model wall.

$$S = \frac{\overline{w'}^3}{\left(\overline{w'}^2\right)^{3/2}} \tag{3.2}$$

This behaviour likely reflects the presence of coherent structures—such as vortices or ejections—that intermittently transport momentum upward or downward. Above this region, the skewness tends to stabilize around zero, indicating a transition to a more isotropic or statistically symmetric turbulence regime, where upward and downward velocity fluctuations become equally probable. The skewness of the vertical velocity fluctuations represents the asymmetry of the turbulence: positive skewness indicates that upward fluctuations are stronger or more frequent than downward ones, while negative skewness indicates the opposite. In terms of transport, it reflects the net transport of turbulent kinetic energy by the vertical velocity fluctuations themselves.

3.2 Water tank activities

This section details the procedures adopted during both the acquisition phase and the processing of the measured raw data. For both the UDP and PIV measurement systems, the determination of velocity components in the Cartesian plane is not straightforward; therefore, the post-processing techniques employed to derive the two Cartesian velocity components are also described.

3.2.1 Experimental procedures for UDP measurements

Each 1 MHz UDP probe, whose instrumental characteristics have already been described in Section 2.2.2, measured velocity along its approximate vertical axis with negative values when the fluid approached the sensor, and positive values when it moved away. In the UDP measurement technique, the gate represents an approximation of the specific point at which the velocity is measured by the probe, expressed in mm/s. Equations 3.3 and 3.4 illustrate the geometric manipulations performed to obtain the two Cartesian velocity components., where v_1 and v_2 are the velocity measured by probe 1, inclined at 5°, and by probe 2, inclined at −25°, respectively.

$$\begin{cases} u_p = \dfrac{v_1 - v_2\cos(30^\circ)}{1-\cos^2(30^\circ)} \\ w_p = v_2 - u_p\cos(30^\circ) \end{cases} \tag{3.3}$$

$$\begin{cases} u = u_p\sin(5^\circ) - w_p\sin(25^\circ) \\ w = -u_p\cos(5^\circ) - w_p\cos(25^\circ) \end{cases} \tag{3.4}$$

The conversion is performed in two stages. In the first system (equation 3.3), the measured velocities v_1 and v_2, which correspond to two non-orthogonal measurement directions forming an angle of 30°, are converted into the components u_p and w_p within the reference system defined by the orientation of the two probes. Subsequently (equation 3.4), these intermediate components are projected onto the orthogonal Cartesian x–z reference frame (see Figure 2.8), yielding the velocity components u and w. This procedure, which allows for the determination of the Cartesian components along a measurement vertical intersecting the two probe directions, constitutes an approximation; nevertheless, it remains consistent with the characteristics of UDP measurements, owing to the overlap of the measurement cones of the two probes. The DOP 2000 measurement system did not allow for simultaneous acquisition from the two probes, which operated in an alternating mode. Two measurement configurations were employed. The first configuration, used for all tests without recirculating flow, provided a velocity profile approximately every 35 ms; therefore, considering the alternating acquisition of the two probes, each acquisition sequence lasted about 70 ms. A total of 200 sequences were recorded, each consisting of 116 gates, resulting in an overall test duration of approximately 14 s. The second configuration, used exclusively for the tests with recirculating flow, involved a reduction in the number of gates to 80, with one profile acquired approximately every 94 ms, for a total of 120 sequences and a test duration of about 22 s. Although both measurement configurations are valid, the second configuration, despite its lower temporal resolution, allowed for cleaner data acquisition, with measurements less affected by noise and spurious spikes. The data measured by the two probes were then matched with the data related to the position of the miniature target along the track, also by inspecting the echo data, which allowed the x-coordinate of the dummy's entry into the measurement cone of the first probe it encountered—the one inclined at $-25°$ to be identified with reasonable accuracy. We emphasize that the instants of interest for the present study are the initial ones, corresponding to the passage of the miniature target and its associated pumping effect. Each test included a waiting period of 1 s before the start of the mannequin.

3.2.2 Experimental procedures for PIV measurements

For data acquisition and initial post-processing aimed at obtaining instantaneous velocities in time for each test, the free and open-source software PIVlab for MATLAB was used. Regarding image acquisition, the camera lens aperture was set to f/2.8, and the laser pulse length, coinciding with the camera exposure time, which coincided with the laser pulse duration, was set to 1173 μs. For all tests, execpt those characterized by head-driven flow, the time interval Δt between the two images of each pair was 2 ms, and a total of 300 image pairs were acquired at a frame rate of 150 fps, i.e. 75 pairs per second, resulting in a total acquisition time of 4 s. For tests characterized by head-driven flow (table 3.5), the time interval Δt between the two images of each pair was 0.2 ms, and a total of 290 image pairs were acquired at a frame rate of 145 fps, i.e. 145 pairs per 2 seconds, resulting in a total acquisition time of 4 s. The acquisition started simultaneously with the onset of the mannequin's motion, triggered by a synchronization signal exchanged between LabVIEW, which controlled the mannequin's movement, and PIVlab, which managed the PIV devices. The acquired images, with a resolution of 5120×5120 px^2, were subsequently processed by providing as input a reference image previously acquired for calibration and for the conversion of velocities from px/s to m/s. Several software-based filters were applied to improve image quality and to remove unwanted reflections. The resulting matrices had dimensions of 169×169, corresponding to the same number of velocity vectors u and w (or u and v, depending on the acquisition plane). Finally, these velocity fields were validated by removing erroneous vectors using the PIVlab software, employing a 2D Gaussian validation method.

3.2.3 Tests performed

Tables 3.3, 3.4 and 3.5 show the tests carried out during the two experimental campaigns, the first using UDP instrumentation, and the second employing PIV techniques. All tests, with the exception of those involving imposed pressure gradients between the two rooms, were repeated multiple times, as shown in the last column of the three tables, due to the high repeatability of the measurements, which made this approach feasible. This allowed the calculation of the ensemble mean of the velocity fields. In addition to the mean, the fluctuations around the mean were analyzed, as these are essential for the study of turbulence and its statistical characterization, as will be shown in the following paragraphs. This methodology enables not only the determination of the average flow behaviour but also a quantitative assessment of turbulent intensity and other relevant statistical properties of the flow.

For tests 1 to 18, a single repetition consisted of the following sequence: first the start of the acquisition with the system at rest and, in the case of PIV tests, either simultaneous or delayed by 1 second, the release of the dummy from the starting room. The dummy then travelled along the rail at velocity U_m and came to a stop at the end of the rail in the arrival room.

By contrast, for tests 19 to 23, each individual run generally followed the same procedure as the tests described above, although the operational details differed slightly. In these latter tests, the pressure gradient was generated, as anticipated in paragraph 2.2.5, by filling the destination room of the model with a greater volume of water. Communication between the two chambers was interrupted—prior to the start of the test—by a gate. The gate was then lifted at the moment the test commenced and the PIV measurements were initiated; simultaneously, the motion of the mannequin on the rail was started. The difference in elevation between the free water surfaces in the two chambers before the beginning of each test was kept constant and equal to 10 cm for each test; what varied was the waiting time of the mannequin before the start of its motion. This made it possible to investigate the mannequin's passage under varying mean return-flow velocities U_{hd}, and thus different corresponding flow rates Q_{hd}, measured at the moment it crossed the opening.

It is important to specify that the velocity U_{hd} was calculated as follows: first, the mean velocity was computed along a vertical line equal in height to the opening (15 cm) and located immediately downstream of it within the PIV acquisition plane. The value U_{hd} was then obtained as the average of the velocities thus determined over the last ten frames preceding the mannequin's passage through the doorway, i.e. averaged over a time interval of 69 ms. Q_{hd} was then obtained multiplying U_{hd} by the area of the opening between the two rooms.

Acquisitions then continued for a few additional seconds; however, the main focus of our experiment was the passage of the dummy and, at most, the first instants after its arrival. Once acquisition was completed, the dummy was returned to the starting position. At this point, the repetition was considered complete, and after a few minutes to allow the system to reach a state of complete rest, the next repetition was performed. The number of repetitions for the PIV tests was lower than that of the UDP tests, due to the higher sampling frequency of the PIV instrumentation. The tests with dynamic environmental conditions, performed at a later stage, were repeated only once due to the strong similarity between the ten-run averaged data obtained with the PIV technique and the data from a single run using the same technique. As shown in Table 3.4, two vertical laser planes were considered, one of which at $y = 0.6$ cm (coordinate system in Figure 2.7, aligned with the rail, and a horizontal plane at a height of $z = 9$ cm, in order to achieve a more comprehensive characterization of the velocity field. Figure 3.4 shows a comparison of the mannequin's position along the track over time for three different repetitions of Test 3, in which the subject's average velocity was 0.79 m/s. As can be observed, the time axis has been shifted so that zero corresponds to the x-coordinate of the opening.

Test number	U_m (m/s)	Repetitions
1	0.16	100
2	0.37	103
3	0.79	100
4	1.13	101
5	1.23	104

Table 3.3: Tests performed in the tank filled with water with ultrasonic doppler profilometers. U_m indicates the velocity of the mannequin in m/s.

Test number	U_m (m/s)	Q_r (l/s)	Plane (cm)	Repetitions
6		0	$y = 0.6$	10
7	0.58	0	$y = 3.6$	10
8		0	$z = 9$	10
9		0	$y = 0.6$	10
10	0.70	0	$y = 3.6$	10
11		0	$z = 9$	10
12		0	$y = 0.6$	10
13		0	$y = 3.6$	10
14		0	$z = 9$	10
15		0.05	$y = 0.6$	1
16	0.86	0.1	$y = 0.6$	1
17		0.15	$y = 0.6$	1
18		0.2	$y = 0.6$	1
19		0.25	$y = 0.6$	1
20		0.35	$y = 0.6$	1

Table 3.4: Tests performed in the tank filled with water using PIV techniques. U_m indicates the velocity of the mannequin in m/s and Q_r is the recirculating flow rate in l/s, if present, through the opening between the chambers in the direction opposite to the motion of the mannequin. The measurement plane is indicated in the coordinate system reported in the figure 2.7.

Test number	U_m (m/s)	U_{hd} (m/s)	Q_{hd} (l/s)	Plane (cm)	Repetitions
21		-0.31	2.98	$y = 0.6$	1
22		-0.38	3.68	$y = 0.6$	1
23	0.73	-0.44	4.27	$y = 0.6$	1
24		-0.53	5.17	$y = 0.6$	1
25		-0.60	5.81	$y = 0.6$	1

Table 3.5: Tests performed in the tank filled with water under the opposing head-driven flow configuration using PIV techniques. U_m indicates the velocity of the mannequin in m/s, U_{hd} and Q_{hd} indicate, respectively, the average velocity in m/s and the flow rate l/s of the flow generated by the pressure difference between the two chambers encountered by the mannequin as it crossed the opening. Both the velocity and the corresponding flow rate are in the direction opposite to the motion of the mannequin. As a convention, the velocity was assigned a negative sign to emphasize its opposition to the mannequin's velocity, while the flow rate was kept positive in order to allow comparison with the recirculating flow values reported in Table 3.4. The measurement plane is indicated in the coordinate system reported in the figure 2.7.

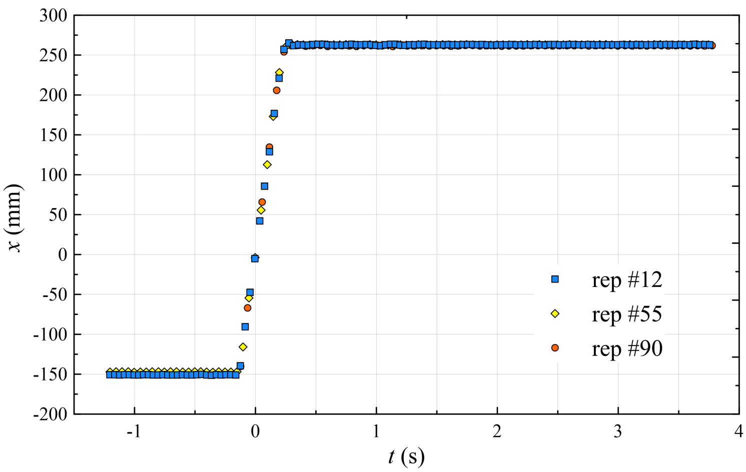

Figure 3.4: Position of the dummy along the track in function of time t (s) for repetitions 12, 55, and 90 of Test 3 (see Table 3.3).

Chapter 4

Results for Wind Tunnel activities

4.1 Dimensional analysis

In order to both understand the underlying physical processes and enable their formal mathematical description, all the relevant fluid mechanics quantities involved in the phenomenon were identified. The primary quantity of interest—i.e., the one to be expressed as a function of the others—was chosen to be the volumetric airflow rate Q through the doorway connecting the two environments. Equation 4.1 expresses Q as a function of the variables involved in the process, that are a caracteristic length L, air density ρ, the freestream wind velocity in the tunnel U_w, air dynamic viscosity μ, the area of the doorway A_d, the area of the window A_w, the pressure gradient between the two rooms Δp and the model's rotation angle θ measured with respect to the freestream wind direction in the tunnel.

$$Q = f(L, \rho, U_w, \mu, A_d, A_w, \Delta p, \theta) \tag{4.1}$$

At this point, dimensional analysis was used to identify the key non-dimensional groups that define the system's behaviour, and to observe how the flow rate Q varies with these dimensionless groups.

This approach offers two principal advantages: it reduces the number of independent variables by combining them into dimensionless groups, and it reveals the dominant physical mechanisms underlying the flow. In this context, the Buckingham Pi theorem was applied to derive a complete set of independent dimensionless parameters. These dimensionless Pi groups, obtained solely from the dimensional properties of the selected variables, allow the governing physical relationships to be reformulated in a more compact and general form—one that is independent of the specific units and directly applicable across a range of similar configurations. In the detailed application of the Buckingham Pi theorem, three independent fundamental quantities were selected from the relation 4.1: the characteristic length L, the density ρ, and the freestream velocity U_w. We have therefore expressed the remaining quantities as functions of the three fundamental ones, transforming 4.1 into 4.2 and retaining the rotation angle θ of the model, being a dimensionless quantity expressed in radians.

$$Q = L^2 U_w \, f_1\left(\frac{\Delta p}{U_w^2 \rho}, \frac{U_w L \rho}{\mu}, \frac{A_w}{A_d}, \theta\right) = L^2 U_w \, f_1\left(Eu,\, Re,\, \frac{A_w}{A_d}, \theta\right) \tag{4.2}$$

It is immediately evident from 4.2 that two of the non-dimensional groups correspond to well-established parameters in fluid mechanics: the Reynolds number, Re, and the Euler number, Eu.

Re quantifies the ratio of inertial forces to viscous forces in the flow. Its value indicates whether the airflow is predominantly smooth and laminar or chaotic and turbulent, an important index for predicting how air will mix and transport momentum in the flow.

Eu represents the ratio between pressure forces and inertial forces. In this context, the flow is driven by the pressure difference between the two rooms, while the freestream velocity of the air characterizes the inertial effects. This dimensionless parameter serves as an indicator of how effectively a given pressure differential drives the flow through the doorway, providing insight into the intensity of air exchange between the two spaces under varying pressure conditions.

4.2 Velocity field and turbulence

This section outlines some of the most interesting results obtained from the experimental campaign, the details of which are summarized in subsection 3.1.2. To analyse and characterize the flow through the doorway in selected cases of interest, the measured horizontal and vertical mean velocities ($\bar{u}$, $\bar{w}$) were first represented pointwise along vertical lines. Subsequently, the flow field was further characterized by examining specific turbulence parameters, whose computation requires a preliminary evaluation of the velocity fluctuations u' and w', defined as the instantaneous value of the wind speed minus the mean value.

Together with TKE (Equation 3.1), another parameter for the characterization of turbulence is obtained by dividing the Reynolds stress $\tau_{i,j}$, whose expression in the case under consideration is

$$\tau_{ij} = -\rho \begin{bmatrix} \overline{u_1'u_1'} & \overline{u_1'u_2'} \\ \overline{u_2'u_1'} & \overline{u_2'u_2'} \end{bmatrix} = -\rho \begin{bmatrix} \overline{u'^2} & \overline{u'w'} \\ \overline{w'u'} & \overline{w'^2} \end{bmatrix}, \tag{4.3}$$

by the fluid density ρ, and has the same dimensions as velocity squared $[L^2][T^{-2}]$:

$$\frac{\tau_{1,2}}{\rho} = -\overline{u'w'}. \tag{4.4}$$

The quantity used to characterize turbulence in equation 4.4 is the kinematic momentum flux, which quantifies the turbulent transport of momentum per unit mass. This metric reveals how turbulent fluctuations redistribute momentum within the flow.

In both equation 4.4 and the subsequent analysis, only the dominant component of the Reynolds stress tensor was considered—specifically, the term representing the vertical transport of horizontal momentum.

In Figure 4.1, the pressure difference Δp measured between the two environments is plotted on the vertical axis as a function of the freestream velocity in the tunnel and the rotation angle θ of the model. The graphs show that the pressure difference increases with increasing freestream velocity, which is consistent with the expectation that dynamic pressure scales quadratically with flow speed. When comparing the two configurations of plots a and b, it is possible to observe an average decrease of 30% in the pressure gradient when the number of open windows is reduced from 6 to 4. Interestingly, the measured pressure difference between the two rooms reaches its maximum values at intermediate rotation angles, specifically at 15° and 30°. In contrast, at the extreme angles of 0° and 60°, the pressure difference is significantly lower. This non-monotonic trend implies that the interaction between the model's orientation and the pressure-driven flow is non-linear and governed by complex aerodynamic phenomena. To highlight this behavior, the graphs in figure 4.2 have been produced. The data corresponding to configurations A, B, C, D and I, all of which share the common feature of having the window on the upstream wall in the bottom-left position open, exhibit a similar trend. Specifically, the pressure gradient Δp increases between $\theta = 0°$ and $\theta = 15°$, followed by a progressive decrease for higher angular values. At $\theta = 60°$, most of these configurations converge to

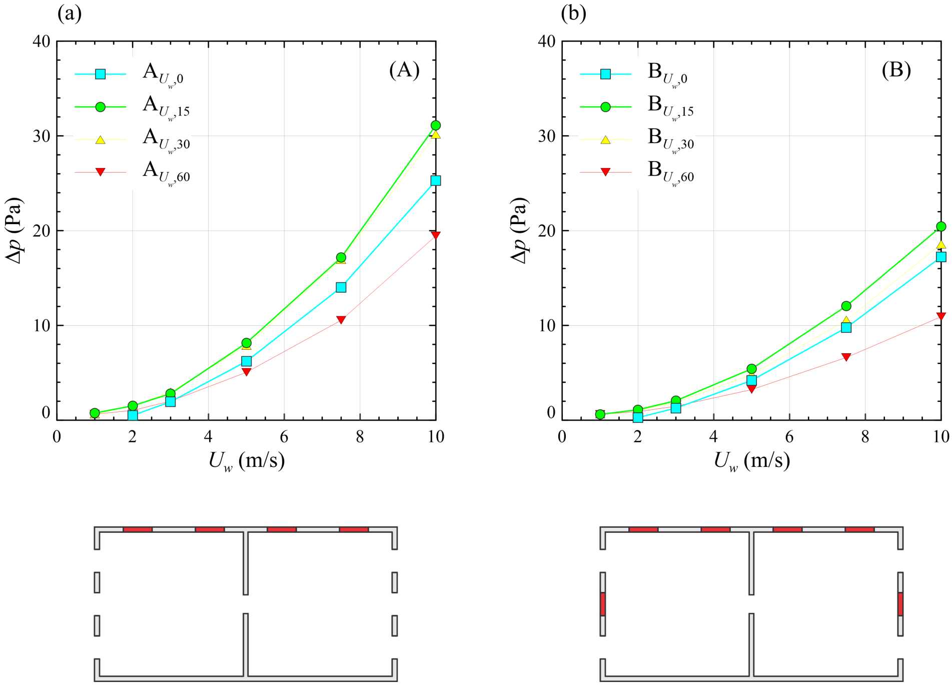

Figure 4.1: (a) Pressure difference, Δp, between the two rooms as a function of wind speed inside the tunnel, U_w, for different rotation angle of the model, θ, in configuration A; (b) pressure difference, Δp, between the two rooms as a function of wind speed inside the tunnel, U_w, for different rotation angle of the model, θ, in configuration B. Sketches of configurations A and B, extracted from figure 3.2, are also provided to assist the reader.

nearly the same value, with a pressure difference around 10 Pa, except for configurations A and I. Configuration A, which has all six windows open, shows a slightly higher Δp at $\theta = 60°$, while configuration I, characterized by having only two windows open, exhibits the lowest pressure gradient at this angle. As a result, configuration I exhibits lower indoor air velocity values, highlighting how both the number and arrangement of openings significantly affect the airflow dynamics. The nearly overlapping trends observed for configurations F and H can be explained by the fact that both configurations involve two open windows, one of which is the same window on the upstream wall, specifically the central one. The only difference lies in the choice of the open window on the downstream wall. This similarity in behaviour suggests that the specific location of the open window on the downstream wall exerts a limited influence on the overall pressure gradients. In other words, it appears that the geometric characteristics and the placement of the upstream window (or windows) opened play a dominant role in determining the ventilation behaviour, while the contribution of a single downstream opening is marginal. However, the number of openings on the downstream wall does prove significant. This is evident from the comparison between configurations E and G. In both cases, the same upstream window, the one in the top-left corner, is open. Yet configuration E includes two open windows on the downstream wall, whereas configuration G has only one. The resulting trend for configuration G can be interpreted as a downward-shifted version of configuration E, maintaining a similar shape but with lower pressure gradients across all values of θ. This shift reflects the reduced ventilation efficiency due to the smaller number of outlets on the downstream side. The greater pressure gradients observed in configuration E are therefore attributable to the increased capacity for air discharge, which amplifies internal airflow velocities. These observations reinforce the importance of both the number and the positioning of openings, particularly on the upstream wall, while also highlighting how the number of downstream openings significantly modulates the magnitude of pressure-driven flow within the model.

In configuration $\mathrm{ind}_{U_w,\theta}$, representative of an industrial shed fenestration system with windows open only on the long side of the physical model, negative pressure gradient values are observed at $\theta = 0°$ (figure 4.3). This indicates the occurrence of air recirculation from the downstream to the upstream room, driven by the flow conditions along the external lateral wall. As θ increases, the pressure difference becomes positive; however, it remains relatively modest throughout the angular range considered. It is also possible to observe the near-complete overlap of the measured data points for $\theta = 30°$, $45°$, $60°$.

Consequently, both the freestream velocity and the angle of rotation play a crucial role in determining the magnitude of the pressure-induced airflow between the two spaces.

We believe it is now useful to provide graphs similar to those in figure 4.1 also for cases of asymmetrical open/closed window configurations with respect to the horizontal axis of the physical model's floor plan. In particular, in figure 4.4, we compare configurations I and G, which are characterized by having only one open window per side, misaligned with the opening between the two rooms. It is first observed a sharp reduction in pressure gradients, although the overall trend remains parabolic, similarly to the cases shown in 4.1. As in the previous scenario, when the wind attack angles are $\theta = 15°$ and $\theta = 30°$, the pressure gradients tend to increase. Interestingly, even in

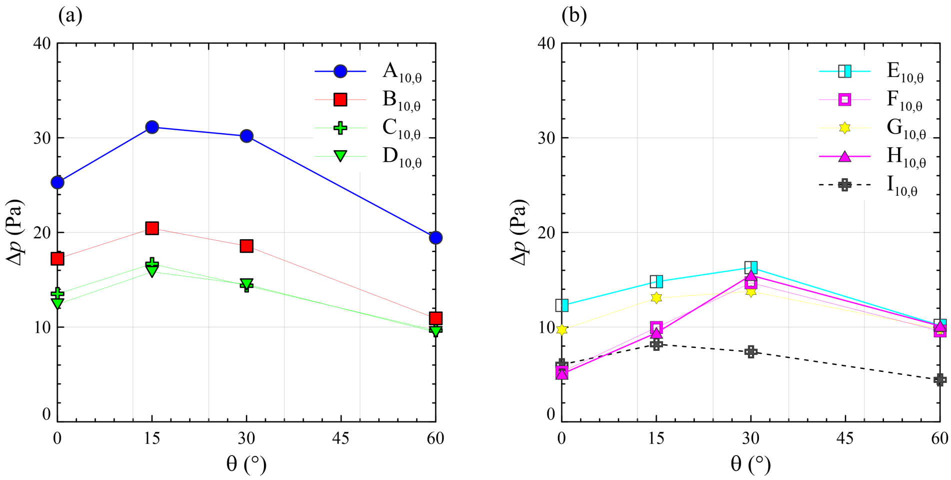

Figure 4.2: $(a,\ b)$ Pressure difference, Δp, between the two rooms as a function of model's rotation angle, θ, and with constant freestream wind velocity $U_w = 10$ m/s, varying with the configuration type, as named in figure 3.2.

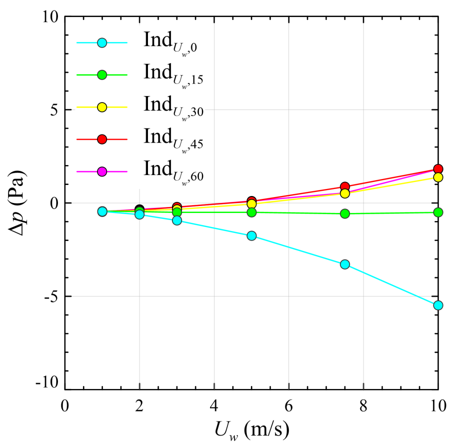

Figure 4.3: $(a,\ b)$ Pressure difference, Δp, between the two rooms as a function of freestream wind velocity, U_w, and with varying model's rotation angle θ, for the industrial configuration, as named in figure 3.2.

the case of $\theta = 0°$, the velocities reached in configuration G are higher than those in configuration I.

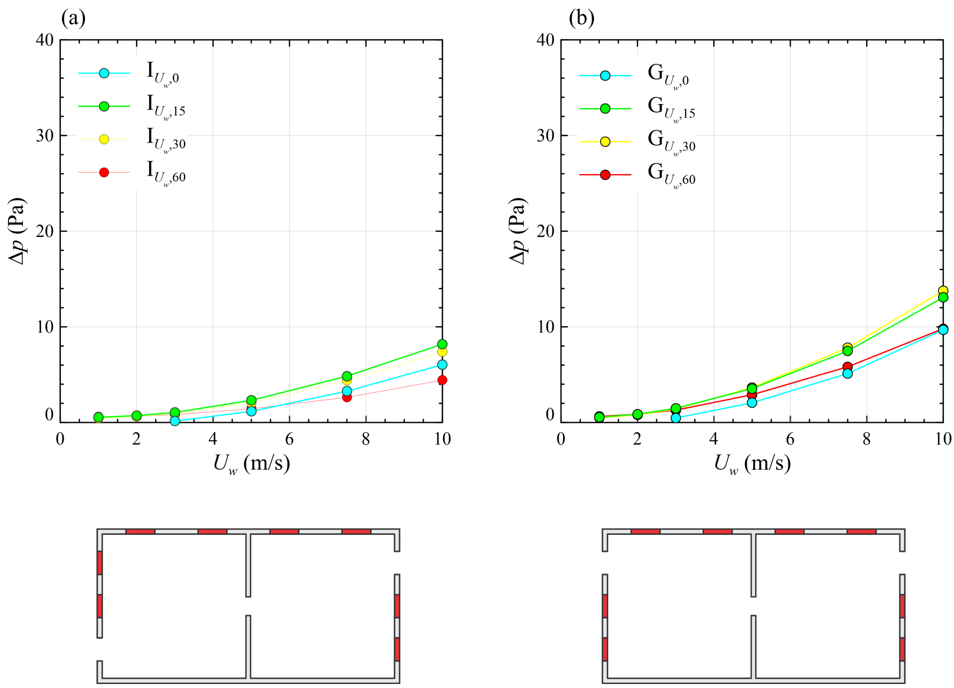

Figure 4.4: (a) Pressure difference, Δp, between the two rooms as a function of wind speed inside the tunnel, U_w, varying with the rotation angle of the model, θ, in configuration A; (b) pressure difference, Δp, between the two rooms as a function of wind speed inside the tunnel, U_w, varying with the rotation angle of the model, θ, in configuration B. Sketches of configurations A and B, extracted from figure 3.2, are also provided to assist the reader.

At this stage of the discussion, we present the results related to the turbulent phenomena observed at the measurement section. Figures 4.5, 4.6, 4.7 and 4.8 share the same structure: they show 2D contour plots of the door section, in panel a with the adimensionalized average horizontal velocities $\bar{u}_{adim}$

$$\bar{u}_{adim} = \frac{\bar{u}}{U_w}, \tag{4.5}$$

where $\bar{u}$ is the average horizontal velocity measured at the positions defined in Figure 3.1, and in panel b with the values of the adimensionalized turbulent kinetic energy (k_{adim})

$$k_{adim} = \frac{\sqrt{k}}{U_w} \tag{4.6}$$

at the same points, where k is calculated according to formula 3.1. We present the four configurations analysed in the previous section on pressure measurements for comparison.

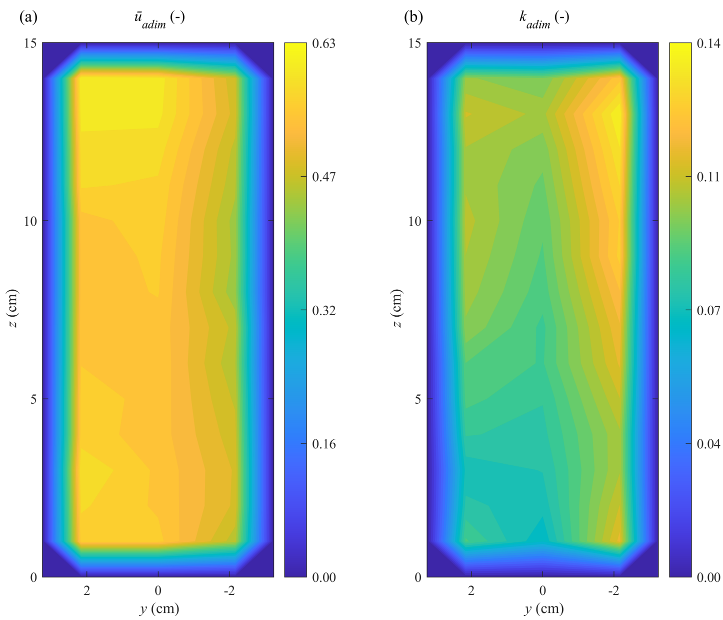

Figure 4.5: (a) Contour plot of the adimensionalized mean horizontal velocity $\overline{u}_{adim}$ for configuration A with $U_w = 10$ m/s and $\theta = 0°$; (b) Contour plot of the adimensionalized TKE k_{adim} for configuration A with $U_w = 10$ m/s and $\theta = 0°$.

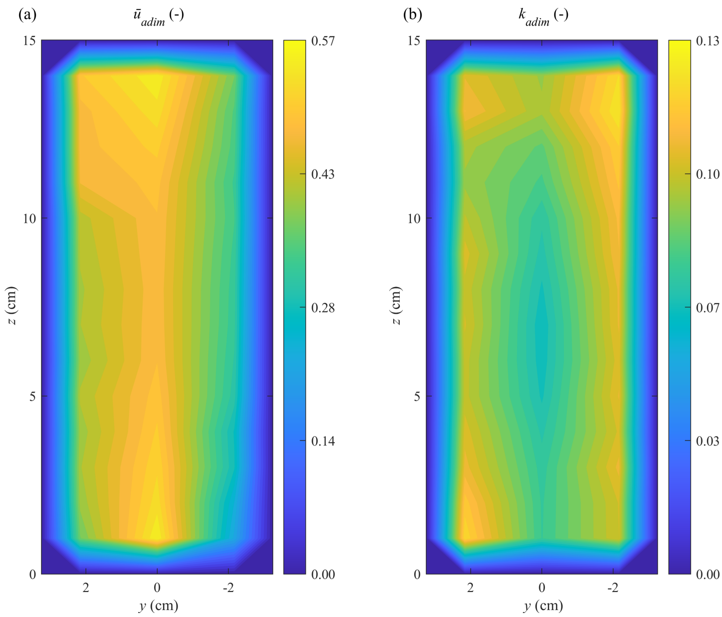

Figure 4.6: (a) Contour plot of the adimensionalized mean horizontal velocity $\overline{u}_{adim}$ for configuration B with $U_w = 10$ m/s and $\theta = 0°$; (b) Contour plot of the adimensionalized TKE k_{adim} for configuration B with $U_w = 10$ m/s and $\theta = 0°$.

In the colorbars of the graphs, the maximum value of the plotted variable has been explicitly indicated. Figures 4.5 and 4.6 demonstrate that symmetric configurations yield more symmetric contours. In addition to the expected reduction in velocity for configuration B with four open windows compared to configuration A with six open windows, a decrease in turbulent kinetic energy is also observed. The examination of the (b) graphs for configurations A and B further allows us to notice a certain symmetry in the distribution of k. In particular, the peaks are located at the edges of the door, and more specifically at the corners, as highlighted in Figure 4.6.

For the two asymmetric configurations, with only one window open per wall, the contour plots are shown in Figures 4.7 and 4.8. These plots reveal a reduction in the mean horizontal velocities, due to the reduced porosity of the model's windward wall, and, unlike what was observed for configurations A and B, peaks in turbulent kinetic energy along the central measurement vertical, especially close to the upper and lower edges of the opening.

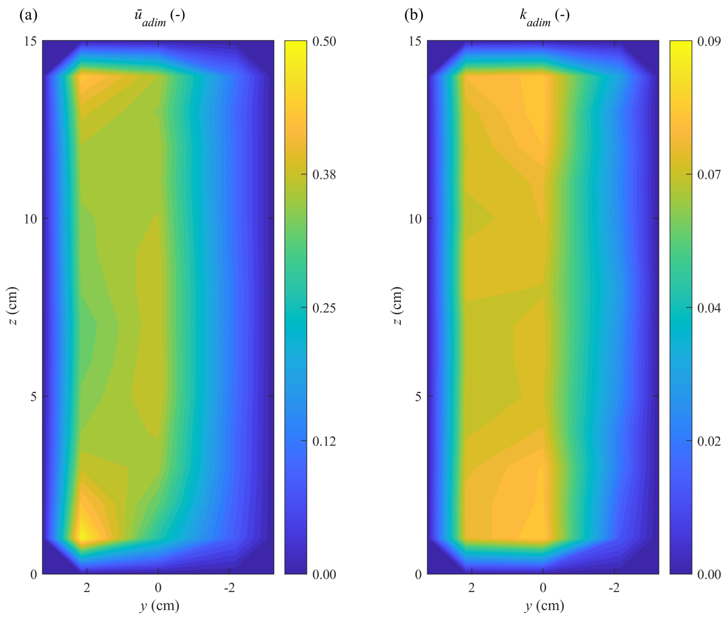

Figure 4.7: (a) Contour plot of the adimensionalized mean horizontal velocity $\overline{u}_{adim}$ for configuration I with $U_w = 10$ m/s and $\theta = 0°$; (b) Contour plot of the adimensionalized TKE k_{adim} for configuration I with $U_w = 10$ m/s and $\theta = 0°$.

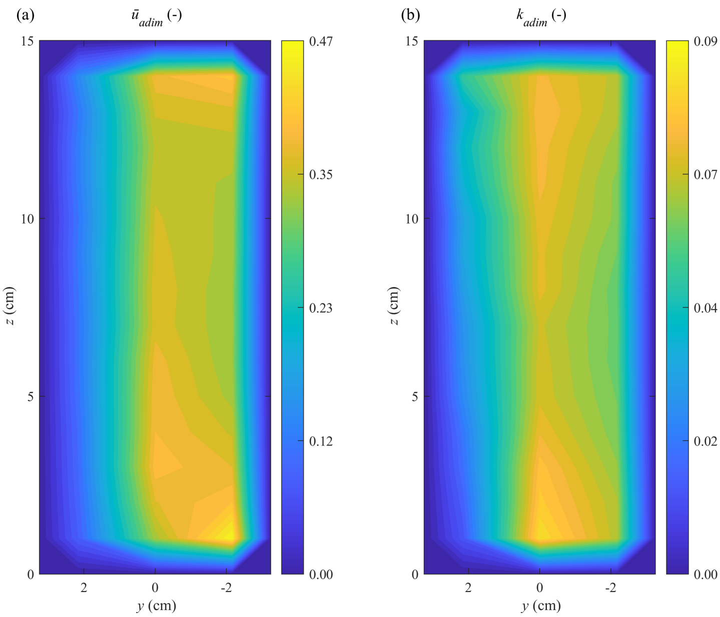

Figure 4.8: (a) Contour plot of the adimensionalized mean horizontal velocity $\overline{u}_{adim}$ for configuration G with $U_w = 10$ m/s and $\theta = 0°$; (b) Contour plot of the adimensionalized TKE k_{adim} for configuration G with $U_w = 10$ m/s and $\theta = 0°$.

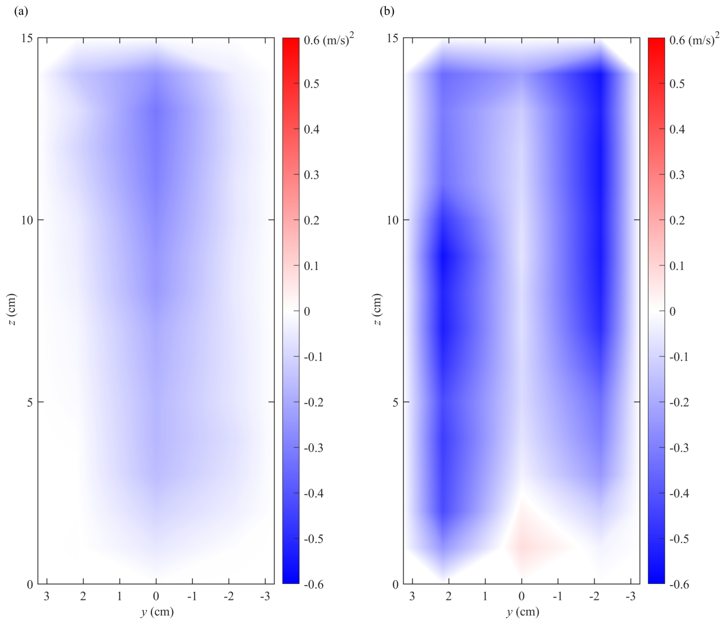

Figure 4.9: (a) Contour plot of the Reynolds stress $-\overline{u'w'}$ in m^2/s^2 for configuration G with $U_w = 10$ m/s and $\theta = 0°$, (b) Contour plot of the Reynolds stress $-\overline{u'w'}$ in m^2/s^2 for configuration B with $U_w = 10$ m/s and $\theta = 0°$.

Figure 4.9 shows the distribution of the Reynolds stress component $-\overline{u'w'}$ across the opening connecting the two rooms. Only two configurations are shown as examples: panel (a) refers to configuration G, while panel (b) refers to configuration B. The values are predominantly negative, especially in configuration B. Physically, this indicates that the horizontal and vertical velocity fluctuations, u' and w', are on average positively correlated in the measured region. In other words, when the horizontal fluctuation is positive, the vertical fluctuation also tends to be upward, resulting in a net upward turbulent transport of horizontal momentum through the opening. The spatial patterns highlight zones where turbulent momentum transfer is strongest, providing insight into local mixing and the redistribution of kinetic energy between the rooms.

4.3 Flow rate considerations

This section presents an analysis of the flow rate through the opening between the two interior spaces of the model. The focus is on quantifying the mass exchange between the two rooms across different configurations, based on the measured mean velocity values. The calculation of the flow rate passing through the aperture offers a concise synthesis of the application of outdoor forcing conditions for each physical model test configuration. For the calculation of the flow rate, following the scheme shown in Figure 3.1, we evaluated the individual areas of influence of the measurement points, which, in the same scheme, are indicated as dA. As noted in paragraph 3.1.1, 6 of the 42 small areas are larger than the others, and their size is equal to $dA_{tb} = 3.25$ cm^2, whereas the size of the remaining 36 ones is equal to $dA = 2.17$ cm^2. We chose to distinguish the larger area elements, denoted with the subscript 'tb' (standing for top and bottom), from the others in order to achieve greater clarity in the notation. At this point, the following formula was applied for the calculation of the flow rate:

$$Q = \sum_{m=1}^{6} d\vec{A_{tb,m}} \cdot \vec{v_m} + \sum_{n=1}^{36} d\vec{A}_n \cdot \vec{v_n} \tag{4.7}$$

where, by virtue of the application of the scalar product, only the horizontal component u of the velocity vector $\vec{v}$ is used. The results of the analysis are summarized in Table 4.1, in which we also included, as indication, the calculated flow rate expressed in terms of ACH_{RS} (Air Changes per Hour) at real scale according to the equation:

$$ACH_{RS} = \frac{Q \cdot 3.6}{V_{room}} \cdot \lambda^2, \tag{4.8}$$

where Q is the calculated flow rate in l/s, 3.6 is the conversion factor used to convert from l/s to m^3/h, V_{room} is the volume of the windward room and $\lambda = 1/15$ is the geometric scale.

The results clearly show that the volumetric flow rate attains its maximum value when all six windows are open. Furthermore, the data indicate that the upstream openings exert the predominant influence on the overall flow rate, as exemplified by the comparison between Tests 9 and 10. A more detailed analysis reveals that the specific position of the upstream opening also plays a decisive role: when the central upstream window is open, a larger airflow volume is observed, as demonstrated by the comparison between Tests 11 and 12. This effect must also be considered in conjunction with the total number of open windows, irrespective of their location. For instance, the comparison between Tests 16 and 11 highlights that, despite identical downstream configurations, the larger number of upstream openings in Test 11 likely enhances the suction effect, thereby promoting a higher overall flow rate. These findings are consistent with the trends illustrated in Figure 4.2. In particular, when considering also the pressure difference between the two rooms, it emerges that for an inclination angle of 15 degrees (Test 6) the flow rates are higher than those obtained with inclination angles of 30 degrees or 0 degrees.

4.4 Dimensionless groups involved

In the present section, attention is devoted to the two dimensionless groups upon which the investigated process primarily depends, namely the Euler number (Eu) and the Reynolds number, this latter defined with reference to the opening between the two rooms (Re_i) as stated in Chu et al. (2010). In paragraph 4.1, the dimensionless groups have already been described; it is further noted that examining them in relation to other non-dimensional quantities enables comparisons across different flow conditions, independent of scale or of the absolute values of velocity, or flow rate, and pressure.

We illustrate the two dimensionless groups explicitly denoting

$$Eu = \frac{\Delta p}{U_w^2 \rho} \tag{4.9}$$

and

$$Re_i = \frac{\bar{u} \times d_i}{\nu}, \tag{4.10}$$

where $\bar{u}$ is the horizontal mean velocity through the aperture, ν is the dynamic viscosity of air and d_i is the characteristic diameter of the aperture defined as

$$d_i = \frac{4A_d}{P_i}, \tag{4.11}$$

with A_d representing the doorway area and P_i its perimeter. In the context of the present study, the Reynolds number associated with the opening is used to characterize the flow regime occurring at that location, while Eu serves as a key indicator of how pressure differences drive the airflow through the inter-room opening.

We then proceeded to calculate Eu and Re_i for the tests reported in Table 4.1, which, as already noted, included tests with velocity and pressure gradient measurements. The results are presented in two graphs, shown in Figures 4.10 and 4.11.

Test	Configuration	U_w (m/s)	θ (°)	Q (l/s)	ACH_{RS} (1/h)	Q_{th} (l/s)	Eu
1	A: 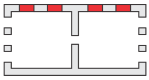	10	0	52.7	11	62.8	0.206
2	B: 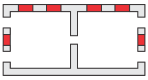	3	0	13.4	3	14.1	0.116
3	B, *as above*	5	0	21.2	5	25.6	0.137
4	B, *as above*	7.5	0	31.2	7	39.0	0.142
5	B, *as above*	10	0	41.1	9	51.8	0.141
6	B, *as above*	10	15	45.6	10	56.4	0.167
7	B, *as above*	10	30	42.3	9	53.8	0.152
8	B, *as above*	10	60	34.3	7	41.3	0.089
9	C: 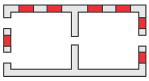	10	0	36.2	8	45.9	0.110
10	D: 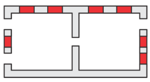	10	0	36.3	8	44.0	0.101
11	E: 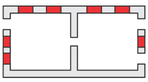	10	0	32.1	7	43.8	0.100
12	F: 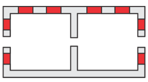	10	0	29.1	6	28.6	0.043
13	G: 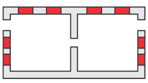	3	0	9.7	2	8.5	0.042
14	G, *as above*	5	0	15.9	3	17.9	0.067
15	G, *as above*	7.5	0	22.1	5	28.3	0.074
16	G, *as above*	10	0	28.0	6	38.9	0.079
17	H: 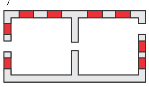	10	0	31.4	7	28.1	0.041
18	I: 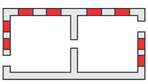	10	0	27.8	6	30.7	0.049

Table 4.1: Summary of the tests carried out and the corresponding calculated flow rate Q, together with the calculated Q_{th} and Eu. We also expressed Q in the unit of Air Changes per Hour at real scale (ACH_{RS}).

In the first graph (Figure 4.10), the flow rate, nondimensionalized with respect to the model length, $L \approx 1$ m, and the freestream wind velocity U_w, is plotted as a function of the Euler number. To the graph we added the flow rate Q_{th}, nondimensionalized in the same manner, determined by applying Bernoulli's theorem calculated between the upstream room internal model section, whose area is equal to A_l, and the contracted section at the doorway.

$$Q_{th} = \frac{1}{L^2 U_w} A_l A_d \sqrt{\frac{2\,\Delta p}{\rho\,(A_l^2 - A_d^2)}} \tag{4.12}$$

Strictly speaking, the pressure difference to be used should be that between the pressure in the upstream room and that at the cross-section of the opening. However, as reported in Chu et al. (2010), many studies have instead employed the pressure difference between the two rooms because it is easier to measure, which has likewise been adopted in the present study. The experimental points of Q and Q_{th} were interpolated using two power law functions in the form $y = ax^b$.

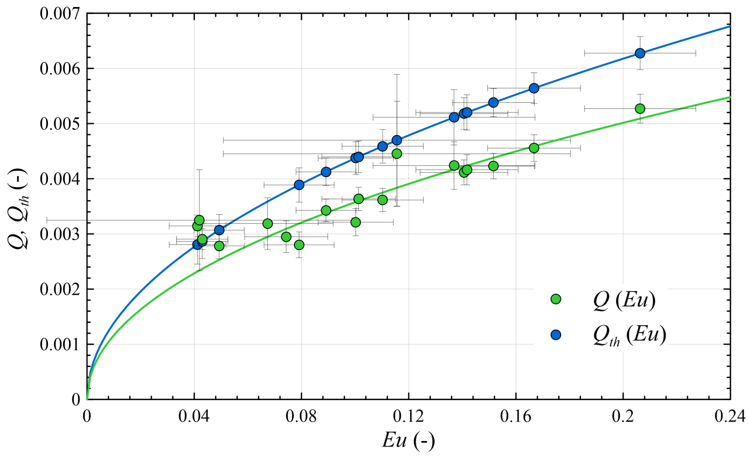

Figure 4.10: Non-dimensional flow rate, Q, through the door as a function of the Euler number, Eu, along with the theoretical points obtained by applying Bernoulli's theorem. Two fits using a power law function are also shown.

The theoretical flow rate Q_{th}, as illustrated in Figure 4.10, exhibits a square-root-type dependence on the Euler number, $Q_{th} \propto Eu^{0.5}$, and therefore on its defining component pressure gradient Δp. The fitting resulted in the following equation:

$$Q_{th} = 0.014\; Eu^{0.5}. \tag{4.13}$$

Similarly, fitting the points of Q as a function of Euler resulted in the following equation:

$$Q = 0.009\ Eu^{0.389}. \tag{4.14}$$

The experimental b exponent being lower than the theoretical one indicates that the flow rate increases with Eu number more slowly than predicted. This behaviour can be physically interpreted as the result of several non-ideal effects. Frictional losses along the walls and at the doorway, turbulence induced by varying boundary conditions (due to different window configurations), and viscous dissipation all contribute to reducing the effective driving pressure across the door.

Moreover, the experimental coefficient a being smaller than the theoretical one reflects that the absolute flow rate is reduced relative to the ideal prediction. Factors such as recirculation zones near the doorway, imperfect alignment of openings, and slight pressure losses due to the physical model's geometry all contribute to this reduction.

Subsequently, the analysis shifted towards the investigation of the behaviour of the so-called internal discharge coefficient C_{zi}, as defined in Chu et al. (2010). The two graphs in Figures 4.11 and 4.12, along with the corresponding numerical values presented in Table 4.2, illustrate the behaviour of C_{zi} as a function of the Reynolds number Re_i, defined in 4.10, reflecting different flow regimes.

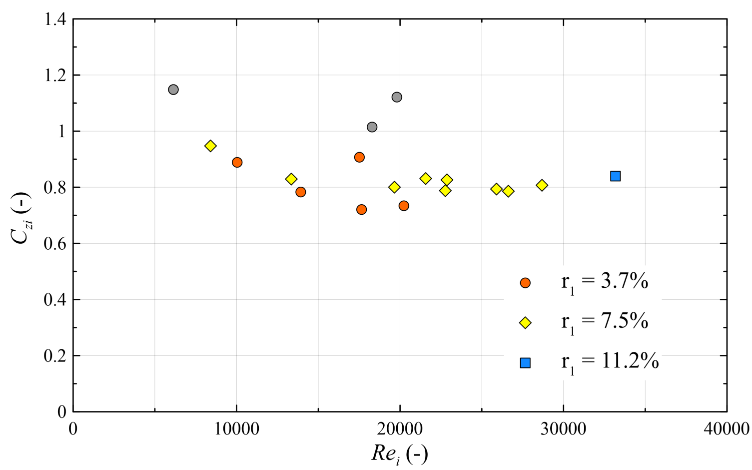

Figure 4.11: Discharge coefficient, C_{zi}, as a function of the Reynolds number, Re_i, with varying upstream wall porosity r_1. We have indicated in grey the points characterized by a $C_{zi} > 1$.

Test	Configuration	U_w (m/s)	θ (°)	r_1	r_2	Re_i ($\times 10^3$)	C_{zi}
1	A: 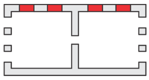	10	0	11.2	11.2	33.18	0.840
2	B: 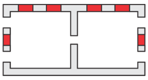	3	0	7.5	7.5	8.410	0.948
3	B, *as above*	5	0	7.5	7.5	13.34	0.829
4	B, *as above*	7.5	0	7.5	7.5	19.66	0.800
5	B, *as above*	10	0	7.5	7.5	25.91	0.794
6	B, *as above*	10	15	7.5	7.5	28.68	0.807
7	B, *as above*	10	30	7.5	7.5	26.62	0.786
8	B, *as above*	10	60	7.5	7.5	21.57	0.831
9	C: 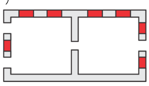	10	0	7.5	3.7	22.76	0.788
10	D: 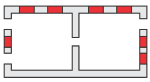	10	0	7.5	3.7	22.88	0.826
11	E: 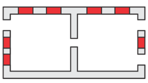	10	0	3.7	7.5	20.22	0.734
12	F: 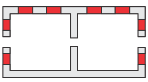	10	0	3.7	3.7	18.29	1.014
13	G: 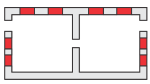	3	0	3.7	3.7	6.134	1.148
14	G, *as above*	5	0	3.7	3.7	10.04	0.889
15	G, *as above*	7.5	0	3.7	3.7	13.93	0.783
16	G, *as above*	10	0	3.7	3.7	17.65	0.721
17	H: 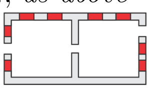	10	0	3.7	3.7	19.80	1.121
18	I: 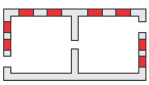	10	0	3.7	3.7	17.52	0.907

Table 4.2: Summary of the tests carried out and the corresponding values of r_1, r_2, Re_i and C_{zi}.

The definition of C_{zi} is the following:

$$C_{zi} = \frac{Q}{A_d}\sqrt{\frac{\rho(1-r_i^2)}{2\Delta p}}, \tag{4.15}$$

where

$$r_i = \frac{A_d}{A_l} \tag{4.16}$$

defines the dividing wall's porosity, with A_l equal to the whole area of the dividing wall between the two rooms, which is also the area of the lateral section of the model's room, in our case equal to 0.15 m^2. The discharge coefficient is essentially a measure of how far the real flow departs from the ideal Bernoulli-based prediction, incorporating the effects of geometry, Reynolds number, and other prevailing flow conditions. In the present study, unlike Chu et al. (2010), the porosity of the dividing wall was kept constant to $r_i = 6.5\%$ for all tests. The freestream wind velocities within the tunnel were varied for certain configurations, as was the angle of incidence (see Table 4.2). It is also possible to define a porosity relative to the windward (upstream) external wall as follows:

$$r_1 = \frac{n_1 A_w}{A_l}, \tag{4.17}$$

where the subscript "1" refers to the windward wall, n_1 is the number of open windows in the windward wall of the model and A_w is again the area of a single window, equal to 56 cm^2. Similarly, it is possible to define a porosity for the leeward wall:

$$r_2 = \frac{n_2 A_w}{A_l}, \tag{4.18}$$

where the subscript "2" refers to the leeward wall and n_2 is the number of open windows in the leeward wall of the model.

To enable a more detailed interpretation of the graph in Figure 4.11, the $C_{zi}(Re_i)$ data points were distinguished according to the porosity of the windward wall r_1, which is 3.7% in the case of one open window, 7.5% for two open windows and 11.2% for three open windows (the latter corresponding to test 1). This value, however, does not account for the position of the open window(s), which could affect the results, although, according to Chu et al. (2010), the internal discharge coefficient is generally independent of the Reynolds number. It can be observed that there is a general tendency for the value of C_{zi} to remain relatively constant and to settle around approximately

0.8, with better agreement for the tests with $r_1 = 7.5\%$ and $r_1 = 11.2\%$. In the graphs of Figures 4.11 and 4.12, the points shown in grey correspond to Czi values greater than 1, which is considered anomalous given the physical meaning of Czi explained above. These anomalies, as also reported inChu et al. (2010), are due to the approximation involved in applying Bernoulli's theorem between the upstream room section and the doorway section, while the associated pressure measurement was actually taken in the downstream room. In our case, this anomaly can be observed not only for low values of porosity (r_1), but also due to the internal turbulence, which generates complex flow patterns that affect the pressure values measured at the two static taps.

We reproduced the graph from Figure 4.11 in Figure 4.12, changing the legend to focus on different aspects, this time related to U_w. Focusing on the C_{zi} values obtained with $U_w = 10$ m/s, i.e. the freestream wind velocity that most closely approaches the value of 17.5 m/s used by Chu et al. (2010), we observe that the first five points, with $15 \times 10^3 < Re_i < 21 \times 10^3$, show the greatest deviation from the asymptotic trend. They are characterized by a value of $r_1 = 3.7\%$ and, for the first four points, also of $r_2 = 7.5\%$. This highlights that at low porosity levels of both the windward and leeward walls, C_{zi} exhibits greater variability, and it is in this circumstance that the configuration of the open windows plays a significant role in determining the discharge coefficient.

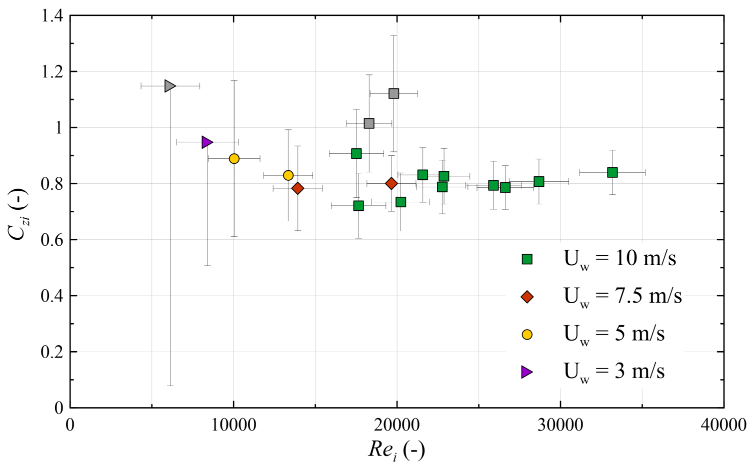

Figure 4.12: Discharge coefficient, C_{zi}, as a function of the Reynolds number, Re_i. We have indicated in grey the points characterized by a $C_{zi} > 1$.

Finally, from a further analysis of Table 1, we observe that the wind's angle of attack does not affect the variability of C_{zi}.

A further step was taken by calculating the propagated errors on the experimental data, included as error bars in Figures 4.10 and 4.12, with the details of the calculation presented in the following section 4.4.1. In light of these large errors, the C_{zi} values for $U_w = 3$ m/s can be considered unreliable. To avoid cluttering the graph, only the lower vertical error bar was reported. This significant error arises from the pressure measurements, which, at low freestream velocities — and consequently low pressure gradients — were more strongly affected by the instrumental error of 0.25 Pa.

4.4.1 Considerations on measurements errors

In this paragraph, the methodologies used to calculate the errors of the experimental measurements will be illustrated. These errors are displayed in the graphs in Figures 4.10 and 4.12 by means of error bars. Assuming that gross errors were negligible, we focused on quantifying the different types of measurement uncertainty: systematic errors, arising from the calibration of the instruments; instrumental errors, corresponding to the precision limits reported in the instruments' datasheets; and random errors, due to the variability of the instantaneous measurements around the time-averaged values. The error evaluated on the measured data was then propagated to obtain the total errors on Q_{th}, Q, Eu, Re_i and C_{zi}.

The error in the measured velocities was calculated by combining a 2% uncertainty from the instrument datasheet with a calibration error, derived from the confidence intervals of the hot-wire calibration curves: 0.25 m/s for mean velocities below 2 m/s, and 0.1 m/s for velocities above 2 m/s. Standard deviation was not considered, in order to prevent the large fluctuations caused by turbulence from inflating the estimated random error. The total error on the mean velocity was then also weighted according to the areas of influence of each point; see Figure 3.1.

The calculation of the error in the pressure measurement was based on the work of Zięba (2010). The study starts from the assumption that, when measured data are autocorrelated, the usual formulas for estimating the variance and the variance of the mean are no longer adequate. In our case, the pressure measurements are autocorrelated due to turbulence, and therefore the calculation of statistical parameters must take into account an effective number of samples n_{eff} that is smaller than the total number n of samples actually recorded by the instrument.

The effective number of samples is given by the following formula:

$$n_{eff} = \frac{n}{1 + 2\sum_{k=1}^{n-1} \frac{n-k}{n}\rho_k}, \tag{4.19}$$

where ρ_k is the autocorrelation function at lag k. Our time series of pressure measurements can be effectively modelled using a first-order autoregressive process, AR(1), given the very high values close to 1 observed in the lag-1 autocorrelation function (ρ_1) indicating a strong dependence of any value on its preceding one. Having established the AR(1) model, we can proceed to simplify formula 4.21 by rewriting the second term of the denominator as follows, taking into account that for first-order autoregressive model $\rho_k = a^k$, with $a = \rho_1$:

$$\sum_{k=1}^{n-1} \left(\frac{n-k}{n}\right) a^k \approx \sum_{k=1}^{\infty} a^k = \frac{a}{1-a}. \tag{4.20}$$

Equation 4.20 was obtained by considering the number of samples tending to infinity with respect to k, which in our case is equal to 1, and by applying the convergence rules of an infinite geometric series, taking into account that $a < 1$.

Equation 4.21 now becomes:

$$n_{eff} = n\frac{1-a}{1+a}. \tag{4.21}$$

The formula for the calculation of n_{eff} for the case of an AR(1) model allowed us to streamline the computations and to proceed with the evaluation of the standard uncertainty of the mean of the measurements (u_{rand}) using formula 4.22:

$$u_{rand} = \frac{\sigma}{\sqrt{n_{eff}}}, \tag{4.22}$$

where σ is the standard deviation of the population.

Subsequently, for the calculation of the random error, we referred to a 95% confidence interval, while for the calculation of the final total error, we added to the aforementioned random error an instrumental error declared in the datasheet of the pressure transducer equal to 0.25 Pa.

Finally, for the calculation of errors in the length measurements, only an instrumental error of 0.5 mm was considered.

Chapter 5

Results for water tank activities

5.1 Velocity field

In this section, the results obtained from the experimental campaign concerning human movement in indoor environments are presented. More specifically, two experimental campaigns were conducted: the first employed the UDP probe measurement technique, described in Section 2.2.2, which allows for the acquisition of velocity values of the fluid disturbed by the motion of the human model along a vertical line; the second made use of the PIV techniques on three measurement planes, as previously described in Section 2.2.3,which allows the measurement of the two-dimensional velocity field on a plane. The aim of this chapter is to investigate the fluid exchange between two environments caused by the passage of a human being, analyzing it from two very different experimental perspectives: the UDP technique, which is more invasive but based on direct velocity measurements obtained through ultrasonic probes, and the PIV technique, which relies on image-based analysis performed after appropriate calibration procedures. The expected outcome is to achieve comparability between the results obtained from the two approaches.

The analysis begins with the data acquired using UDP measurement techniques. The data recorded by the two probes, after undergoing the necessary processing steps described in Section 3 to obtain the velocity components along the measurement vertical in the Cartesian reference frame (x–z), were represented in panels structured as follows: the abscissa axis reports time in seconds, t (s), while the ordinate axis corresponds to the vertical coordinate z. Thus, as time t varies, the quantity under consideration is displayed along the measurement vertical at the different acquisition points, i.e., at the probe's gate positions (see Section 3.2.1). The resulting output is therefore a temporal contour plot (time map), illustrating the evolution of the measured quantity along the vertical as a function of time. In all time maps obtained from the UDP probe measurements, the origin of both the time axis and the mannequin's x-coordinate was set to the instant when the mannequin crossed the opening between the two model environments. This convention ensured that all test repetitions were referenced to the same space–time coordinate, thus simplifying the computation of averages.

In Figure 5.1, two contour plots are presented, produced using the methodology described above, illustrating the temporal evolution of the mean horizontal velocity $\bar{u}$. In both panels, the starting and ending moments of the mannequin's motion are indicated, and, from the comparison between the two panels, two different behaviours of the fluid subjected to the passage of the dummy emerge. Panel (a) in figure 5.1 shows Test 1 (the numbering refers to Table 3.3), in which the dummy's velocity was 0.16 m/s, whereas Figure (b) shows Test 4, in which the its velocity was 1.13 m/s.

We can observe that for the lowest sliding speed of the mannequin, the fluid is only slightly disturbed by its passage. The region of the plot affected by the mannequin's movement exhibits very low average horizontal velocities, exceeding 0.1 m/s only when the mannequin is in areas closest to the doorway. Moreover, the velocities are predominantly positive during the mannequin's motion, with the exception of a slight reverse flow occurring between $t = 0.5$ s and $t = 1$ s at heights z between 50 mm and 70 mm. It is important to note that the portion of the plots between $z = 0$ mm and approximately $z = 10$ mm contains somewhat unreliable data, as this area was occupied by a perforated rail, which may have induced minor, non-representative local flow disturbances.

That reverse flow, which in panel (a) appeared at an embryonic stage and was barely noticeable in the data, becomes much more evident in panel (b) of figure 5.1, which shows the contour plot of the mean horizontal velocity $\bar{u}$ for the case with $U_m = 1.13$ m/s. Four distinct phases can be identified in Test 4. In the first phase, the ambient fluid is at rest, with mean velocities close to zero. Upon the pedestrian's departure, a second phase begins, during which the pumping effect caused by the pedestrian passing through the doorway becomes evident, reaching peak positive velocities and producing a rapid inflow of water into the receiving room. To balance this strong positive transfer, a counterflow develops in the opposite direction, with the fluid in the receiving environment moving back through the opening against the direction of the pedestrian's motion. Finally, once the pedestrian has completely passed, the system seeks a new equilibrium. Since the opening between the two spaces remains unobstructed after the passage, a fourth phase of oscillations occurs, in which the fluid alternates in direction with a periodicity of approximately 0.5 s, and mean velocities remain close to zero. This final phase is particularly critical for our experimental setup, as the preliminary tests did not include any constraints at the upper boundary, leading to noticeable oscillations of the free surface. It is for this reason that two polystyrene panels were installed to dampen the motion, significantly reducing the oscillations, although they did not disappear completely. For the subsequent tests with PIV, a ceiling (leed) was added to the arrival chamber, which almost completely eliminated this issue. We also observe that in the velocity maps obtained from the UDP measurements, there are white areas. These regions, where data are missing, are due to the fact that when the dummy passes through the measurement cones of the probes, shadowed zones are created, preventing the instrument from measuring the velocity data in certain gates.

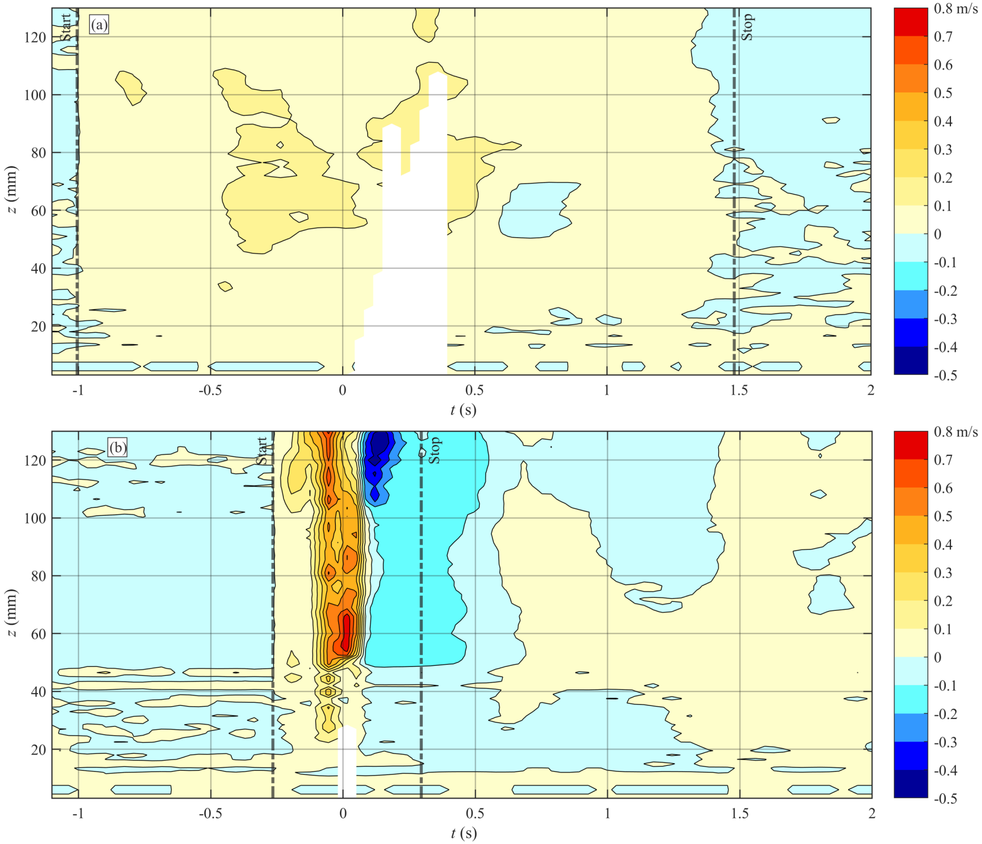

Figure 5.1: (a) Velocity map showing the contour plot of the mean horizontal velocity $\bar{u}$ in m/s measured by the UVP probes as a function of time t in seconds for test 1 with $U_m = 0.16$ m/s, (b) Velocity map showing the contour plot of the mean horizontal velocity $\bar{u}$ in m/s measured by the UVP probes as a function of time t in seconds for test 4 with $U_m = 1.13$ m/s. Test numbering according to Table 3.3.

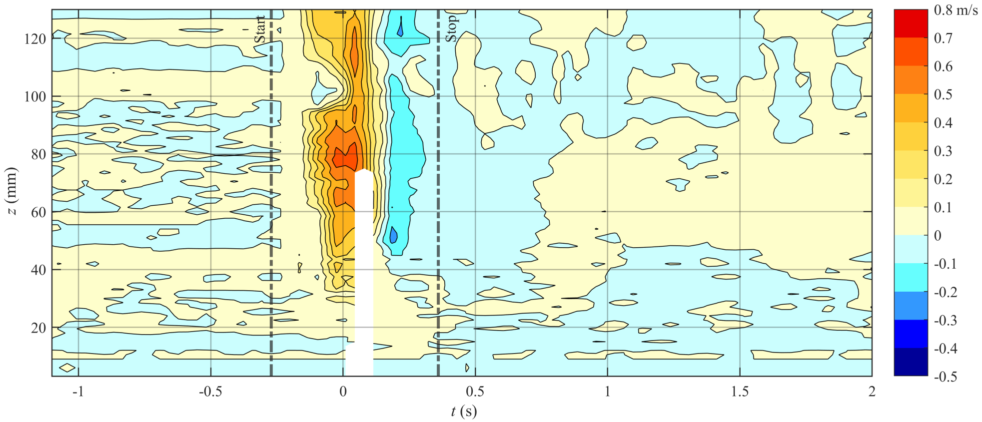

Figure 5.2: Velocity map showing the contour plot of the mean horizontal velocity $\bar{u}$ in m/s measured by the UVP probes as a function of time t in seconds for test 3a with $U_m = 0.79$ m/s. Test numbering according to Table 3.3.

The presence of reverse flow is also confirmed at lower pedestrian velocities, such as 0.79 m/s. In fact, the plot in Figure 5.2 shows that the mean horizontal velocity measured by the UDP profilometers exhibits a behavior similar to the case with $U_m = 1.13$ m/s, although with lower velocity magnitudes.

A simultaneous analysis of the data obtained using PIV techniques allows us to validate the measurements obtained with the Doppler profilometers. The coordinate system used for the PIV acquisition results was aligned with that employed for the UDP measurements. Specifically, the z coordinate is identical in both cases, and the x coordinate is likewise zero at the midline of the opening. The gray regions in the plots indicate areas where data acquisition was not possible because of the apparatus geometry; in these zones, the tank walls obstructed the camera's line of sight, preventing them from being captured within its field of view.

Figure 5.3 shows a pair of contour plots of the mean horizontal velocity $\bar{u}$ in m/s obtained from Tests 6 and 8, conducted using the PIV technique (the numbering of the PIV tests refers to Table 12). The plots correspond to two tests in which the mannequin moved along the rail at the same velocity U_m; however, in plot (a) the acquisition plane was vertical and parallel to the mannequin's motion, at $y = 0.6$ cm, whereas in plot (b) the plane was horizontal, located at $z = 9$ cm. Although the two tests were performed at different times, it can be observed that our experimental configuration ensured good reproducibility at the instant $t = 0.25$ s, which was captured in both cases. In this case, the instant $t = 0$ corresponds to the beginning of the test when the mannequin starts moving.

Complementing Figure 5.3, Figure 5.4 presents another pair of contour plots of the mean horizontal velocity, this time for $U_m = 0.86$ m/s, captured at $t = 0.19$ s. In this case, higher mannequin velocities result in greater magnitudes of the fluid's mean horizontal velocity. However, the flow regions remain comparable, consisting of a region of positive mean velocity in front of the mannequin (more extended in the plots of Figure 5.4), a region of negative velocity above the mannequin's head, and a turbulent wake region behind the mannequin.

The comparison with the final instants of the same tests (shown in Figures 5.5 e 5.6) allows us to confirm the previously identified flow regions, while also highlighting two phenomena more clearly. The first is the wake effect caused by the mannequin's motion, which appears much more pronounced and exhibits a different structure between the two tests. In fact, the plots in Figure 3 show that with $U_m = 0.86$ m/s, the wake flow field is highly chaotic and turbulent, making entrainment effects more significant.

In contrast, for $U_m = 0.58$ m/s, the mean horizontal velocity $\bar{u}$ is locally higher in some regions; however, this is due to reduced turbulent activity, resulting in much more modest entrainment effects. Further analyses on the characterization of turbulence will allow us to clarify this feature of the wake flow. The other phenomenon, related to the area of greatest interest in the physical modeling—namely, the region near the opening between the two rooms—is the partitioning of the opening's cross-section into a zone dominated by reverse flow and a zone characterized by predominantly positive mean horizontal velocities and higher turbulent activity.

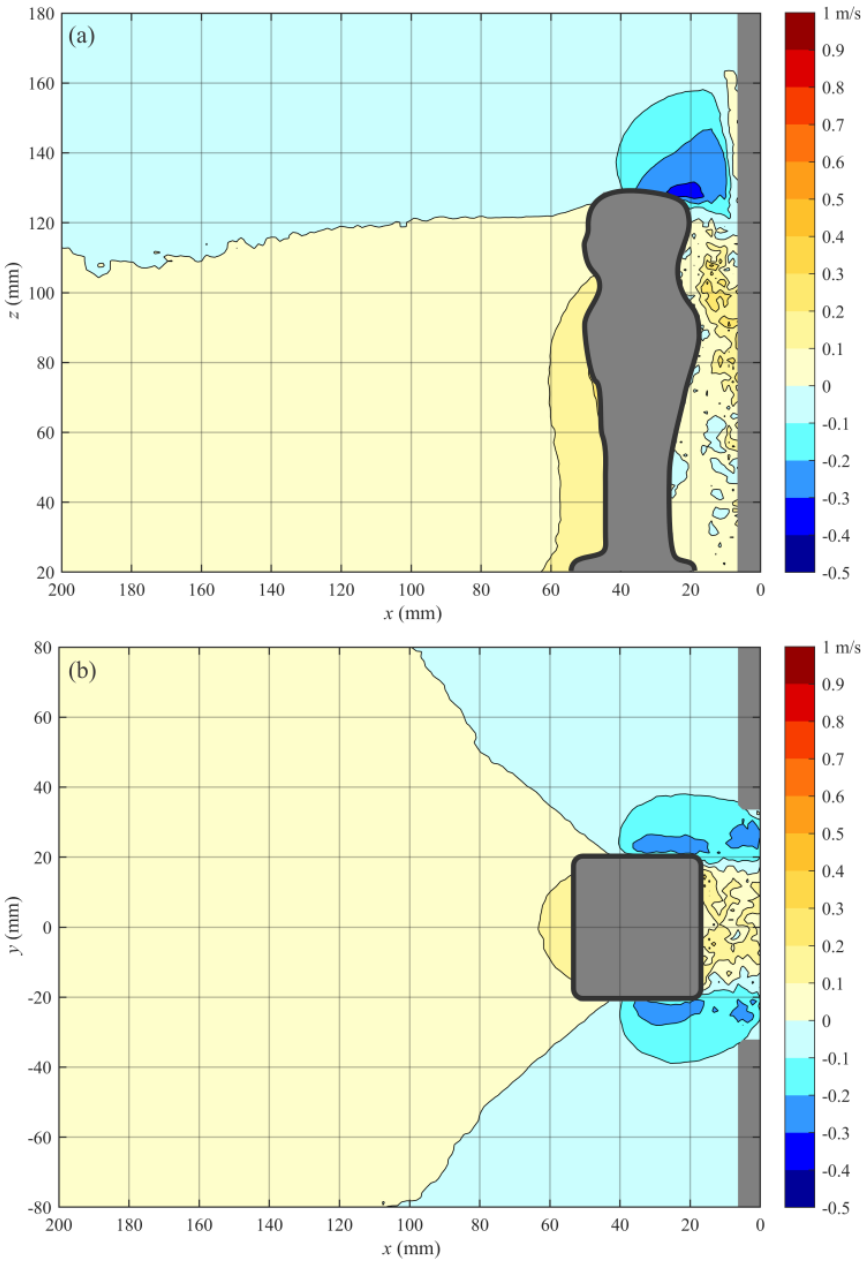

Figure 5.3: Contour plot showing the mean horizontal velocity $\bar{u}$ (in m/s) for Test 6 (panel a) and 8 (panel b) with $U_m = 0.58$ m/s at time $t = 0.25$ s. The axes refer to the coordinate system presented in Figure 2.7. Test numbering according to Table 3.4. Panel (a) refers to plane $y = 0.6$ cm while panel (b) refers to plane $z = 9$ cm.

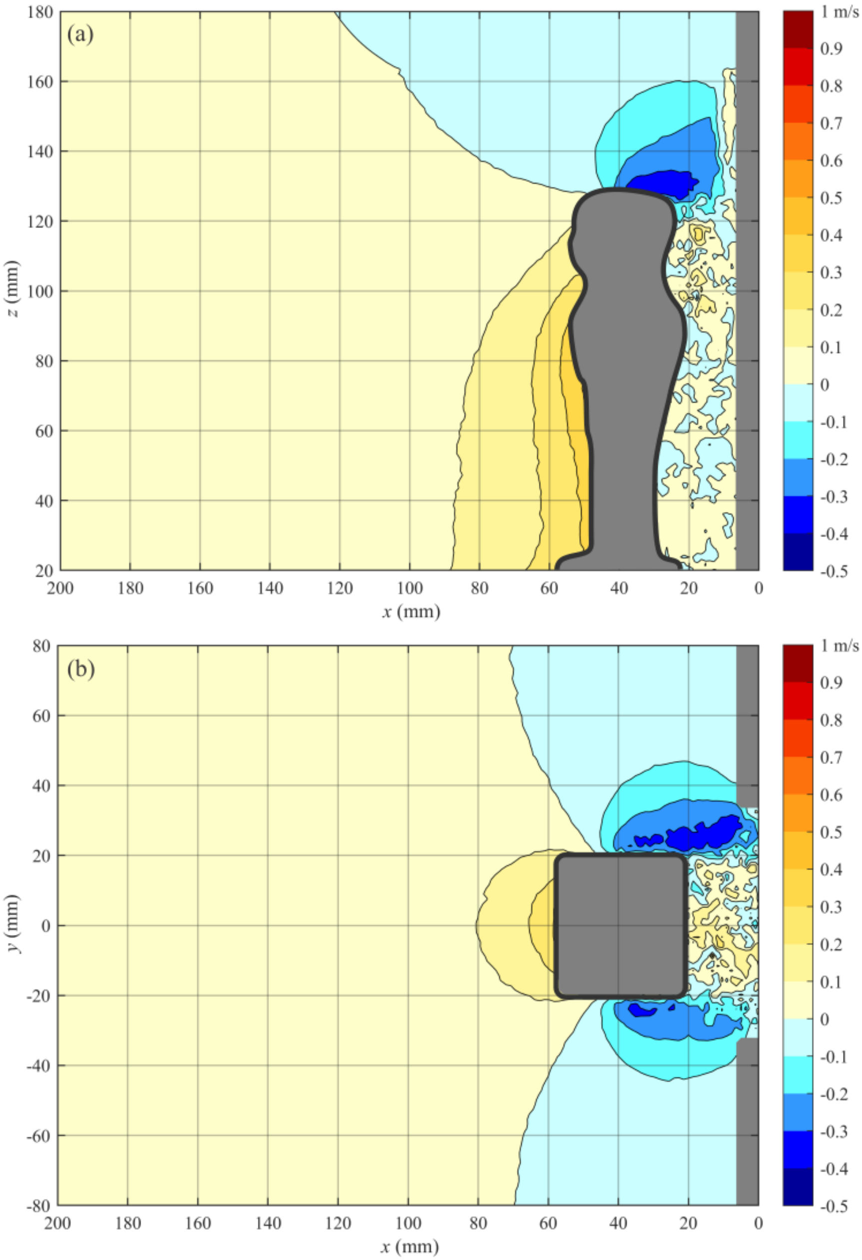

Figure 5.4: Contour plot showing the mean horizontal velocity $\bar{u}$ (in m/s) for Test 12 (panel a) and 14 (panel b) with $U_m = 0.86$ m/s at time $t = 0.19$ s. The axes refer to the coordinate system presented in Figure 2.7. Test numbering according to Table 3.4. Panel (a) refers to plane $y = 0.6$ cm while panel (b) refers to plane $z = 9$ cm.

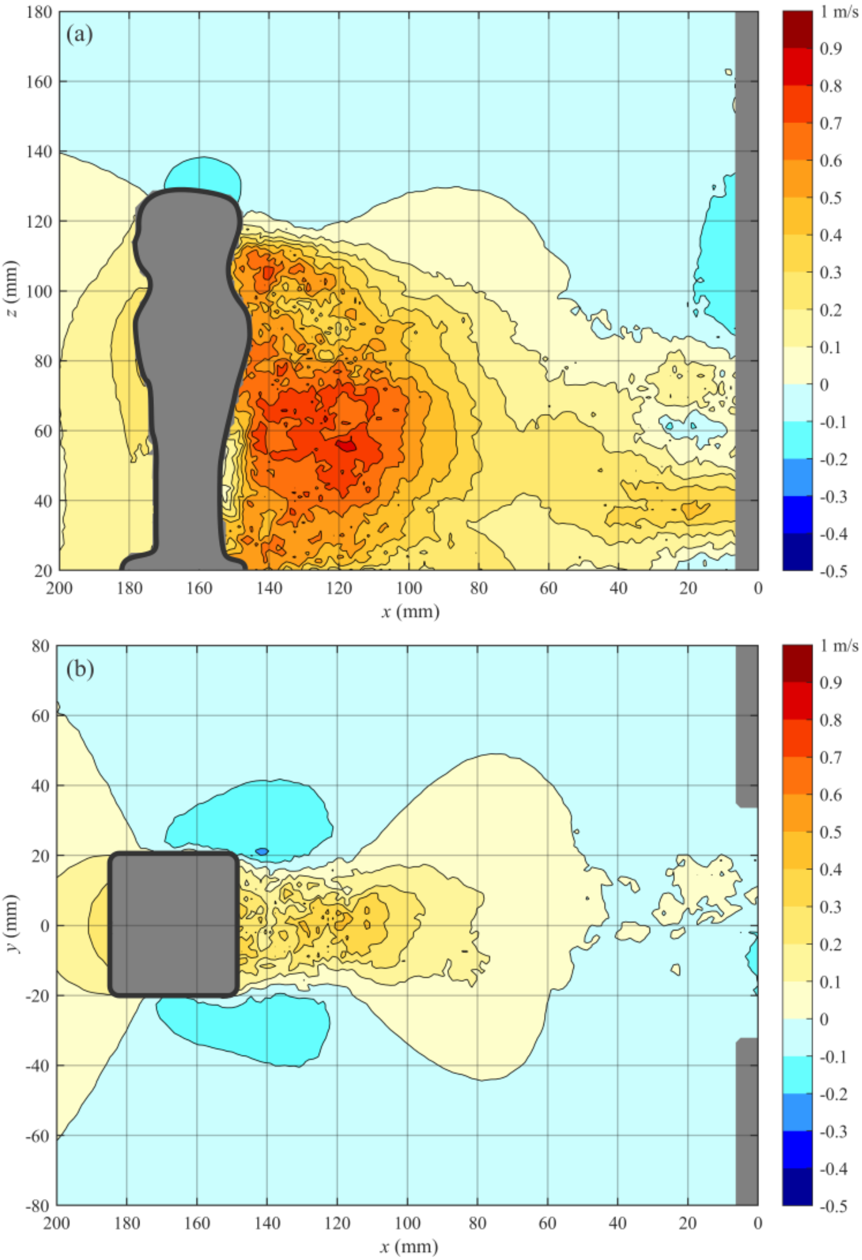

Figure 5.5: Contour plot showing the mean horizontal velocity $\bar{u}$ (in m/s) for Test 6 (panel a) and 8 (panel b) with $U_m = 0.58$ m/s at time $t = 0.37$ s. The axes refer to the coordinate system presented in Figure 2.7. Test numbering according to Table 3.4. Panel (a) refers to plane $y = 0.6$ cm while panel (b) refers to plane $z = 9$ cm.

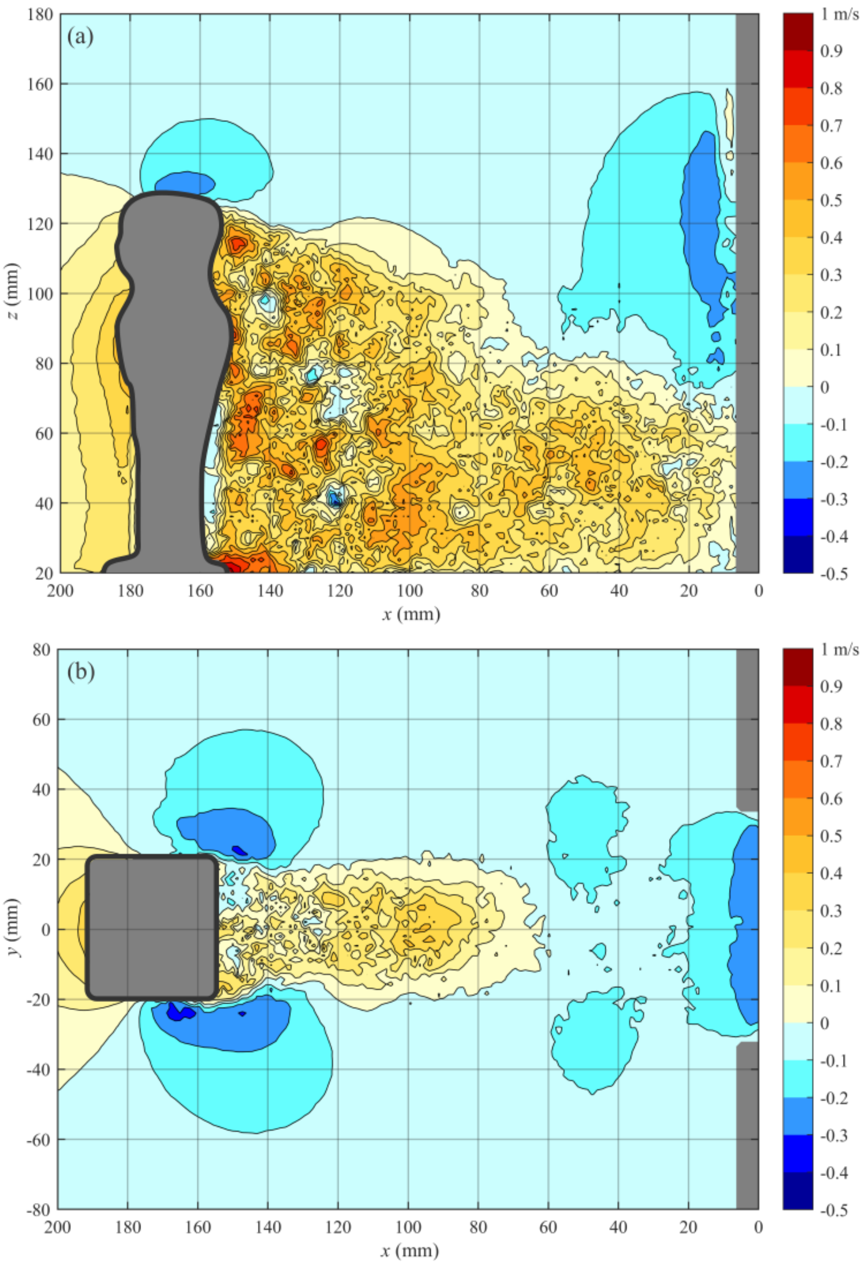

Figure 5.6: Contour plot showing the mean horizontal velocity $\bar{u}$ (in m/s) for Test 12 (panel a) and 14 (panel b) with $U_m = 0.86$ m/s at time $t = 0.27$ s. The axes refer to the coordinate system presented in Figure 2.7. Test numbering according to Table 3.4. Panel (a) refers to plane $y = 0.6$ cm while panel (b) refers to plane $z = 9$ cm.

5.1.1 Imposed pressure gradient with recirculation

In this paragraph, the results obtained for tests number 15, 16, 17, 18, 19 and 20 (the numbering refers to Table 3.4) will be analyzed. These tests were carried out using the experimental configuration shown in Figure 2.11 in the presence of a recirculation flow from the arrival room toward the departure room of the mannequin's movement, that is, with an overpressure imposed in the arrival room of the mannequin. These tests were compared with test number 12, which has the same characteristics in terms of the mannequin's speed but was carried out in the absence of overpressure or recirculating flow.

In all tests with imposed pressure gradient, the acquisition plane was vertical and coincident with the plane $y = 0.6$ cm, according to the reference system shown in Figure 2.9. This plane was selected because it was the first available position as close as possible to the mid-width of the opening that still prevented the laser sheet from intersecting the rail. As previously noted, the rail was made of stainless steel, and laser refraction on its surface would have produced undesirable effects that could have compromised the quality of the measurements. Therefore, given the rail width of 1.2 cm, the plane was positioned flush with one of its edges.

The acquired data made it possible to calculate the flow rate Q passing through the opening between the two environments. This calculation is an approximation, as the horizontal velocity measured with PIV techniques at the opening (i.e., for heights z between 0 and 15 cm) was obtained by averaging the horizontal velocity values measured at identical heights over a window located at the far right of the frame, i.e. corresponding to the opening section, 0.5 cm wide and extending, as previously mentioned, up to $z = 15$ cm.

Subsequently, the velocity values thus obtained along the vertical coordinate were multiplied by the corresponding area of the opening at each point, that is, a rectangular area with its center at the height where the average horizontal velocity was calculated, a height equal to the distance between two adjacent points, and a base of 6.5 cm, corresponding to the width of the opening.

The sign convention for the flow rates refers to the reference system adopted throughout the analysis (Figure 2.9). A negative flow rate Q therefore corresponds to a flow (and thus a volume) leaving the arrival room of the mannequin, whereas a positive Q corresponds to a flow (or volume) entering the arrival room.

Figure 5.7 shows the temporal evolution of the flow rate Q through the opening between the two rooms for a constant dummy velocity $U_m = 0.86$ m/s and for the different recirculating flow rates tested. The figure reports only the time interval preceding the entry of the dummy into the room (at $t = 0$), corresponding to the phase during which the displaced air begins to interact with the opening. It was decided to consider, for these tests with recirculating flow rate, only the time instants preceding the entry of the mannequin into the receiving room, since the strong oscillations in the flow rate measured with the PIV equipment after the mannequin entered the room resulted in highly uncertain data. Furthermore, the time instants corresponding to the passage of the mannequin through the opening were characterized by a lack of measured data in the region of interest closest to the opening. At the beginning of its movement, the dummy injects volume into the arrival room in an increasingly greater amount until it passes through the opening, which, as customary in the present analysis, corresponds to time $t = 0$, where a peak in the introduced fluid volume occurs. This is verified for all tests except Test 12, in which the beginning of a decrease can already be observed; however, this falls within the experimental variability.

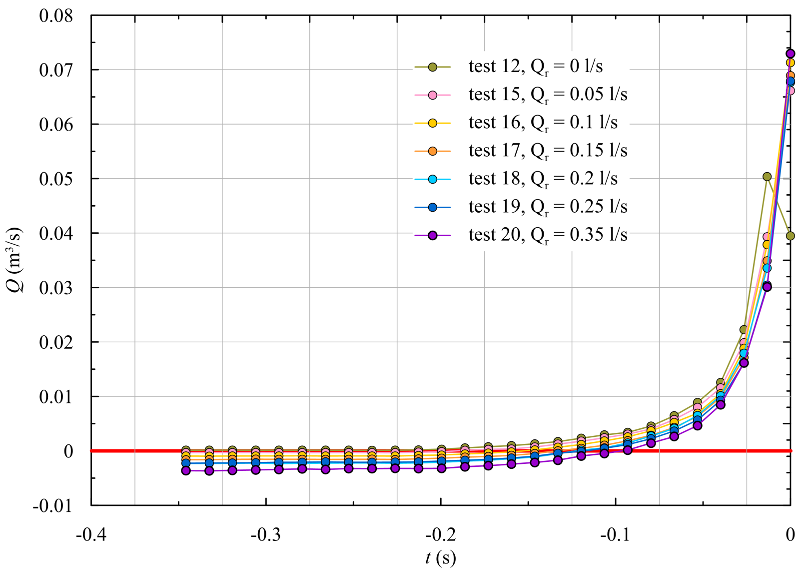

Figure 5.7: Flow rate Q in m^3/s trend at the opening between the two environments as a function of time t in s, shown for $t < 0$ As customary, $t = 0$ corresponds to the instant at which the mannequin passes through the opening.

To evaluate how the recirculating flow—and the resulting overpressure generated in the dummy's arrival room—mitigates air exchange between the two environments for $t < 0$, a volume balance was carried out by piecewise linearly integrating the flow rate over time curves shown in Figure 5.7. The practical interest is indeed in limiting air exchange between the two spaces and, more specifically, in minimizing the volume of air introduced into the arrival room during the dummy's passage. The results are summarized in the graph of Figure5.8, which shows the trend of the incoming volume into the room V_{in} as a function of the applied recirculating flow rate. Using the similarity criteria, the measured values were scaled to full scale by multiplying the calculated values by λ^{-3}, where λ is the geometrical scale equal to 1/15, as our model was at a 1:15 scale (see paragraph 2.2.7 for details).

To interpret the data, a fitting obtained from a simplified model presented below was used. The two rooms connected by an open standard doorway from which the dummy starts and arrives were considered as A and B. When a person walks from room A to room B at sustained speed, this motion induces a transient airflow across the doorway plane. This flow transports a finite volume of air from A to B, which may be relevant in the context of contaminant transfer or ventilation control.

Let $Q_h(t)$ denote the instantaneous volumetric flow rate induced by the moving person across the doorway, directed from A to B, and let τ be the effective duration of this transient event (including passage and near-wake effects). Suppose that a steady counterflow Q_r is imposed in the opposite direction (from B to A), for instance by means of mechanical ventilation.

The instantaneous net flow rate in the A $\rightarrow$ B direction is then

$$Q_{\text{net}}(t) = Q_h(t) - Q_r.$$

Only the time intervals for which $Q_{\text{net}}(t) > 0$ contribute to net transfer from A to B. The total volume of air from room A entering room B during a single crossing can therefore be written as

$$V_{A\to B}(Q_r) = \int_0^{\tau} \max\big(Q_h(t) - Q_r,\, 0\big)\, dt.$$

This expression highlights a simple physical mechanism: the imposed counterflow subtracts from the human-induced transient, and transfer occurs only when the latter locally exceeds the former.

For engineering purposes, $Q_h(t)$ can be approximated by a simple pulse. If the induced flow is modeled as approximately constant, $Q_h(t) \approx Q_h$ for

$0 < t < \tau$, the transferred volume becomes

$$V_{A\to B}(Q_r) = \max\big((Q_h - Q_r)\tau,\, 0\big).$$

Defining $V_0 = Q_h\tau$ as the transferred volume in the absence of counterflow, this reduces to

$$V_{A\to B}(Q_r) = V_0 \max\left(1 - \frac{Q_r}{Q_h},\, 0\right),$$

which predicts a linear decrease of transferred volume with increasing counterflow, vanishing at $Q_r = Q_h$.

A more realistic representation assumes that the induced flow increases and then decreases during the passage, which can be approximated by a triangular pulse of peak value Q_{pk} and duration τ. In this case, the no-counterflow volume is $V_0 = \frac{1}{2}Q_{pk}\tau$, and the transferred volume becomes

$$V_{A\to B}(Q_r) = \begin{cases} V_0\left(1 - \dfrac{Q_r}{Q_{pk}}\right)^2, & Q_r < Q_{pk}, \\ 0, & Q_r \geq Q_{pk}. \end{cases}$$

The reduction is now quadratic rather than linear, implying that even moderate counterflow can significantly suppress transfer.

Both limiting cases can be summarized in a compact parametric form,

$$V_{A\to B}(Q_r) = V_0 \max\left(1 - \frac{Q_r}{Q_*},\, 0\right)^n,$$

where Q_* is a characteristic human-induced flow scale (typically of the order of the peak value) and the exponent n depends on the pulse shape, with $n = 1$ corresponding to a rectangular approximation and $n = 2$ to a triangular one.

A simple scaling estimate for the peak human-induced flow is

$$Q_{pk} \approx C\, A_p\, U_m,$$

where A_p is the projected frontal area of the person, U_m is the walking speed, and C is a dimensionless coefficient accounting for bypass flow and non-ideal effects. If the doorway has area A_d, the imposed counterflow corresponds to an average doorway velocity $U = Q_r/A_d$. In practice, the reduction in transferred volume is primarily governed by the ratio Q_r/Q_{pk}.

Within the limits of this simplified one-dimensional description, net transfer from A to B is fully suppressed when the imposed counterflow equals or exceeds the characteristic peak human-induced flow. Although idealized, this framework provides a compact and physically transparent basis for estimating inter-room air exchange driven by occupant motion and its mitigation by controlled ventilation.

In our case, $V_0 = 0.17$ m^3/s, i.e. the volume at real scale calculated for $Q_r = 0$, and $Q_{pk} = 0.85$ l/s. The result of the fitting is shown in Figure 5.8.

Moreover, we added in Figure 5.8 a grey band that represents the total, i.e. also considering the wake transport, inlet-volume V_{in} datum obtained for the case of zero recirculation flow rate. This band is defined with reference to the sliding-door cases reported in the work by Kalliomäki and Koskela (2016), according to which the normalized air volume exchange falls within the range of 0.25 to 0.36 m^3.

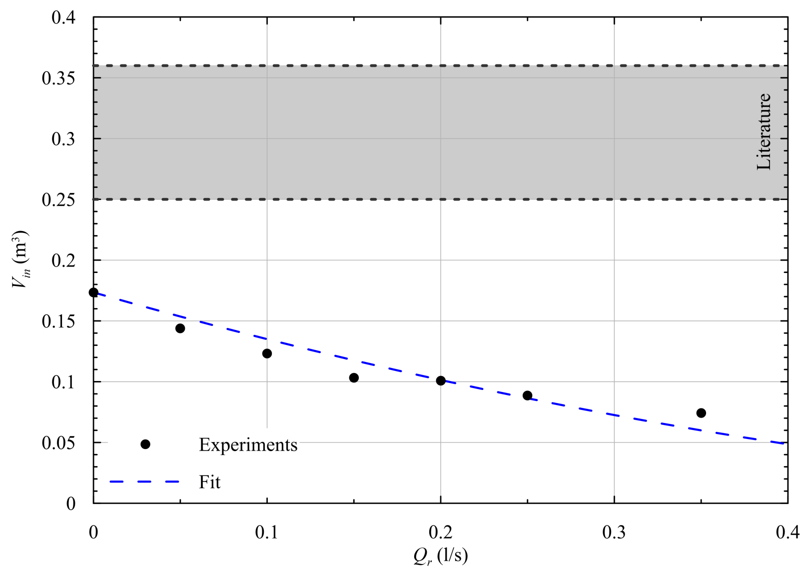

Figure 5.8: Incoming volume V_{in} into the arrival room transported by the dummy before its passage through the doorway as a function of the recirculation flow rate Q_r used. The black dots represent the experiments, while the dashed line corresponds to the fitting curve. The grey-shaded portion of the graph refers to the literature data that represents the total, i.e. also considering the wake transport, inlet-volume V_{in} datum obtained for the case of zero recirculation flow rate (Kalliomäki and Koskela, 2016).

5.1.2 Imposed pressure gradient with head-driven flow

In this paragraph, the results obtained for tests number 21, 22, 23, 24 and 25 (the numbering refers to Table 3.5) will be illustrated. The most significant results are shown in Figure 5.9. In this case, it was possible to analyse the evolution of the flow rate over time for time values greater than zero. The nature of the tests themselves, where an overpressure was created by imposing a pressure difference between the two rooms, made it possible to better control the experimental parameters, reducing oscillations.

We note that for the two lowest values of the flow rate Q_{hd}, there is a portion of positive volume entering the receiving room, therefore indicating a certain amount of wake transport. The visualization, not shown here for readability reasons, of the entire curve highlighted that for none of the flow rates considered with this testing method there was any volume transport prior to the entry of the dummy into the room.

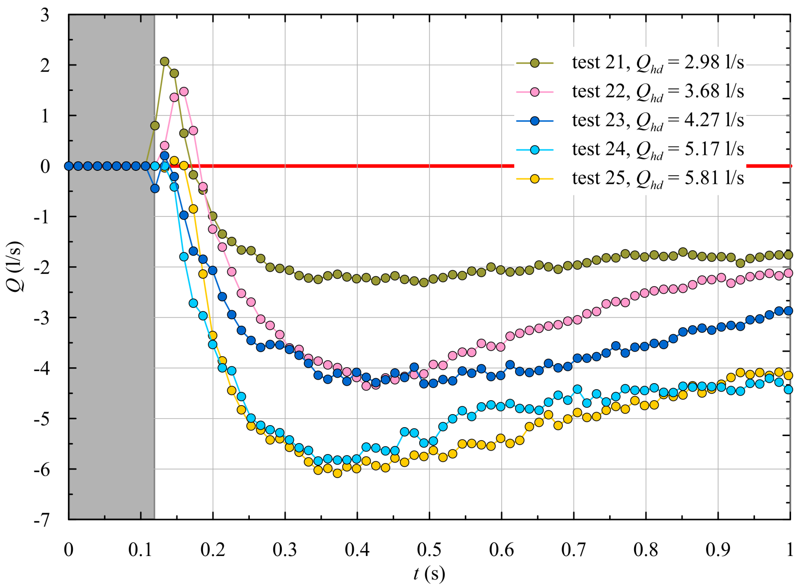

Figure 5.9: Incoming volume V_{in} into the arrival room transported by the dummy before its passage through the doorway as a function of the recirculation flow rate Q_r used. The black dots represent the experiments, while the dashed line corresponds to the fitting curve.

5.2 Turbulence

In this paragraph, a characterization of the turbulence generated as a result of the dummy's passage between the two environments will be presented. In particular, the results of the analyses carried out for the calculation of the Reynolds stresses (according to equation 4.4 derived in paragraph 4.2) and the turbulent kinetic energy, TKE (according to equation 3.1 derived in paragraph 3.1.3), will be discussed. The results shown in Figure 5.11 display, at time $t = 0.27$ s of experiment 12 in the plane $y = 0.6$ cm, the behaviour of the Reynolds stresses, in panel (a), and TKE, panel (b). The test presented is characterized by the highest mannequin velocity tested with PIV, equal to 0.86 m/s. It was deemed appropriate to show only the turbulence calculations performed on the data acquired with the PIV technique, since the dataset is much more complete and detailed compared to the UDP data. It is evident that turbulence production is concentrated in the wake region, particularly immediately behind the moving subject, where strong velocity gradients between the induced flow and the surrounding air give rise to significant shear effects. The observed TKE values, ranging between approximately 0.25 m^2/s^2 and 0.4 m^2/s^2, indicate a relatively high turbulence intensity, consistent with a strongly perturbed flow still influenced by coherent motions associated with body movement. Since the TKE values are not multiplied by the air density, they directly represent the kinetic intensity of the velocity fluctuations, providing a clear measure of the flow's capacity to generate and sustain turbulent regions in the surrounding air. A marked entrainment effect can be observed in the wake, where ambient fluid is progressively drawn into and mixed with the disturbed flow induced by the body's motion. This process enlarges the turbulent region and promotes the transfer of momentum and energy within the wake. Such behavior is typical of wake flows, where the entrainment mechanism contributes both to the rapid decay of mean velocity peaks and to the enhancement of local turbulence levels. This characteristic decrease in the peaks of the mean velocity can be observed by comparing the plots in Figures 5.5 and 5.6. The velocity of the model in Figure 5.5 is lower, resulting in a stronger drag effect, i.e. higher mean horizontal fluid velocities but reduced mixing, i.e. lower Reynolds stresses and TKE (Figure 5.10). Figure 5.10, presented for comparison with Figure 5.11, exhibits modest turbulent activity but reveals a visually similar behaviour to Figure 5.11(a) with regard to the trend of the Reynolds stresses. The upper region of the wake shows predominantly positive values, indicating a mean downward transport of horizontal momentum, whereas the lower region displays generally negative values, corresponding to an upward (positive) vertical transport of horizontal momentum. This behaviour is also confirmed by the analysis of Reynolds stresses derived from the UVP probe measurements.

As further evidence of the aforementioned observations, Figure 5.12 shows a comparison between the Reynolds stresses from tests 6 and 12, which are characterized by two different mannequin velocities U_m, namely 0.58 m/s and 0.86 m/s. The data points displayed in the two panels were obtained by averaging the Reynolds stress values located at the same height and falling within a moving window, fixed to the walker's motion, 1 cm wide and as tall as the walker, positioned 0.5 cm behind its back. From the two positions along the walker's path shown, whose reference frame is always the one reported in Figure 5.12, it can be observed that, for the test characterized by the lower walking speed, the Reynolds stresses with significant values are predominantly positive. This indicates, as previously stated, an average downward transport of horizontal momentum. In contrast, the case with the higher walker velocity $U_m = 0.86$ m/s exhibits a more chaotic pattern, highlighting a large variability in the direction of horizontal momentum transport. However, this variability tends to be more oriented toward positive values at the mannequin position $x = 4$, while it shifts toward generally negative values at $x = 17$.

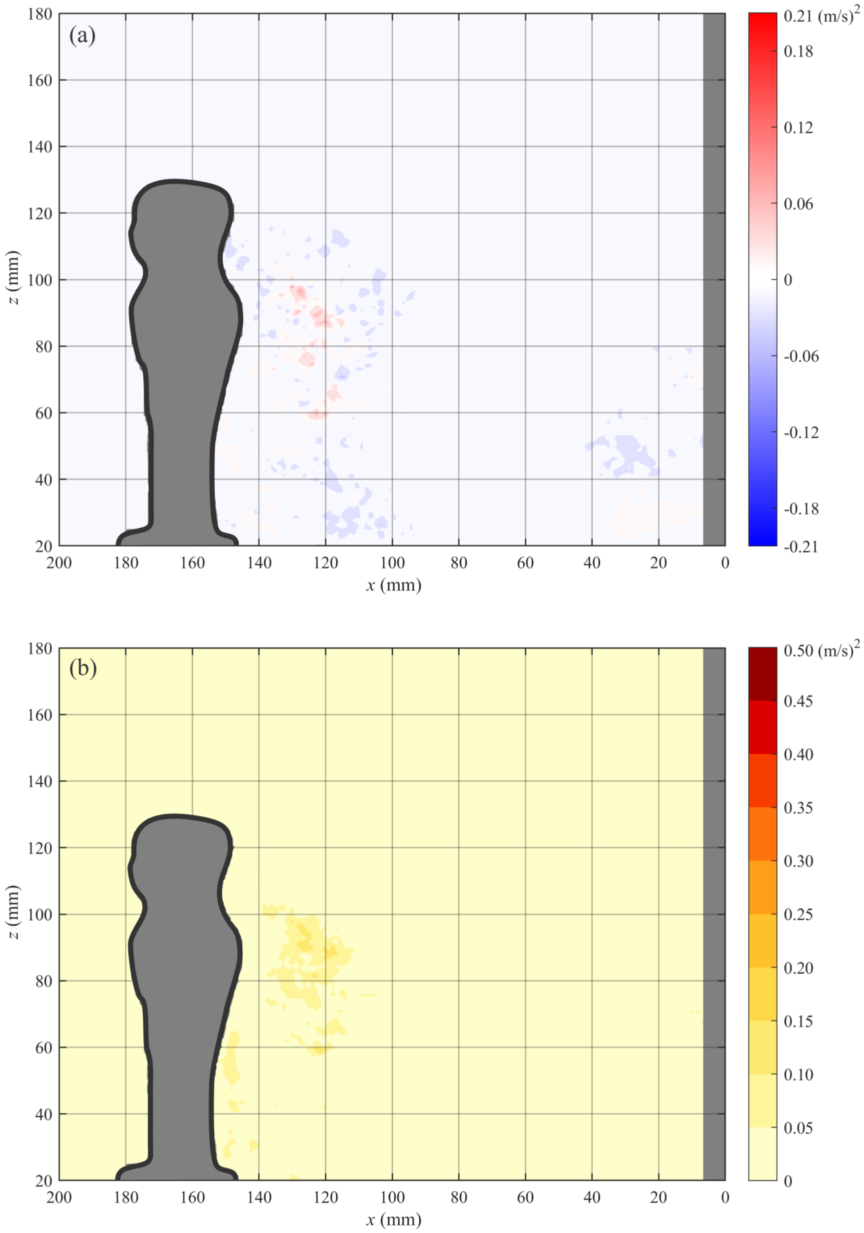

Figure 5.10: (a) Contour plot showing the mean Reynolds stress component $-\overline{u'w'}$, in $(\mathrm{m/s})^2$, for Test 6 with $U_m = 0.58$ m/s at time $t = 0.37$ s; (b) contour plot showing Turbulent Kinetic Energy (TKE), in $(\mathrm{m/s})^2$, for Test 6 with $U_m = 0.58$ m/s at time $t = 0.37$ s. The axes refer to the coordinate system presented in Figure 2.7. Test numbering according to Table 3.4. Both panels refer to plane $y = 0.6$ cm.

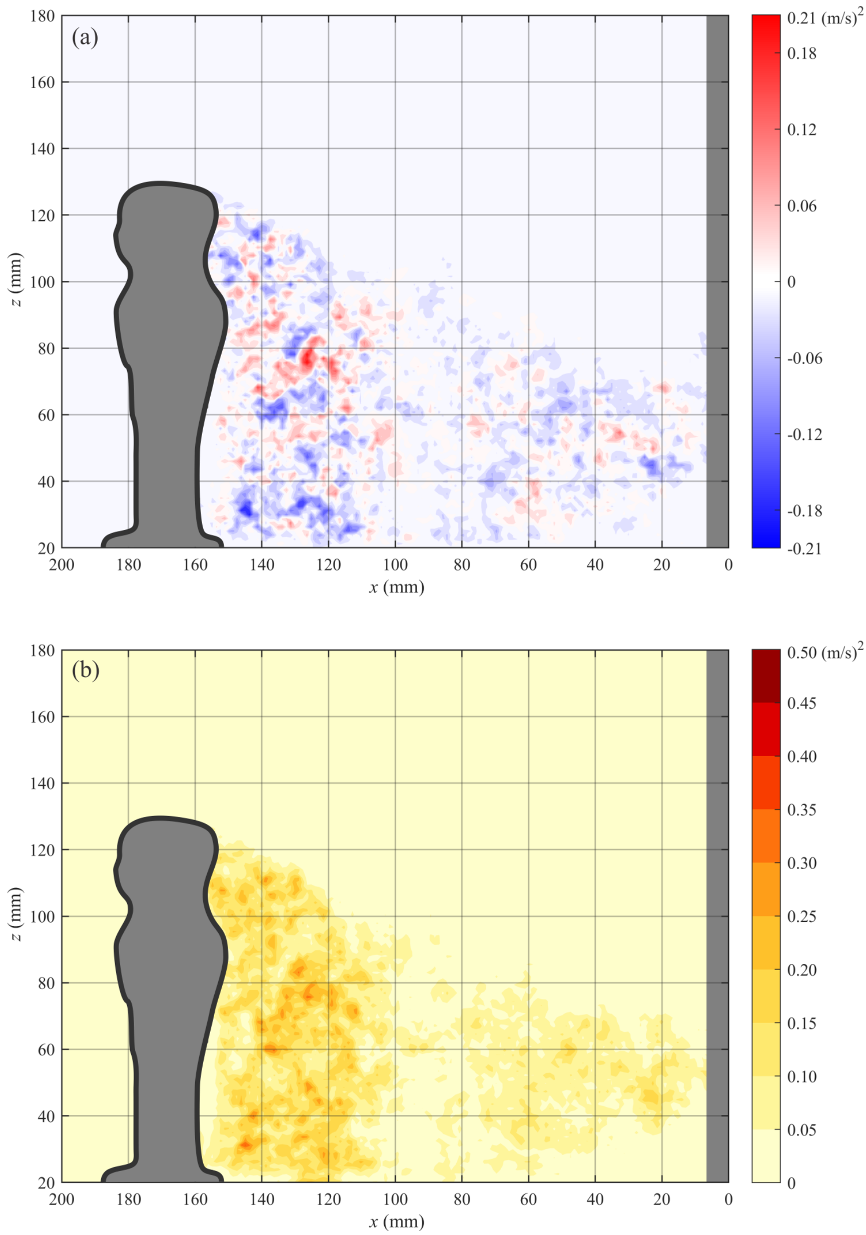

Figure 5.11: (a) Contour plot showing the mean Reynolds stress component $-\overline{u'w'}$, in $(\mathrm{m/s})^2$, for Test 12 with $U_m = 0.86$ m/s at time $t = 0.27$ s; (b) contour plot showing Turbulent Kinetic Energy (TKE), in $(\mathrm{m/s})^2$, for Test 12 with $U_m = 0.86$ m/s at time $t = 0.27$ s. The axes refer to the coordinate system presented in Figure 2.7. Test numbering according to Table 3.4. Both panels refer to plane $y = 0.6$ cm.

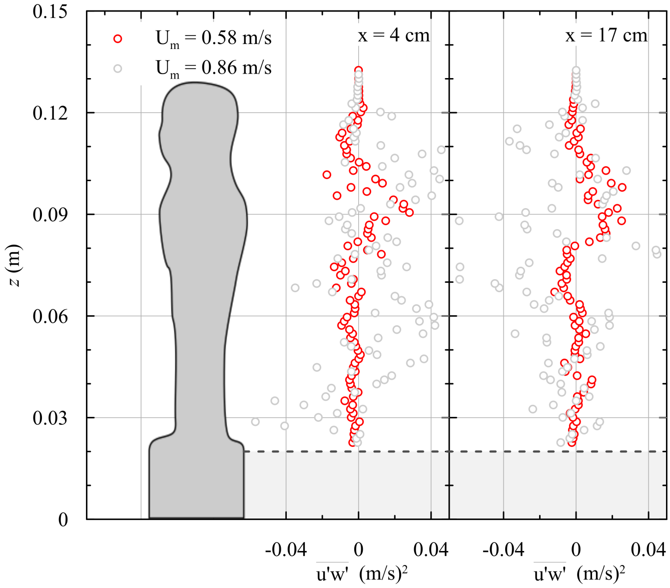

Figure 5.12: Mean Reynolds stress component $-\overline{u'w'}$ in $(\mathrm{m/s})^2$ averaged at the same height within a moving window located 0.5 cm from the walker and 1 cm wide. Results for Test 6 (U_m = 0.58 m/s) and 12 (U_m = 0.86 m/s) at positions of the mannequin equal to $x = 4$ cm and $x = 17$ cm; Test numbering according to Table 3.4. Both panels refer to plane $y = 0.6$ cm.

Chapter 6

Conclusions and future work

Air flows and their mixing dynamics in indoor environments have a huge impact on the dispersion of pollutants and, in turn, on the microclimate that develops inside buildings. The aim of the present work was to experimentally investigate the characteristics of air exchange between two interconnected indoor environments under the influence of two distinct driving mechanisms: one induced by a moving human passing from one room to the other, and the other associated with the interaction between the indoor spaces and the outdoor environment, namely the effects of external wind and airflows entering through the windows. The research topic is broad and complex; therefore, to ensure coherence and consistency, the study focused on a single physical model investigated using different measurement techniques. To enrich the analysis, both reduced-scale similarity with water–air and air–air systems was employed.

In particular, the use of water as the working fluid, analogous to air in the full-scale phenomenon, allowed for the exploitation of several experimental advantages, notably the use of more effective instrumentation for characterizing the turbulent structures induced by human motion. These include ultrasonic probes and Particle Image Velocimetry (PIV) techniques, which require the dispersion of tracer particles that remain more effectively suspended in water than in air. Moreover, water facilitates the preservation of Reynolds number similarity, which is essential for accurately reproducing turbulent flow and momentum exchange phenomena. It also enables better control of boundary conditions, promoting the maintenance of steady-state flow rates and density distributions. At the same time, it was also possible to perform reduced-scale modeling using air as the working fluid in the physical model, thanks to the application of Reynolds number similarity, given the fully developed turbulent flow regimes under investigation, and to the experimental facilities made available by the IISTA of Granada, first and foremost their environmental wind tunnel.

6.1 Summary of main results

Our research involved the design and construction of an experimental setup representing a reduced-scale replica of two rooms connected by a standard doorway.

The main objective of the first part of the study was focused on investigating the airflow dynamics at the opening between the two rooms when the physical model was subjected to atmospheric-type forcing. For this purpose, a 1:15 scale experimental apparatus was designed, based on Reynolds similarity, equipped with a series of small openings designed to simulate the presence of windows in the two rooms, which could be opened or closed in various configurations.

This model, made of wood, was studied by placing it inside an open-circuit wind tunnel. By imposing different freestream wind velocities inside the tunnel, various angles of wind attack on the model, and different window opening/closing configurations, a substantial amount of data was collected for the characterization of the model.

The instrumentation used to measure air velocity was based on hot-wire anemometry technology, which allowed measurement of the two velocity components, horizontal and vertical, at 42 points along three vertical lines located at the opening. These measurements were complemented by a pressure transducer capable of measuring the pressure difference between the two rooms through two static taps specifically arranged for this purpose.

The data analysis allowed for the characterization of the turbulence generated in the various studied scenarios, as well as the calculation of the flow rate passing through the doorway in each case. This flow rate, after a dimensional analysis aimed at identifying the characteristic dimensionless groups for the phenomenon under study, was then expressed as a function of the Euler number and compared with a theoretical flow rate obtained through an extension of Bernoulli's theorem. This comparison revealed an increase in flow rate as a function of the Euler number Eu following a power law with an exponent of 0.39, compared to the theoretical case where the exponent is 0.5.

A study was also conducted on the discharge coefficient C_{zi} as a function of the internal Reynolds number at the opening, considering variations in both the porosity of the upstream wall of the model and the freestream wind velocity.

The main objective of the second part of the study was to examine how human motion through the doorway, commonly referred to as the "pump effect" (Jha et al., 2021b), influences mass transfer between adjacent indoor spaces, with particular emphasis on the effects of walking speed and the presence of mean flow structures. For this purpose, a 1:15 scale experimental apparatus was designed, based on Reynolds similarity and with the same geometry of the model used for wind tunnel activities, consisting of a water-filled tank that allowed modelling two rooms connected by a doorway and studying the effects on the two environments caused by the passage of a human being from one room to the other. This apparatus made it possible to control the speed of the scaled human model (a foosball figure) and to determine its position along the rail on which it was free to move, as well as to impose a recirculation flow in the direction opposite to the mannequin's motion, in order to mitigate contamination between the two rooms. Various advancing speeds of the figure were tested, such as 0.16 m/s, 0.79 m/s, and 1.13 m/s, whose ratio to the speeds of a real human at full scale is equal to 1, thanks to the similarity ratios. The use of ultrasonic profilometers (UVP) and particle image velocimetry (PIV) technology made it possible to measure and visualize the resulting two-dimensional flow fields, as well as to study their turbulence through Reynolds stresses and the generated turbulent kinetic energy (TKE). The tests with induced pressure gradient flow also allowed a closer connection to practical cases, such as operating rooms or over-pressurized environments in which designers aim to limit air exchange between indoor spaces, were considered. To investigate this situation, the variations in the volumes introduced into the target room by the moving human figure were analysed as a function of different recirculation flow rates Q_r or head-driven flow rates Q_{hd}. A simplified model which relates the incoming volume before the mannequin enters the arrival room to the recirculation flow rate, constitutes the main outcome of the study. Furthermore, the analysis of the volumes introduced after the dummy enters the arrival room, based on tests with head-driven flow, made it possible to quantify the flow rates above which contamination becomes negligible once the mannequin has entered the room.

6.1.1 Practical implications for building ventilation and indoor airflow control

The findings of this study have significant implications for building physics, particularly in the understanding and control of airflow and contaminant transport between adjacent indoor environments. Doorways represent one of the most critical pathways for air exchange within buildings, and their behaviour is influenced by a complex interaction between external wind forcing, internal pressure gradients, buoyancy effects, and transient disturbances generated by occupant movement. While ventilation systems are typically designed under steady-state assumptions, real indoor environments are characterized by frequent transient events, such as door opening, human passage, and local pressure fluctuations, which can significantly alter airflow patterns and contaminant dispersion.

The experimental results obtained in this work provide quantitative insight into both wind-driven airflow and the pump effect associated with human motion, contributing to a more realistic representation of inter-room air transfer mechanisms. In particular, the measurements highlight how the passage of a person through a doorway generates complex wake structures and displacement flows capable of transporting a significant volume of air from one space to another. These transient transport mechanisms can be comparable in magnitude to background ventilation flows, especially in situations where the imposed pressure differences between adjacent spaces are small. As a result, models that neglect occupant-induced airflow may underestimate the potential for cross-contamination between rooms.

These aspects are particularly relevant in environments where strict control of airborne contamination is required, such as hospitals, isolation wards, operating theatres, cleanrooms, and other pressurized indoor spaces. In particular, in operating theatres and surgical suites, positive pressurization is commonly employed to protect sterile environments from external contamination. Nevertheless, the frequent movement of medical staff, the opening of doors, and the transfer of equipment between adjacent rooms can generate transient airflow exchanges that may introduce airborne particles into the surgical area. Understanding the magnitude and dynamics of such transport processes is therefore essential for evaluating the real effectiveness of ventilation strategies and for designing layouts that minimize contamination risks.

Another important application concerns cleanroom environments used in pharmaceutical manufacturing, semiconductor production, and biotechnology laboratories. In these settings, strict control of particle concentration is required to ensure product quality and process reliability. Doorways connecting clean and less-clean areas represent critical interfaces where contamination control strategies must be carefully implemented. Personnel movement, in particular, has been recognized as one of the main sources of particle transport between zones of different cleanliness classes. The pump effect generated by human motion can therefore represent a non-negligible mechanism for the transfer of contaminated air across pressure-controlled boundaries.

Beyond healthcare and industrial clean environments, the results of this study are also relevant to other types of buildings where indoor air quality and pollutant transport are major concerns. Examples include laboratory facilities handling hazardous chemicals, buildings exposed to outdoor pollutants in urban environments, and educational or office buildings where high occupant density can increase the risk of airborne disease transmission. In these contexts, understanding the combined influence of ventilation systems, pressure differentials, and occupant-induced flows is essential for predicting how contaminants spread within the building.

The relationships identified in this work between transported volume and imposed recirculation or pressure-driven flow rates provide useful indications for the design and optimization of ventilation strategies aimed at reducing cross-contamination risks. The experimental data and simplified models derived from this work may support the development and validation of predictive tools used in building airflow modelling. Computational fluid dynamics (CFD) simulations and multizone airflow models are increasingly employed to evaluate ventilation performance, contaminant dispersion, and infection risk in buildings. It is well known that the accuracy of these tools depends on the availability of reliable empirical data describing real airflow exchange mechanisms across internal openings. The measurements presented here can therefore contribute to improving model parameterization and to validating simulation approaches that aim to capture transient airflow phenomena associated with occupant movement.

A better understanding of airflow exchange through doorways has the potential to inform both architectural design and ventilation engineering. Design strategies such as the use of vestibules, airlocks, directional airflow control, automated door systems, or optimized circulation patterns may significantly reduce the probability of contaminant transfer between spaces. By integrating experimental evidence on transient airflow processes with building design and ventilation strategies, it becomes possible to achieve more effective control of indoor air quality, improve the reliability of contamination containment systems, and enhance the overall resilience of buildings against airborne hazards.

6.2 Directions for future work

The directions for future work, building on what has been addressed in this thesis, can concern both the field of design of heating, ventilation, air conditioning (HVAC) systems and the development of the experimentally acquired data for the validation of computational fluid dynamics (CFD) models.

The contribution of this work to ventilation system designers can lie in the design of localized systems aimed at limiting the backflow that was observed and spatially and temporally identified in Chapter 5.

As for the numerical modeling, an initial rudimentary CFD model of the downstream room used in the wind tunnel experiments has already been developed. Using Ansys Fluent 2024 as the computational software, some preliminary results have been obtained, so far at a qualitative and basic level, which could enable the development of a 3D model capable of reproducing the flow field of the empty room under different configurations of opened/closed windows using as boundary conditions the experimental data obtained.

Bibliography

Daniel P Albuquerque, Paul D O'Sullivan, and Guilherme Carrilho da Graça. Effect of window geometry on wind driven single sided ventilation through one opening. *Energy and Buildings*, 245:111060, 2021. (Cited on page 22.)

Mehrzad Ansaripour, Mohammad Abdolzadeh, and Saleh Sargazizadeh. Computational modeling of particle transport and distribution emitted from a laserjet printer in a ventilated room with different ventilation configurations. *Applied Thermal Engineering*, 103:920–933, 2016. (Cited on page 24.)

Jack Arbuthnot. *An essay concerning the effects of air on human bodies.* 1751. (Cited on page 17.)

Erik Bjørn, Magnus Mattsson, Mats Sandberg, and Peter V Nielsen. Displacement ventilation: effects of movement and exhalation. 1997. (Cited on page 24.)

Henrik Brohus, KD Balling, and D Jeppesen. Influence of movements on contaminant transport in an operating room. *Indoor air*, 16(5), 2006. (Cited on page 24.)

S. J. Cao and J. Meyers. Influence of turbulent boundary conditions on rans simulations of pollutant dispersion in mechanically ventilated enclosures with transitional slot reynolds number. *Building and Environment*, 59: 397–407, 2013. (Cited on page 19.)

Wang Y. Logachev K. I. Ziganshin A. M. Huang Y. Cao, Y. and Z. Yu. Experimental and theoretical investigation on transportation of gaseous pollutants in long and narrow industrial buildings. *International Journal of Heat and Mass Transfer*, 199:123453, 2022. (Cited on page 26.)

Zhu D. H. Cao, S. J. and Y. B. Yang. Associated relationship between ventilation rates and indoor air quality. *RSC Advances*, 6(112):111427–111435, 2016. (Cited on page 19.)

R.A. Catarelli, P.L. Fernández-Cabán, F.J. Masters, J.A. Bridge, K.R. Gurley, and C.J. Matyas. Automated terrain generation for precise atmospheric boundary layer simulation in the wind tunnel. *Journal of Wind Engineering and Industrial Aerodynamics*, 207:104276, 2020. ISSN 0167-6105. doi: https://doi.org/10.1016/j.jweia.2020.104276. URL https://www.sciencedirect.com/science/article/pii/S0167610520301860. (Cited on pages 36 and 37.)

C. K. Chan and X. H. Yao. Air pollution in mega cities in china. *Atmospheric Environment*, 42(1):1–42, 2008. (Cited on page 20.)

Qingyan Chen. Ventilation performance prediction for buildings: A method overview and recent applications. *Building and Environment*, 44(4):848–858, 2009. (Cited on page 25.)

Peng Cheng et al. Probable cross-corridor transmission of sars-cov-2 due to cross airflows and its control. *Building and Environment*, 218:109137, 2022. (Cited on page 22.)

J. I. Choi and J. R. Edwards. Large-eddy simulation of human-induced contaminant transport in room compartments. *Indoor Air*, 22(1):77–87, 2012. (Cited on page 26.)

Chia Chu, Chiu, and Kun Wang. An experimental study of wind-driven cross ventilation in partitioned buildings. *Energy and Buildings*, 42:667–673, 05 2010. doi: 10.1016/j.enbuild.2009.11.004. (Cited on pages 27, 76, 78, 79, 81, and 82.)

D. Ciuzas, T. Prasauskas, E. Krugly, A. Jurelionis, L. Seduikyte, and D. Martuzevicius. Indoor air quality management by combined ventilation and air cleaning: An experimental study. *Aerosol and Air Quality Research*, 16(10):2550–2559, 2016. (Cited on page 19.)

Peng-Yi Cui et al. Wind-tunnel studies on the characteristics of indoor/outdoor airflow and pollutant exchange in a building cluster. *Journal of Wind Engineering and Industrial Aerodynamics*, 214:104645, 2021. (Cited on page 20.)

Guilherme Carrilho Da Graça and Paul F Linden. Simplified modeling of cross-ventilation airflow/discussion. *ASHRAE Transactions*, 109:65, 2003. (Cited on page 22.)

Guilherme Carrilho da Graca, Daniel P Albuquerque, Mats Sandberg, and PF Linden. Pumping ventilation of corner and single sided rooms with two openings. *Building and Environment*, 205:108171, 2021. (Cited on page 22.)

Nicholas Charles Daish, G Carrilho da Graça, Paul Frederick Linden, and D Banks. Impact of aperture separation on wind-driven single-sided natural ventilation. *Building and Environment*, 108:122–134, 2016. (Cited on page 22.)

Henk de Bruin and C. Moore. Zero-plane displacement and roughness length for tall vegetation, derived from a simple mass conservation hypothesis. *Boundary-Layer Meteorology*, 31:39–49, 06 1985. doi: 10.1007/BF00120033. (Cited on page 37.)

Zhibao Dong, Shangyu Gao, and Donald Fryrear. Drag coefficients, roughness length and zero-plane displacement height as disturbed by artificial standing vegetation. *Journal of Arid Environments*, 49:485–505, 11 2001. doi: 10.1006/jare.2001.0807. (Cited on page 37.)

Fu Z. Wang J. Wang Z. Suo H. Kong X. Fan, M. and H. Li. A review of different ventilation modes on thermal comfort, air quality and virus spread control. *Building and Environment*, 212:108831, 2022. (Cited on page 20.)

Z. Feng, Z. Long, and J. Mo. Experimental and theoretical study of a novel electrostatic enhanced air filter (eeaf) for fine particles. *Journal of Aerosol Science*, 102:41–54, 2016. (Cited on page 19.)

L. Fontana and A. Quintino. Experimental analysis of the transport of airborne contaminants between adjacent rooms at different pressure due to the door opening. *Building and Environment*, 81:81–91, 2014. (Cited on page 23.)

T. Godish and J. D. Spengler. Relationships between ventilation and indoor air quality: a review. *Indoor Air*, 6(2):135–145, 1996. (Cited on page 20.)

Ghali K. Ghaddar N. Chakroun W. Habchi, C. and S. Alotaibi. Ceiling personalized ventilation combined with desk fans for reduced direct and indirect cross-contamination and efficient use of office space. *Energy Conversion and Management*, 111:158–173, 2016. (Cited on page 21.)

Saleh N. Paunescu A. C. Momas I. Hachem, M. and L. Bensefa-Colas. Exposure to traffic air pollutants in taxicabs and acute adverse respiratory effects: A systematic review. *Science of the Total Environment*, 693: 133439, 2019. (Cited on page 20.)

Jian Hang, Yuguo Li, WH Ching, Jianjian Wei, Ruiqiu Jin, Li Liu, and Xiaojian Xie. Potential airborne transmission between two isolation cubicles through a shared anteroom. *Building and Environment*, 89:264–278, 2015. (Cited on pages 22 and 23.)

Abolfazl Hayati, Magnus Mattsson, and Mats Sandberg. A wind tunnel study of wind-driven airing through open doors. *International journal of ventilation*, 18(2):113–135, 2019. (Cited on pages 21 and 22.)

G. R. Hunt and P. P. Linden. The fluid mechanics of natural ventilation—displacement ventilation by buoyancy-driven flows assisted by wind. *Building and Environment*, 34(6):707–720, 1999. (Cited on page 20.)

Narsing K Jha, D Frank, L Darracq, and PF Linden. Contaminant transport by human passage through an air curtain separating two sections of a corridor: Part ii–two zones at different temperatures. *Energy and buildings*, 236:110728, 2021a. (Cited on page 24.)

Narsing K Jha, D Frank, and PF Linden. Contaminant transport by human passage through an air curtain separating two sections of a corridor: Part i–uniform ambient temperature. *Energy and Buildings*, 236:110818, 2021b. (Cited on pages 24 and 109.)

Gagytė L. Prasauskas T. Čiužas D. Krugly E. Šeduikytė L. Jurelionis, A. and D. Martuzevicius. The impact of the air distribution method in ventilated rooms on the aerosol particle dispersion and removal: The experimental approach. *Energy and Buildings*, 86:305–313, 2015. (Cited on page 21.)

Saarinen P. Tang J. W. Kalliomäki, P. and H. Koskela. Airflow patterns through single hinged and sliding doors in hospital isolation rooms–effect of ventilation, flow differential and passage. *Building and Environment*, 107:154–168, 2016. (Cited on pages 13, 23, and 100.)

DE Kiel and DJ Wilson. Combining door swing pumping with density driven flow. 1989. (Cited on page 23.)

Ashvath Kunadi, Richard Silberstein, and Sally Thompson. Variation in zero plane displacement and roughness length for momentum revisited. *Boundary-Layer Meteorology*, 190, 08 2024. doi: 10.1007/s10546-024-00876-8. (Cited on page 37.)

GF Lane-Seriff, PF Linden, and JE Simpson. Transient flow through doorways produced by temperature difference. 1987. (Cited on page 23.)

Martin W. Liddament. A review of ventilation and the quality of ventilation air. *Building and Environment*, 2000. (Cited on page 20.)

P. F. Linden. The fluid mechanics of natural ventilation. *Annual Review of Fluid Mechanics*, 31(1):201–238, 1999. (Cited on page 20.)

PF Linden and JE Simpson. Buoyancy driven flow through an open door. 1985. (Cited on pages 19 and 23.)

Simon R. Livermore and Andrew W. Woods. Natural ventilation of a building with heating at multiple levels. *Building and Environment*, 42(3):1417–1430, 2007. (Cited on page 25.)

L. Lv, L. Zeng, Y. Wu, J. Gao, W. Xie, C. Cao, and J. Zhang. Effects of human walking on the capture efficiency of range hood in residential kitchen. *Building and Environment*, 196:107821, 2021. (Cited on page 20.)

Yang Lv, Haifeng Wang, Yuwei Zhou, Hiroshi Yoshino, Hiroshi Yonekura, Rie Takaki, and Genta Kurihara. The influence of ventilation mode and personnel walking behavior on distribution characteristics of indoor particles. *Building and Environment*, 149:582–591, 2019. ISSN 0360-1323. doi: https://doi.org/10.1016/j.buildenv.2018.12.057. URL https://www.sciencedirect.com/science/article/pii/S0360132318308151. (Cited on page 28.)

HK Malinowski. Wind effect on the air movement inside buildings. 1971. (Cited on page 21.)

T. M. Mata, A. A. Martins, C. S. Calheiros, F. Villanueva, N. P. Alonso-Cuevilla, M. F. Gabriel, and G. V. Silva. Indoor air quality: a review of cleaning technologies. *Environments*, 9(9):118, 2022. (Cited on page 20.)

M Mattson and M Sandberg. Displacement ventilation-influence of physical activity. 1994. (Cited on page 24.)

M Mattsson. Velocity field created by moving objects in rooms. In *Proc. of the 5ˆ¡ th¿ International Conference on Air Distribution in Rooms, 1996*, 1996. (Cited on page 24.)

Daniel Micallef, Vincent Buhagiar, and Simon P Borg. Cross-ventilation of a room in a courtyard building. *Energy and buildings*, 133:658–669, 2016. (Cited on page 22.)

N. Mingotti, T. Chenvidyakarn, and A. W. Woods. The fluid mechanics of the natural ventilation of a narrow-cavity double-skin facade. *Building and Environment*, 46(4):807–823, 2011. (Cited on pages 20 and 25.)

N. Mingotti, T. Chenvidyakarn, and A. W. Woods. Combined impacts of climate and wall insulation on the energy benefit of an extra layer of glazing in the facade. *Energy and Buildings*, 58:237–249, 2013. (Cited on pages 20 and 25.)

N. Mingotti, R. Wood, C. Noakes, and A. W. Woods. The mixing of airborne contaminants by the repeated passage of people along a corridor. *Journal of Fluid Mechanics*, 903:A52, 2020a. (Cited on pages 20 and 26.)

Nicola Mingotti, Richard Wood, Catherine Noakes, and Andrew W. Woods. The mixing of airborne contaminants by the repeated passage of people along a corridor. *Journal of Fluid Mechanics*, 903:A52, 2020b. doi: 10.1017/jfm.2020.671. (Cited on page 28.)

E. S. Mousavi and K. R. Grosskopf. Airflow patterns due to door motion and pressurization in hospital isolation rooms. *Science and Technology for the Built Environment*, 22(4):379–384, 2016. (Cited on page 23.)

T. Norton and D. W. Sun. Computational fluid dynamics (cfd)–an effective and efficient design and analysis tool for the food industry: a review. *Trends in Food Science & Technology*, 17(11):600–620, 2006. (Cited on page 26.)

T. Norton, D. W. Sun, J. Grant, R. Fallon, and V. Dodd. Applications of computational fluid dynamics (cfd) in the modelling and design of ventilation systems in the agricultural industry: A review. *Bioresource Technology*, 98(12):2386–2414, 2007. (Cited on page 26.)

Roshan C Oberoi, Jung-Il Choi, Jack R Edwards, Jacky A Rosati, Jonathan Thornburg, and Charles E Rodes. Human-induced particle re-suspension in a room. *Aerosol Science and Technology*, 44(3):216–229, 2010. (Cited on page 24.)

M. Ohba, K. Irie, and T. Kurabuchi. Study on airflow characteristics inside and outside a cross-ventilation model, and ventilation flow rates using wind tunnel experiments. *Journal of Wind Engineering and Industrial Aerodynamics*, 89(14):1513–1524, 2001. ISSN 0167-6105. doi: https://doi.org/10.1016/S0167-6105(01)00130-1. URL https://www.sciencedirect.com/science/article/pii/S0167610501001301. Bluff Body Aerodynamics and Applications. (Cited on page 26.)

M. Pettenkofer. Xxix.—volumetric estimation of atmospheric carbonic acid. *Q. J. Chem. Soc.*, 10:292–297, 1858. doi: 10.1039/QJ8581000292. URL http://dx.doi.org/10.1039/QJ8581000292. (Cited on page 18.)

P. Saarinen, P. Kalliomäki, H. Koskela, and J. W. Tang. Large-eddy simulation of the containment failure in isolation rooms with a sliding door—an experimental and modelling study. *Building Simulation*, 11: 585–596, 2018. (Cited on page 22.)

M Sandberg and M Mattsson. The effect of moving heat sources upon the stratification in rooms ventilated by displacement ventilation. 1992. (Cited on page 24.)

Mats Sandberg, Magnus Mattsson, Hans Wigö, Abolfazl Hayati, Leif Claesson, Elisabet Linden, and Mubashar Ahmed Khan. Viewpoints on wind and air infiltration phenomena at buildings illustrated by field and model studies. *Building and Environment*, 92:504–517, 2015. (Cited on page 22.)

Mohammadreza Shirzadi, Yoshihide Tominaga, and Parham A. Mirzaei. Wind tunnel experiments on cross-ventilation flow of a generic sheltered building in urban areas. *Building and Environment*, 158:60–72, 2019. ISSN 0360-1323. doi: https://doi.org/10.1016/j.buildenv.2019.04.057. URL https://www.sciencedirect.com/science/article/pii/S0360132319303099. (Cited on page 27.)

Monika Śmiełowska, Mariusz Marć, and Bożena Zabiegała. Indoor air quality in public utility environments—a review. *Environmental Science and Pollution Research*, 24:11166–11176, 2017. (Cited on page 18.)

Mutmainnah Sudirman, Stefanie Gillmeier, Twan van Hooff, and Bert Blocken. Wind tunnel measurements of cross-ventilation flow in a realistic building geometry: Influence of building partitions and wind direction. *Journal of Wind Engineering and Industrial Aerodynamics*, 254:105907, 2024. ISSN 0167-6105. doi: https://doi.org/10.1016/j.

jweia.2024.105907. URL https://www.sciencedirect.com/science/article/pii/S0167610524002708. (Cited on page 27.)

Y. Tao, K. Inthavong, P. Petersen, K. Mohanarangam, W. Yang, and J. Tu. Experimental visualisation of wake flows induced by different shaped moving manikins. *Building and Environment*, 142:361–370, 2018. (Cited on page 23.)

Yao Tao, Kiao Inthavong, and Jiyuan Tu. Computational fluid dynamics study of human-induced wake and particle dispersion in indoor environment. *Indoor and Built Environment*, 26(2):185–198, 2017. doi: 10.1177/1420326X16661025. URL https://doi.org/10.1177/1420326X16661025. (Cited on page 28.)

C. Walker, G. Tan, and L. Glicksman. Reduced-scale building model and numerical investigations to buoyancy-driven natural ventilation. *Energy and Buildings*, 43(9):2404–2413, 2011. (Cited on page 20.)

PR Warren. Ventilation through openings on one wall only. In *International Conference Heat and Mass transfer in Buildings, Dubrovnik, Yugoslavia*, 1977. (Cited on page 22.)

Rudolf O. Weber. Remarks on the definition and estimation of friction velocity. *Boundary-Layer Meteorology*, 93(2):197–209, Nov 1999. ISSN 1573-1472. doi: 10.1023/A:1002043826623. URL https://doi.org/10.1023/A:1002043826623. (Cited on page 37.)

Jon Wieringa. Updating the davenport roughness classification. *Journal of Wind Engineering and Industrial Aerodynamics*, 41(1):357–368, 1992. ISSN 0167-6105. doi: https://doi.org/10.1016/0167-6105(92)90434-C. URL https://www.sciencedirect.com/science/article/pii/016761059290434C. (Cited on page 38.)

S. C. Wong, A. K. W. Au, H. Chen, L. L. H. Yuen, X. Li, D. C. Lung, and V. C. C. Cheng. Transmission of omicron (b. 1.1. 529)-sars-cov-2 variant of concern in a designated quarantine hotel for travelers: a challenge of elimination strategy of covid-19. *The Lancet Regional Health–Western Pacific*, 18, 2022. (Cited on page 22.)

Jialin Wu, Jing Geng, Ming Fu, and Wenguo Weng. Multi-person movement-induced airflow and the effects on virus-laden expiratory droplet dispersion in indoor environments. *Indoor air*, 32(9):e13119, 2022. (Cited on page 20.)

Weiqin Wu and Zhang Lin. Experimental study of influence of movements on airflow under stratum ventilation. *Energy Procedia*, 78:1207–1211, 2015. (Cited on page 24.)

Z. Zhang and Q. Chen. Experimental measurements and numerical simulations of particle transport and distribution in ventilated rooms. *Atmospheric Environment*, 40(18):3396–3408, 2006. (Cited on page 20.)

M. Zheng, Y. Fan, X. Li, D. Lester, X. Chen, Y. Li, and I. Cole. Aerosol exchange between pressure-equilibrium rooms induced by door motion and human movement. *Building and Environment*, page 110486, 2023. (Cited on page 26.)

C. Zhuang, G. Yang, T. Long, and D. Hu. Numerical comparison of removal and deposition for fully-distributed particles in central-and split-type air-conditioning rooms. *Building and Environment*, 112:17–28, 2017. (Cited on page 21.)

Andrzej Zięba. Effective number of observations and unbiased estimators of variance for autocorrelated data - an overview. *Metrology and Measurement Systems*, XVII:14, 01 2010. doi: 10.2478/v10178-010-0001-0. (Cited on page 83.)